Double Pionic Fusion:

Towards an Understanding of the ABC Puzzle
by Exclusive Measurements

Dissertation

vorgelegt von
Mikhail Bashkanov
aus Samara
2006

Abstract

Unter dem ABC-Effekt versteht man eine riesige Überhöhung am unteren Ende des Spektrums der invarianten Masse von zwei Pionen, die in der doppelt-pionischen Fusion zu gebundenen nuklearen Systemen entstehen. Dieses eigenartige Phänomen konnte seit seiner erstmaligen Beobachtung 1960 in Messungen der ^{3}He-Ejektile in der Reaktion $pd \rightarrow {}^3\text{He}X$ bisher nicht schlüssig erklärt werden. Ein Grund dafür ist, dass alle bisherigen Messungen zu diesem Effekt inklusive Messungen waren, d.h. lediglich mit Detektoren zum Nachweis des schweren Fragments durchgeführt wurden, was bedeutet, dass nicht die vollständige experimentell zugängliche Information erfasst wurde.

Daher wurden an CELSIUS/WASA erstmals vollständige exklusive Messungen dieser Reaktion bei einer Energie von $T_p = 0.895\,\text{GeV}$ durchgeführt, bei der man das Maximum des ABC-Effekts erwartet. Damit wurden zum ersten Mal kinematisch vollständige Daten hinreichender Statistik und getrennt nach Kanälen neutraler und geladener Pionen, d.h. getrennt nach $pd \rightarrow {}^3\text{He}\pi^0\pi^0$ und $pd \rightarrow {}^3\text{He}\pi^+\pi^-$ gemessen. Als Nebenprodukt wurden auch Ergebnisse zur Drei-Pionen-Produktion erhalten.

Die neuen Messdaten sind konsistent mit den früheren inklusiven Messungen. Sie liefern aber weit umfangreichere Detailinformationen, die alle früheren Erklärungsversuche ausschließen. Der jetzt zugängliche, kinematisch komplette Datensatz enthüllt, dass die Überhöhung bei niedrigen ππ-Massen (ABC-Effekt)
- nicht notwendigerweise mit einer Überhöhung bei großen ππ-Massen einhergeht,
- immer mit der gleichzeitigen Anregung von zwei Δ-Resonanzen verbunden ist,
- von skalar-isoskalarer Natur, d.h. ein σ-Kanal-Phänomen ist,
- eine Dynamik im Reaktionssystem erfordert, die bisher nicht betrachtet wurde.

Verschiedene mögliche Lösungen werden in dieser Arbeit diskutiert. Alle von ihnen erfordern eine starke Attraktion zwischen den beiden produzierten Δ-Teilchen – ein Punkt, der bisher weder in theoretischen noch experimentellen Arbeiten untersucht wurde.

Für die Analyse der Daten wurden neue leistungsfähige Methoden entwickelt, die auf den Techniken neuraler Netze basieren. Laufende wie auch mögliche zukünftige Anwendungen werden diskutiert.

Abstract

The ABC effect is a huge unexpected enhancement at twice the pion mass in the invariant mass spectrum of two pions, which are generated in double-pionic fusion to bound nuclear systems. This peculiar phenomenon has been missing a conclusive explanation all the time since it has been discovered 1960 in single-arm measurements of ^{3}He ejectiles in the reaction $pd \rightarrow {}^3\text{He}X$. One reason for this failure has been that all measurements to this subject have been inclusive, i.e., lacking the full experimentally accessible information. Hence exclusive measurements were performed at CELSIUS/WASA at an energy of $T_p = 0.895\,\text{GeV}$, where the ABC effect is expected to be strongest. For the first time exclusive data of solid statistics for both the $pd \rightarrow {}^3\text{He}\pi^0\pi^0$ and $pd \rightarrow {}^3\text{He}\pi^+\pi^-$ reactions were obtained including also results for the three-pion production total cross-section.

The new data are consistent with the previous inclusive data. They provide, however, much more additional information, which rule out all previous explications of the ABC effect. The now available kinematically complete set of data reveals that the low $\pi\pi$-mass enhancement (ABC-effect)

- is not necessarily associated with a high $\pi\pi$-mass enhancement,
- is always connected with the simultaneous excitation of two Δ resonances,
- is of scalar-isoscalar nature, i.e. a σ-channel phenomenon,
- requires dynamics in the reaction system, which has not been considered hitherto.

Various possible solutions are discussed, however, all of them demand a high attraction in the $\Delta\Delta$ system — a point, which has never been touched so far in theoretical and experimental investigations.

For this data analysis new powerful methods based on neural nets have been developed. Their current and possible future applications are discussed.

There is a remarkably close parallel between the problems of the physicist and those of the cryptographer. The system on which a message is enciphered corresponds to the laws of the universe, the intercepted messages to the evidence available, the keys for a day or a message to important constants which have to be determined. The correspondence is very close, but the subject matter of cryptography is very easily dealt with by discrete machinery, physics not so easily.

--Alan Turing

Contents

1 Introduction

Since the dawn of mankind, when a monkey jumped down from a tree becoming a human being, people have been trying to understand the laws of nature — moving a long way on the road of knowledge. We do not worry any longer about thunderstorms, we can create light brighter than the sun at noon and fly faster than any bird. We know why the sun is shining, why the wind is blowing and why the sky has a blue color. We even can sometimes initiate a rain, not by asking a god like ancient oracles, but by our will and technology. We tend to believe that we finally come close to a full understanding of the world around us and we need just another small step to succeed in a unified theory, which would be able to describe each process that ever happened in the Universe. However, since such a theory does not yet exist, we have to stick with its simplified version — the Standard Model.

The present model of everything like the mythological turtle is placed on three whales: General Relativity, Electroweak Theory and Quantum Chromodynamics (QCD). Each of these theories describes different forces: General relativity is responsible for the moving of stars and galaxies, i.e. phenomena related to gravity. The Electroweak Theory contains two parts: the Glashow-Weinberg-Salam theory for the weak force and Quantum Electrodynamics (QED) for the electro-magnetic interactions. QCD is the theory of the strong force. Having all these theories at hand we still have problems in describing phenomena in reality, not because theories are wrong, but just due to technical problems in applying them — aside from the many-body problem. This is especially true for phenomena driven by the strong force. Usually it is much simpler to create a model with a very restricted range of validity, like Chiral Perturbation Theory (CPT) or even use some phenomenological models.

But let us start from the roots of QCD. From the experiments of Rutherford we know that all matter around us resides basically in nuclei. After the work of Yukawa we realized that we need a force to have these nuclei bound and a particle to carry this force — the pion (or π-meson) with quantum numbers $J^{pc} = 0^{-+}$. Soon, however, it was realized that just pions are not enough to bind even light nuclei, making the existence of heavier nuclei absolutely impossible. In order to eliminate the discrepancy between the theory and reality, one had to introduce an additional particle — the sigma meson, with the quantum numbers of the vacuum, $J^{pc} = 0^{++}$. That was a starting point for the long-lasting thriller "Hunting for the σ meson", the story, which is not yet over, so everybody can participate in it either as an actor or as a spectator.

The σ-meson is one of the most mysterious particles ever discussed in hadron physics. Many experiments claimed its observation, and at least as many claimed its absence. From time to time it was included into the Particle Data Group (PDG) booklet — the "Holy Bible" of a particle physics — and at other times it was removed from it as a heresy.

The mass of the σ-meson is one of the biggest "known-unknowns" (even the result of the world soccer championship can be predicted with a higher accuracy than the mass of the σ-meson). Just for comparison: the mass of the pion we know with a 10^{-7} accuracy being $m_{\pi^{\pm}} = 139.57018 \pm 0.00035$ MeV (PDG value). The mass of the σ-meson according to the PDG is $m_{\sigma} = 400 \div 1200$ MeV, i.e. widely unknown. The same situation is found with regards to branching ratios and decay width — despite fifty years of history of the σ-meson. All information from PDG is "$\pi\pi$ decay — dominant; $\gamma\gamma$ decay

— seen", i.e. just two phrases after half a century of enormous theoretical and experimental efforts. On the theoretical side presently most high-rated is the result of Leutwyler et al. [1], based on chiral dynamics and $\pi\pi$ phase shifts, that the σ-meson is the lowest QCD resonance, dynamically generated by $\pi\pi$-rescattering with a mass $m_\sigma = (441 + i272)$ MeV.

Hence it is not a surprise that having the ability to measure the $\pi\pi$ production we decided to look it more carefully especially the two-pion production in *nucleon-nucleon*[a] collisions leading to a bound nuclear system, where one may expect strong medium modifications of the unknown σ-meson properties and where the so-called ABC effect observed also nearly fifty years ago is still missing an explanation.

The following chapter will highlight the history of the ABC effect, in particular the experimental data collected so far on this topic and discuss several theoretical models claimed to explain this phenomenon at various times.

1.1 Experimental results in the ABC field.

The mess with the ABC effect starts in 1960 with the work of *Alexander Abashian, Norman E. Booth and Kenneth M. Crowe*[2]. The observed effect in that paper was called "anomaly in meson production". Only much later the whole class of such effects started to be called ABC effect according to the initials of authors of the fist paper.

The pioneering experiment was performed in Berkeley with a single arm magnetic spectrometer. The resulting measurements with proton beams of different energies and a deuteron gas target exhibited a very unexpected behavior: in the reaction $pd \rightarrow {}^3\text{He} + X$ [b] an enhancement in the invariant mass spectrum of X right at the two-pion threshold was observed, (*Fig. 1—1*). The experiment was performed at four beam energies: *624* MeV*, 648* MeV*, 695* MeV and *743* MeV. The effect was observed at all energies at roughly the same position.
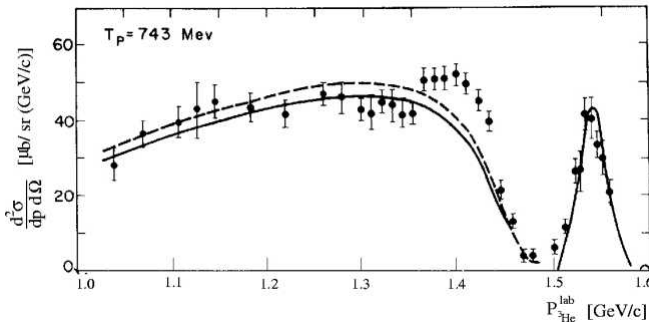
Fig. 1—1 First published figure about ABC effect [2]. The peak at very right position is single pion production. The solid and dashed lines are phase space with different normalization. The enhancement over phase space is called the ABC effect

---

[a] The notation NN is reserved for the Neural Net, except for reaction equations
[b] they measured only the momentum of ${}^3\text{He}$ at one angle, but that is enough to reconstruct the mass of the state X at this angle

In their 1963 paper [3] the same authors added some more information about the ABC effect: one more energy and one more angle. Qualitatively the effect did not change. Later on their experimental results were confirmed and supplemented by other groups: Birmingham[4] (1969) $pn(p_{spec}) \rightarrow d(p_{spec}) + X$ [a]; Saclay[5] (1970) $dp \rightarrow d(p_{spec}) + X$, $dp \rightarrow {}^3He + X$; Saclay[6] (1973) $d + p \rightarrow {}^3He + (mm)^0$; Saclay[7] (1978) $n + p \rightarrow d + (mm)^0$; Saclay [8] (1976) $d + d \rightarrow {}^4He + (mm)^0$ [b].

All of these experiments have several features in common: all of them have been single arm measurements detecting only the heavy outgoing nuclear recoil, i.e. all measurements were inclusive with no possibility to distinguish between $\pi^+\pi^-$ and $\pi^0\pi^0$ contributions or even 3π admixtures. All of these experiments were performed at roughly the same energy, 150-400 MeV above $\pi\pi$ threshold in the CMS[c], at a few fixed angles.

The results are also similar: if the system X is electrically neutral and isoscalar, than there is an ABC effect (bump at 2π threshold), in all other cases no particular enhancement is observed.

Only very recently the first exclusive experiments [9][10] were performed, unfortunately at much lower energy — close to threshold — i.e. far away from the established ABC region. In addition, one experiment [9] had very low statistics, and the other one [10] measured only $pd \rightarrow {}^3He\pi^+\pi^-$, which is not the best suited channel as we will see later.

Hence no exclusive measurements of solid statistics have been available so far in this field. That is why a series of experiments were performed now at CELSIUS/WASA, the results of which are described in this thesis.

1.2 *Theoretical status of the ABC effect*

In the very first paper about ABC [2] it was suggested that the enhancement originates from a strong $\pi\pi$ interaction or even a meson state close to threshold. However, the derived isoscalar $\pi\pi$ scattering length of $a_s = 2.4$ fm was larger by an order of magnitude than that known from other reactions. Later on, in the seventies the idea was born that the excitation of two nucleons into their first excited state, the $\Delta(1232)$ resonance could be the reason for the ABC effect [11].

Since in three-body systems all binary invariant masses are constrained by the relation $M_{12}^2 + M_{23}^2 + M_{31}^2 = const$ for given center of mass energy, this means that a resonance-like structure in M_{12} may show up as a reflection of resonances in M_{23} and M_{31} (two Δs may lead to bumps in the $\pi\pi$ system).

In 1973 the first $\Delta\Delta$ model [11] for the explanation of the ABC effect appeared. In their article [11] Risser and Shuster demonstrated that two multiplicative Δ

---

[a] They used proton beam and deuteron target. Only outgoing deuteron was measured, and the rest proton was assumed to be a spectator.

[b] Here the reactions quoted as in the original papers: mm = X. mm mean that the mass of system X was reconstructed using missing mass technique. Symbol 0 mean that the charge of system X was 0.

[c] CMS — Center of Mass System

propagators lead to a maximum contribution in the reaction cross section for the following two particular configurations if the two nucleons from the decay of the Δs are bound in a nuclear final state:

- the two pions are emitted in parallel from the decaying ΔΔ system, resulting in low $M_{\pi\pi}$ values
- the two pions are emitted in antiparallel from the decaying ΔΔ system, resulting in high $M_{\pi\pi}$ values
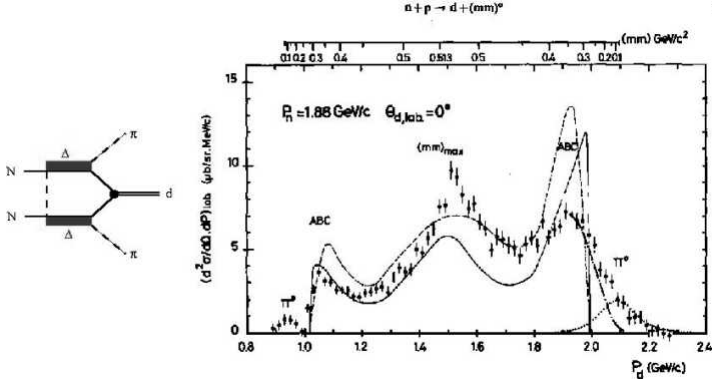

Fig. 1—2 Typical Feynman diagram for Delta-Delta models(left). ABC data [6] for the reaction $np \rightarrow dX$ with some Delta-Delta calculations (right) [from Ref. 12]. Top scale is translation deuteron momentum to deuteron missing mass.

These two constellations triggered by excitation and decay of the ΔΔ system lead to two enhancements in the $\pi\pi$ invariant mass spectrum: one at low $\pi\pi$ invariant masses (pions move in parallel), and one at the high $\pi\pi$ invariant masses (pions move in antiparallel). At low energies, i.e. $\sqrt{s} < 2m_\Delta$ the low-mass enhancement is somewhat preferred kinematically, at $\sqrt{s} > 2m_\Delta$ the high-mass enhancement should dominate. At $\sqrt{s} \approx 2m_\Delta$ both enhancements should be of comparable size. This behavior is further supported by the anisotropy of Δ decay. Indeed the heavy-particle momentum spectra taken for the reactions $np \rightarrow dX$, $pd \rightarrow {}^3\text{He}X$ and $dd \rightarrow {}^4\text{He}X$ all show a three-bump structure (*Fig. 1—2*), with the middle bump belonging to large $\pi\pi$ invariant masses. The bumps at small and large momentum both belong to small $M_{\pi\pi}$ values[a], the first being due to the heavy particle [deuteron] moving backward in the CMS, but forward in the lab system. The high momentum peak of the spectrum belongs to situations, where the heavy particle moves forward both in the CMS and lab systems. On top of *Fig. 1—2* the scale for the invariant mass of the system X is given. Note the largely nonlinear scale, where the low $M_{\pi\pi}$ region (left and right ends) appears compressed and the high $M_{\pi\pi}$ region (middle[b]) stretched. Accordingly, deviations from phase space appear overstated in the low-mass region and understated in the high-mass region. How these deviations from

---

[a] Two pions move parallel
[b] Two pions move antyparallel

phase space show up in the $M_{\pi\pi}$ spectrum having a linear scale in $M_{\pi\pi}$ will be demonstrated in *Chapter 5*.

If the measurements are inclusive, they can not really distinguish between two-pion production, three-pion production, and also other meson production as, e.g., η production, which all may contaminate the spectrum. In Ref. [12] it has been suspected that the central peak in the momentum spectrum could actually originate from three-pion and η production, (*Fig. 1—3*).
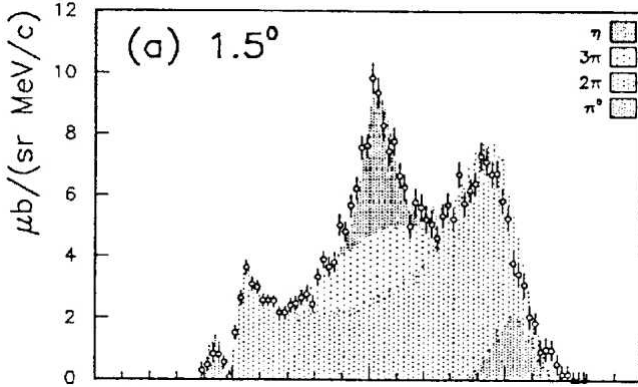
Fig. 1—3 Reaction decomposition of $np \rightarrow d + (mm)^0$ data from [12]. P_d

As already noted there, this would imply a serious problem for the interpretation of the ABC effect by the $\Delta\Delta$ model. However all other publications, in particularly theoretical papers, disregarded this warning. As will be shown the first exclusive measurements to this topic, which have been carried out at CELSIUS-WASA and which are the subject of this work, reveal this middle structure not to be of $\pi\pi$ origin. Therefore the $\Delta\Delta$ model interpretation believed to be the proper explanation of the ABC effect is at variance with the true $\pi\pi$ production data, as will be demonstrated in the following chapters.

2 Experimental setup

This chapter briefly describes the place, where our experiment was performed as well as the techniques used. The description of the detector components can also be found in this chapter.

2.1 The Theodor Svedberg Laboratory (TSL)

The experiment was performed at the national Swedish accelerator facility in Uppsala, the Theodor Svedberg Laboratory, *Fig. 2—1*. The Gustaf Werner cyclotron provides accelerated ion beams starting from protons up to xenon and can deliver them to different research areas, including CELSIUS storage ring, see *Chapter2.2,* where our experiment took place.
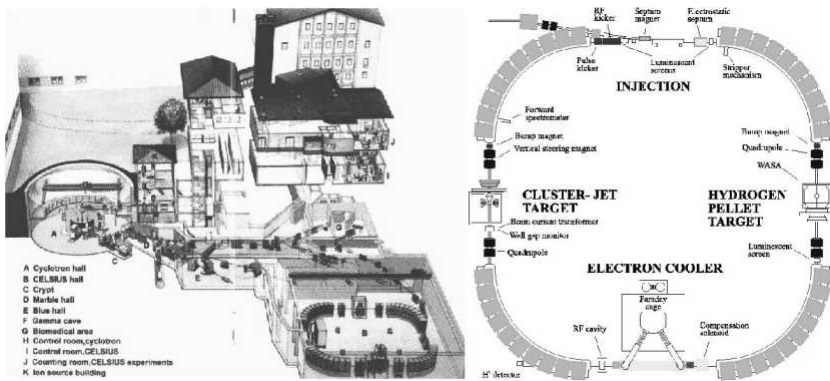

Fig. 2—1 The cross section of the TSL. The cyclotron and CELSIUS laboratories are visible, placed underground (left). Setup of The CELSIUS storage ring (right)

2.2 The CELSIUS accelerator and storage ring

The name CELSIUS originate from Cooling with Electrons and Storing Ions from Uppsala Synchro-cyclotron, *Fig. 2—1*.

The magnets for the ring originally come from the ICE experiment, CERN. The maximum kinetic energy available for protons is 1450 MeV, however it is possible to cool protons only up to an energy of 550 MeV. It is also possible to store heavier ions up to Ar with maximum energy of 470 MeV/A. We are only interested in protons and deuterons, because at CELSIUS energies it is not possible to get two-pion production with heavier projectiles. The highest achieved deuteron energy was 1015 MeV (June 2005). To calculate the luminosity one needs two more numbers about CESLIUS — Circumference (81.8m) and typical number of stored particles (protons $\propto 1\times10^{11}$; deuterons $\propto 1\times10^{10}$). All other information can be found in Ref. [13].

2.3 The pellet target

A crucial part of WASA[14] is the pellet target system. Since the main goal of the CELSIUS/WASA detector was measuring of rare decays of the η-meson, one had certain requirements to the detector and the target system:

- The detector should cover a solid angle of close to 4π
- The density of a hydrogen/deuterium target should be as high as possible.
- The background coming from the target system should be as small as possible.

These three points rule out most of the target systems except for pellet target, *Fig. 2—2*.

The pellet target works in the following way: the gas (in our case hydrogen or deuterium) is liquidized; then in the pellet generator the jet out of this gas is created and brakes down into droplets by the acoustic excitation. The droplets are uniform in size and in spacing. After that the droplets freeze by evaporation in the droplet chamber, *Fig. 2—2, right*. So in the vacuum chamber we have solid spheres of frozen gas with a size of 25-35 μm, coming down with a frequency 5-12 kHz. More information about the pellet target can be found in [15].
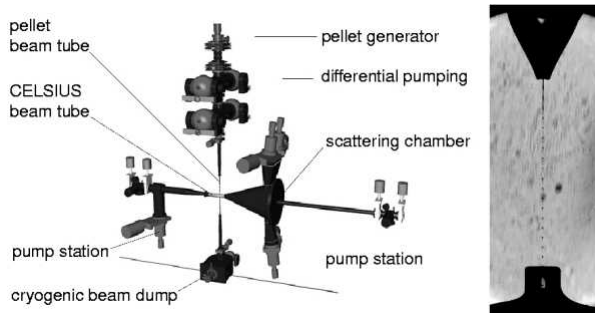

Fig. 2—2 Left: schematic view of the target system; Right: photo of the droplet chamber

2.4 The WASA detector

As mentioned in the preceding section, there have been several requirements for the WASA detector design. In addition to the three, which influenced the choice of pellet system, one can name:

- measurement of the energy and the angles of all tracks
- the ability to work with high luminosities (more than $10^{32}\,\mathrm{cm}^{-2}\mathrm{s}^{-1}$)
- low-Z detector material to reduce hadronic interactions of protons and to measure neutrons.
- high-Z detector material to measure photons efficiently.

Some of these requirements contradict each other, so there had to be a compromise solution. As a result of such compromises the WASA detector was constructed, *Fig. 2—3*: It consists of 3 parts: Forward Detector, Central Detector, Zero Degree detector.

The Forward Detector (FD) is optimized for measuring protons from the $pp \rightarrow pp\eta$ reaction. It also has some efficiency for measuring neutrons. It provides energy and angular information for charged particles with good precision, and also some

angular information for neutrons. The first level trigger also relies on the FD, because it incorporates several layers of thin fast plastic scintillator detectors. The FD is also well suited for measuring charged target recoil particles and rescattered projectiles. It is also important for our case that it can trigger and detect ³He. As a drawback of such a solution the forward detector can not effectively detect photons.
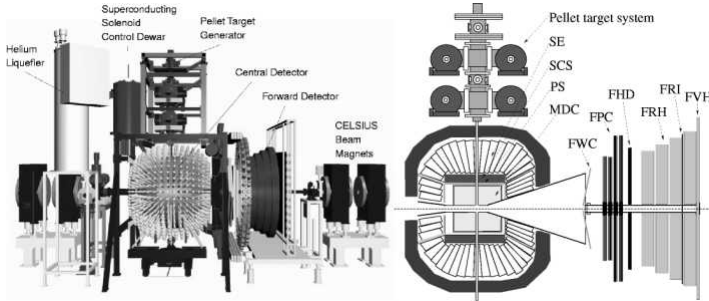

Fig. 2—3 The 3D and the cut view of the WASA detector

The Central detector on the other hand is optimized to detect mesons and their decay products. That is why it also has to measure photons, as a consequence we have a large electromagnetic calorimeter. A magnetic field is also important to distinguish positively and negatively charged particles, that is why the solenoid is present. The individual detector components will be discussed in the following chapter.

2.4.1 The Forward Detector (FD)

The Forward Detector as noted before is suited for precise measurements of charged particles. It covers the range of polar angles $3° < \Theta < 18°$. The angular resolution provided by the FPC (*Forward Proportional Chamber*), see *Chapter 2.4.1.2,* can be better than $0.2°$. The best energy resolution will be achieved, when particles stop in the FD, i.e., $T < 0.4$ GeV for deuterons, 0.3 GeV for protons and 0.17 GeV for pions. For the particles which punch through the FD, the energy can also be reconstructed, but with larger errors. For protons with energy below 0.3 GeV the relative uncertainty is roughly constant and about 3% and rises linearly with higher energy reaching 20% at 1 GeV. For deuterons the relative energy error is roughly the same, but they are much more difficult to identify uniquely.

Unfortunately it is hardly possible to reconstruct the energy of punch-through pions, since already at 0.3 GeV they deposit an energy like minimum ionizing particles. The situation with electrons is even worse.

For ³He and α particles the stopping power is 0.9 GeV, lower than the maximum available energy for these particles at CELSIUS. The most limiting factor in the case of ³He appears to be not the highest but the lowest energy: ³He particles with energy below 0.2 GeV stop before the FRH (*Forward Range Hodoscop*, see *Chapter 2.4.1.4*), that is why a precise energy determination is hardly possible for them.

2.4.1.1 The **F**orward **W**indow **C**ounter (FWC)

The FWC is the first layer of the forward detector. It consists of 12 plastic scintillator elements, each 5 mm thick, *Fig. 2—4*.
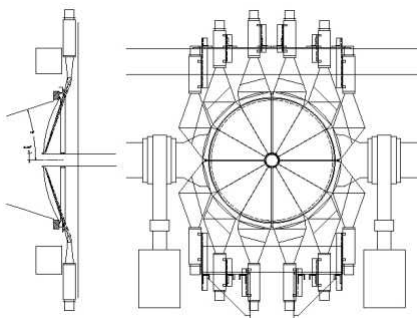

Fig. 2—4 Schematic representation of the FWC. Left: side view, right: front view.

All elements are inclined by approximately 10° with respect to the vertical position. This is in order to follow the window of the scattering chamber. The main purpose of FWC is to suppress the background coming from *beam—beampipe* interactions. It is also used in the first level trigger logic, because it is small and fast. In our case it was used in the trigger also for inducing a high threshold on deposited energies in order to separate ^{3}He from protons and deuterons.

2.4.1.2 The **F**orward **P**roportional **C**hamber (FPC)

The FPC[16],[14] (tracker) is used to determine the coordinates of charged tracks at a distance of 1100 mm downstream of the vertex position, *Fig. 2—5*.
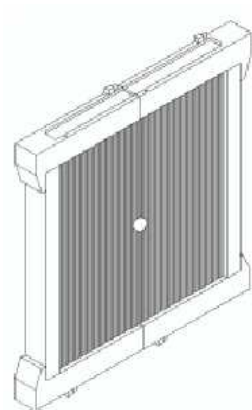

Fig. 2—5 Schematic view of one module of the FPC

Initially four modules were built, but only two of them had been installed. At a later stage the third module was installed, too, and in the ^{3}He runs, three modules were in use. According to the original design one module should measure the horizontal position, one the vertical one and two modules the positions along two diagonals. Each module consists of straws: 122 straws in one layer, each second layer straggled by the radius of a straw (4 mm) thus leaving no gaps in the sensitive area. The straws are cylindrical drift tubes made of aluminized Mylar foil with central sensitive resistive wire. Just by geometrical overlap one can reach an angular resolution of 0.2°. In addition it is possible to use drift times to improve the spatial resolution from 8 mm to 200 µm, and use of the resistive wire can help for position determination just from one module along without overlap with several other modules. This feature might be important at high energy high, luminosity runs for resolving tracks from different high multiplicity events for WASA at COSY[a].

2.4.1.3 The Forward Hodoscope (FHD)

The FHD [17],[18] (so called "Juelich hodoscope", named after the place of manufacture), is one of the main components of FD, especially for the ^{3}He analysis.

It consists of three layers, *Fig. 2—6*. The third one is pizza-like, segmented into 48 elements. The first and second planes are Archimedean spirals consisting of 24 elements each. All three layers are plastic scintillators 5 mm thick each. The FHD fully cover the circles with radius 580 mm, with inner hole of 48 mm diameter.
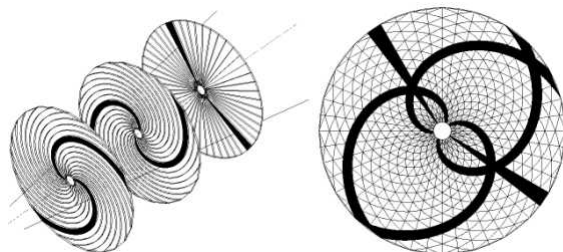

Fig. 2—6 Design of the FHD. Two tracks pass the detector, each hits one element in each plane. Due to their different geometry (left and right Archimedean spirals as well as straight elements), it is possible to reconstruct the hit position by the intersection of all 3 layers.

The FHD is a working horse of the WASA detector. It is used:
- to distinguish charged and neutral particles in forward direction (neutrals do not give a signal in the thin plastic detector: for neutrons the probability to create a signal in FHD is about 0.5% on average — strongly depending on energy; the probability for photons is even lower).
- as a first level trigger, to settle the charge multiplicity conditions.
- for particle identification (particle ID) via *dE—E* techniques (in case of ^{3}He at 895 MeV beam energy it is the only possibility to select Helium).

---

[a] Next generation experiment with upgraded WASA detector at COSY facility in Juelich, Germany.

- to use also coordinate information from FHD (θ, ϕ) for a smart Missing Mass trigger for the WASA at COSY program.

Despite of all these nice features, some unpleasant effects appeared during the work with FHD: Since FHD was manufactured more than 10 years ago, the aging effects got meanwhile big and different for different elements; in addition the photo-multiplier response is not linear. These two deficiencies make the work with FHD presently much more difficult than it could be.

2.4.1.4 The **F**orward **R**ange **H**odoscope (FRH)

The FRH, *Fig. 2—7,* is the largest and heaviest sensitive part of the forward detector.

It consists of four layers each 110 mm thick. Each layer incorporates 24 elements (covering $\Delta\phi = 15°$ per element, ϕ being the azimuthal angle) and is constructed in such a manner that one FRH element covers 2 elements of FHD3. This is to simplify tracking at the trigger level. The main purpose of the FRH is a precise energy reconstruction, although it is also used for particle ID. The layered design allows to consider many ΔE-E combinations, which are important for complicated cases. Due to this design it is also possible to reconstruct the energy of a particle even if it undergoes hadronic interaction [19].
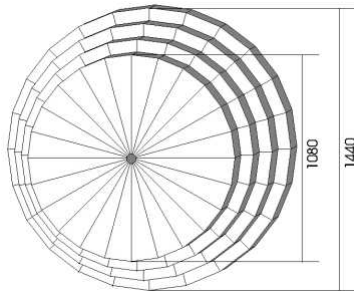
Fig. 2—7 Principal scheme of the FRH with all four layers. The diameter of the first and the last layer are given in mm.

2.4.1.5 The **F**orward **R**ange **I**ntermediate Hodoscope (FRI)

The FRI [20] (sometimes wrongly named Forward Range Interleaving hodoscope) is placed between the third and fourth layer of the FRH. It consists of 32 bars of 5 mm thick plastic scintillator rotated by 90° with respect to each other and forming thus rectangular pixels, *Fig. 2—8*. The widths of the bars are 60 mm for the outer region (10+10) and 30 mm close to the beam pipe (6 and 6 — narrow bars are spitted due to beam pipe).

Fig. 2—8 Scheme of the Forward Range Intermediate hodoscope.

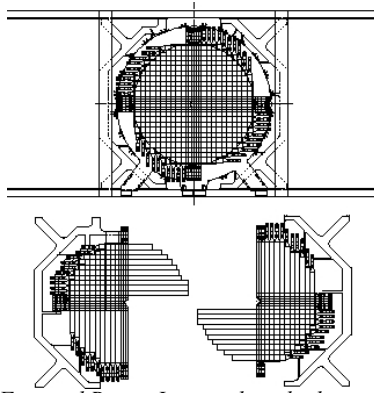The main purpose of the FRI is to measure the angle of neutrons by detecting the position of recoil protons. It also can improve the position information for charged tracks, and provide additional information for chance coincident separation, since it is extremely fast. At present the limiting factor for time resolution of FRI is the time resolution of TDCs. Unfortunately it was not included at trigger level, but it is proposed to do so for WASA at COSY. With better TDCs one can also think about Time Of Flight analysis at the base FWC—FRI, which is more than 1000 mm long.

2.4.1.6 The **F**orward **V**eto **H**odoscope (FVH)

The FVH [21] is the last but not the least part of the FD. It consists of 12 bars 20 mm thick, 137 mm high and 1650 mm wide *Fig. 2—9*. It is widely used to select punch-through particles at trigger level as well as for energy reconstruction. Due to the readout on both ends, one can determine both x and y hit positions, improving the position of the track.
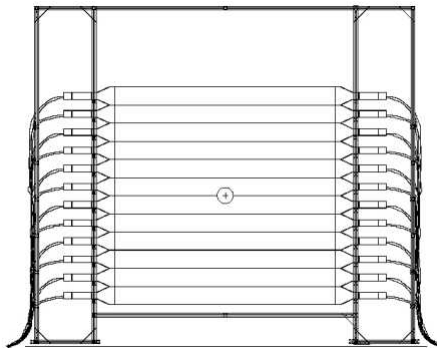

Fig. 2—9 Schematic view of the Forward Veto Hodoscpoe, together with its support structure

2.4.2 The <u>C</u>entral <u>D</u>etector (CD)

For the design of the CD there were hard requirements, which were difficult to fulfill. The main task is to measure both charged and neutral particles with high precision. To measure the charge one needs a magnetic field. The respective magnet can be placed before or behind the electromagnetic calorimeter. In the latter case the whole calorimeter is placed in the magnetic field, and therefore one can not use conventional photomultipliers, but photodiodes, like e.g., the CMS CERN collaboration. However the energy resolution of photodiodes is much worse than that of photomultipliers. So this solution was not acceptable. The other case is also not much better: if one places the magnet in front of the calorimeter, then one has much high-Z material in front — many photons will be converted before they would reach the calorimeter. An optimal solution was found for the WASA case — a thin wall superconducting solenoid. It allows on the one hand to place it before the electromagnetic calorimeter, and on the other hand it is thin, i.e. there is not so much material to convert photons.

The momentum of charged particles can be measured by a drift chamber (one can measure θ, ϕ at the vertex and the momentum by the curvature of the track in the magnetic field). Photons create clusters in the calorimeter and can thus be reconstructed (also θ, ϕ and Energy) as described in the following.

2.4.2.1 The <u>M</u>ini <u>D</u>rift <u>C</u>hamber (MDC)

The MDC [22] is the first part of the CD. This cylindrical drift chamber consists of 17 layers of drift tubes (1738 tubes). It covers polar angles from 24° to 159°. The diameter of drift tubes varies: the first 5 layers have 4 mm; the next 6 layers have 6 mm and the last 6 layers have a diameter of 8 mm. The tubes are made of Mylar foil coated with aluminum on the inner side. The layers are located at radii between 41 and 203 mm. The tubes in nine layers are parallel to beam axis and in eight other skewed by a small angle (6°-9°) with respect to beam axis, *Fig. 2—10*.

The main purpose of the MDC is to provide vertex position, polar and azimuth angles at the vertex, as well as the momentum of charged particles.
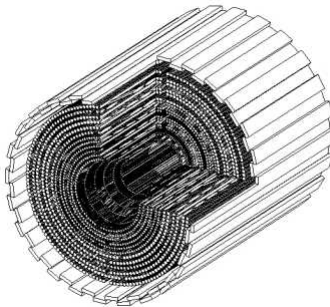

Fig. 2—10 Cut view of the MDC surrounded by the PS barrel (seen from the back side).

2.4.2.2 The <u>P</u>lastic <u>S</u>cintillator Barrel (PS)

The PS [22] is a cylindrical detector surrounding the MDC. It contains three independent parts: forward (PSF), central (PSC) and backward (PSB).Both PSF and PSB are divided into 48 straight sectors. The PSC is made of bars. Due to the pellet target tubes the top and the bottom bars are divided into two half's, *Fig. 2—11*.
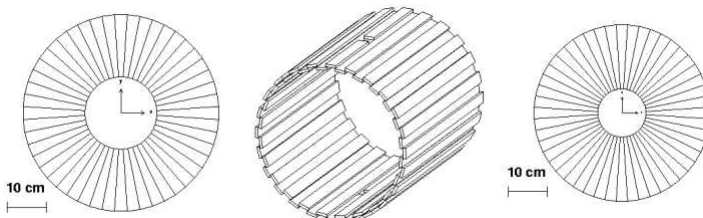

Fig. 2—11 Plastic Scintillator barrel: left — forward part; middle — central; right — backward part

That is why the number of elements is not 48 but 50. The light from the PSC is read out from the back side (except for two elements). All three parts have been manufactured from the same 8 mm thick plastic scintillator.

The main purpose of the PS is triggering (number of charged particles in CD). But it is also used for particle identification via *dE-E* and *dE-P* plots. Additionally it provide the time zero t_0 for the MDC.

2.4.2.3 The <u>S</u>uper<u>c</u>onducting <u>S</u>olenoid (SCS)

The SCS is an ultra-thin walled superconducting solenoid. It is as thin as 0.18 radiation lengths. The maximum available magnetic field is 1.3 T, but most of CELSIUS/WASA runs were performed with a magnetic field of 1 T. It has to be cooled down to 4.5° K by the helium refrigerator. The field is confined by the iron yoke, which provides magnetic field protection for the PMT's of the Scintillating Electromagnetic Calorimeter.

2.4.2.4 The <u>S</u>cintillating <u>E</u>lectromagnetic Calorimeter (SE)

The most outer layer of the CD is the SE calorimeter [23].It has 3 parts: forward (SEF), central (SEC) and backward (SEB), *Fig. 2—12*.

In total it has 1012 *Na* doped *CsI* crystals. The crystals of each part are of different shape and size.
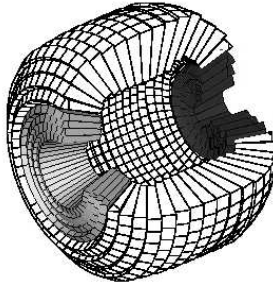
Fig. 2—12 The scheme of the Scintillating Electromagnetic calorimeter. From left to right: forward, central, backward parts — all marked by different colors.

The main purpose of the SE is a precise energy determination for both charged and neutral particles, in particular for the latter ones, since for charged particles one can get a similar information from MDC. It is also used at the second level triggering, either to determine the number of clusters or for a total energy calculation.

2.4.3 The Zero-degree detector

The Zero-degree detector is the smallest part of the CELSIUS/WASA detector setup. In our beam time it was used for tagging of ^{3}He from the reaction $pd \rightarrow {}^3$Heη. Since the measurements were performed close to the η threshold, all ^{3}He particles resulting from such a reaction emerge with angles below 2° in the lab frame and reach the ZD detector.

For the momentum selection one uses dipole magnets from the CELSIUS ring. Since ^{3}He^{++} is much heavier and much slower compared to beam particles, it has a higher curvature in the magnetic field of dipoles, which allows to measure it in the germanium spectrometer. To increase the acceptance for $pd \rightarrow {}^3$Heη tagging, one had to defocus the beam by quadrupoles. That is why the overall quality of the beam was a bit worse than it could have been.

A detailed description of the Zero-degree detector can be found in [24].
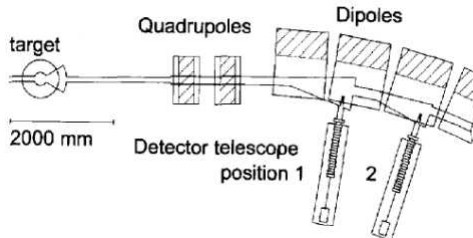
Fig. 2—13 The Zero-degree detector. 1 and 2 are germanium telescopes.

2.4.4 The Data Acquisition System (DAQ) and the Trigger system.

Since WASA is a very complicated detector, the data acquisition system is also complicated. One can find a detailed description in [25]. To get some impression of how it looks like one can examine *Fig. 2—14* and *Fig. 2—15*.

Fig. 2—14 Principal scheme of the Data Acquisition System

Fig. 2—15 Principal Scheme of the trigger system.

3 Analysis Tools

3.1 Theoretical aspects of Neural Nets

Since quite a big part of the analysis is done via Neural Nets, the basic aspects as well as possible applications will be described in this chapter.

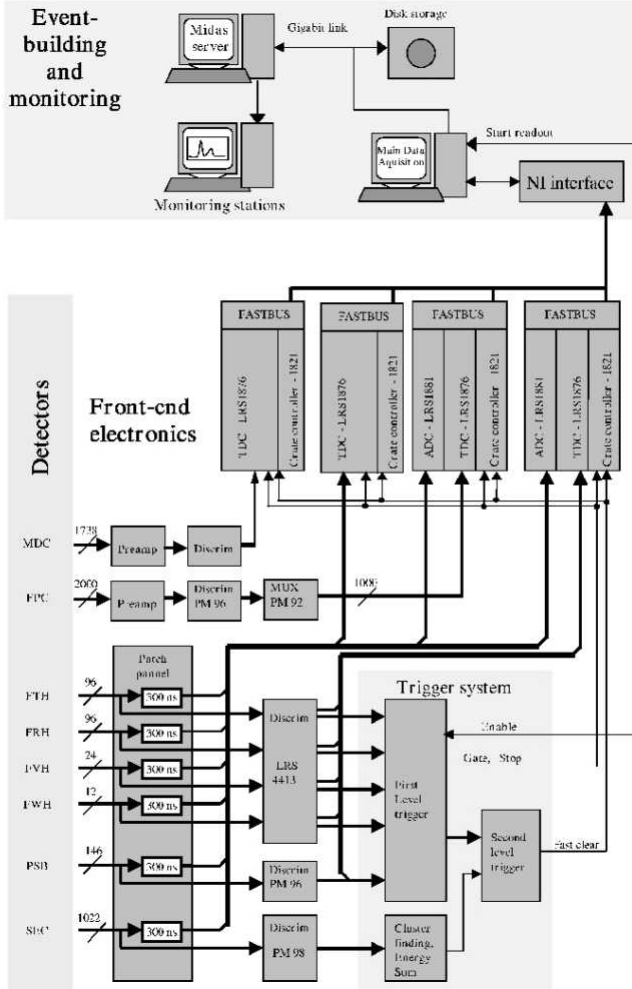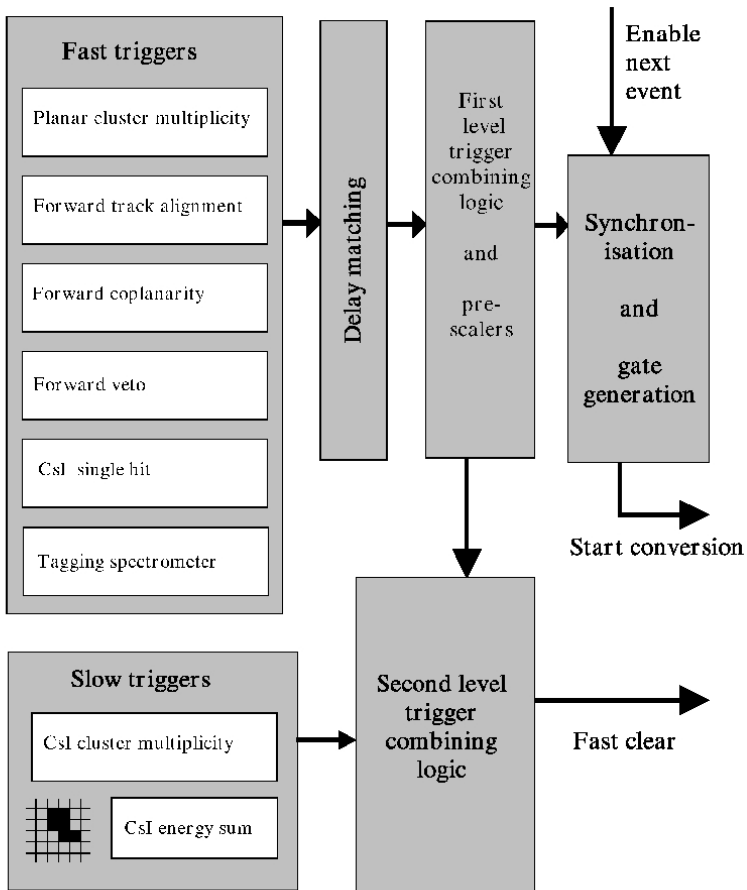The study of Neural Nets started by the pioneering work of McCulloch and Pitts in 1940. Later on it was shown that any continuous function can be approximated arbitrarily close by Neural Net (*universal approximation theorem*). By translating from the mathematical language to a real one it means that any task can be solved by Neural Net with any desired accuracy. As usual, mathematicians proved that it is possible, but did not say anything on how to do it. Fortunately, since then a lot of works appeared on how to use it in reality. In this dissertation a possible way of applying it for *Particle ID* and *Calibration* purposes will be demonstrated.

3.1.1 Neural Nets! Why and how.

Neural Networks, or Artificial Neural Networks have been motivated by the observation that the human brain computes in a different way compared to present day digital computers with *von Neumann* logic. The brain is a highly nonlinear and parallel computer. It can organize its constituents (*neurons Fig. 3—1*) in such a way that it allows to perform computational tasks many times faster than any existing digital computer.

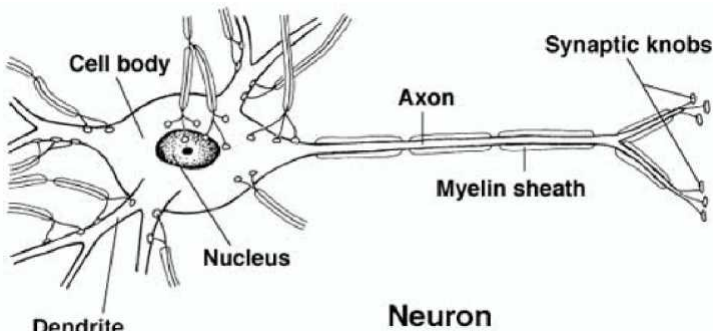*Fig. 3—1 Sketch of a real human neuron*

In its most general form the neural net is a tool to model the way in which our brain performs some tasks. For our case the most important one is the following property of the neural net: it can learn an input-output mapping.

The artificial neuron, *Fig. 3—2,* is a primitive model of a real one, but it allows to design artificial neural nets and perform some computations.
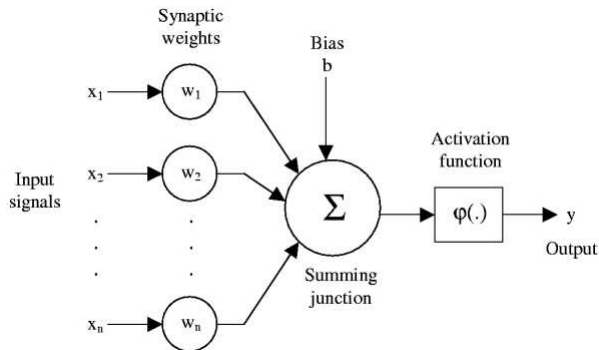
Fig. 3—2 Most common view of an artificial neuron

In mathematical terms we may describe neurons as $y = \phi(\sum_{j=1}^{n} w_j x_j + b)$, where x_j are the inputs, w_j are the weights of corresponding synapses and the ϕ is the activation function and b plays the role of an offset. There are a lot of different possible activation functions described in the literature: step function, linear, sigmoid, hyperbolic tangents… In our case we use Sigmoid[a], i.e. $f(x) = \dfrac{1}{1+e^{-x}}$, see *Fig. 3—3*:
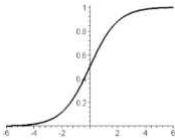
Fig. 3—3 Sigmoid activation function

There are several architectures of neural nets. In this work we will use only Feed Forward neural nets, as shown in *Fig. 3—4*.

Fig. 3—4 Typical view of a Feed Forward neural net

---

[a] Since it is smooth, symmetric around 0 and finite, the NN based on such activation function can be taught easier as compared to many others. It also fits to our task.

Feed forward means that a layer of neurons is connected only to the next layer of neurons. In such a design there are no loops and cycles. It is the simplest kind of NN, but for our case it is sufficient.

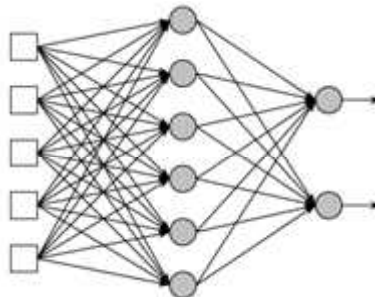The topology (number of inputs, outputs and intermediate (hidden) layers) of a NN is designed for each task separately. The number of inputs and outputs are usually not a problem: put in all you have and get out what you want. But the decision about hidden layers is complicated. There is no prescription on how to choose the network topology, but there are some empirical rules which help sometimes: The number of hidden layers roughly corresponds to nonlinearities existent in your task — the more nonlinear the task, the more layers you need, but the more layers you take, the more difficult it is to train the NN. Basically with more than 3 layers most of the algorithms can not teach the NN reasonably well. The number of neurons in one layer is arbitrary, but usually it should not exceed the number of neurons in the previous layer more than twice plus one. Usually it works, although one of our NN does not obey such a rule. The reason for that will be described in *Section3.2.3.1*.

Another rule on how to try the appropriate number of neurons: not the number of neurons is essential, but the relations between layers, for example: odd-even-odd, or even-even-even. It is better to decide first which combination converges faster with few neurons (which is usually task dependent), and only then play with the number of neurons.

3.2   *Software packages*

For the data analysis the CELSIUS/WASA Offline program [26] was used. It incorporates the full detector simulation (WMC — Wasa Monte Carlo) and track/event reconstruction routines (W4P — Wasa 4π) based on Fortran under Unix/Linux.

However the *W4P* package is used only for track finding and energy reconstruction, all later analysis is done by several C/C++ routines for the simplification of the analysis, and to make it faster. So after the *W4P* program all tracks as well as additional event information (event number, triggers, etc.) are stored in ntuples/ root[a] TTree's for further processing. Unfortunately some features are not implemented in *W4P* code, so they are applied at later stages.

For Monte Carlo simulations, the standard ROOT Phase Space Generator was applied. All additional model corrections to Phase Space were done within ROOT framework.

3.2.1 Ntuple Track Format (NTF).

The Ntuple Track Format was made to separate hit analysis and track processing from each day analysis. In this paradigm one should analyze events by *W4P* and store these tracks in track format (root TTree). Then later analysis can be started already from tracks and no longer from the detector information. So if you today analyze $pp \rightarrow pp\pi^0$ and tomorrow you want to analyze $pp \rightarrow pp\pi^0\pi^0$, then you can make it faster, because you will skip such time consuming parts as hit processing and track

---

[a] root.cern.ch

finding. In addition you are always sure that the analysis is done with the same procedure, which is important, e.g., for deriving correct total cross-sections.

To see what type of analysis can be performed with this NTF one should look into its diagramatic description below. The idea of such a format is taken from the ALICE track format [27].

```
Track
 ├─ θ
 ├─ ϕ
 ├─ TDC
 └─ E_dep
      ├─ FWC
      ├─ FHD1
      ├─ FHD2
      ├─ FHD3
      ├─ FRH1
      ├─ FRH2
      ├─ FRH3
      ├─ FRH4
      ├─ FVC
      ├─ Momentum from MDC
      ├─ PS
      └─ SE
```
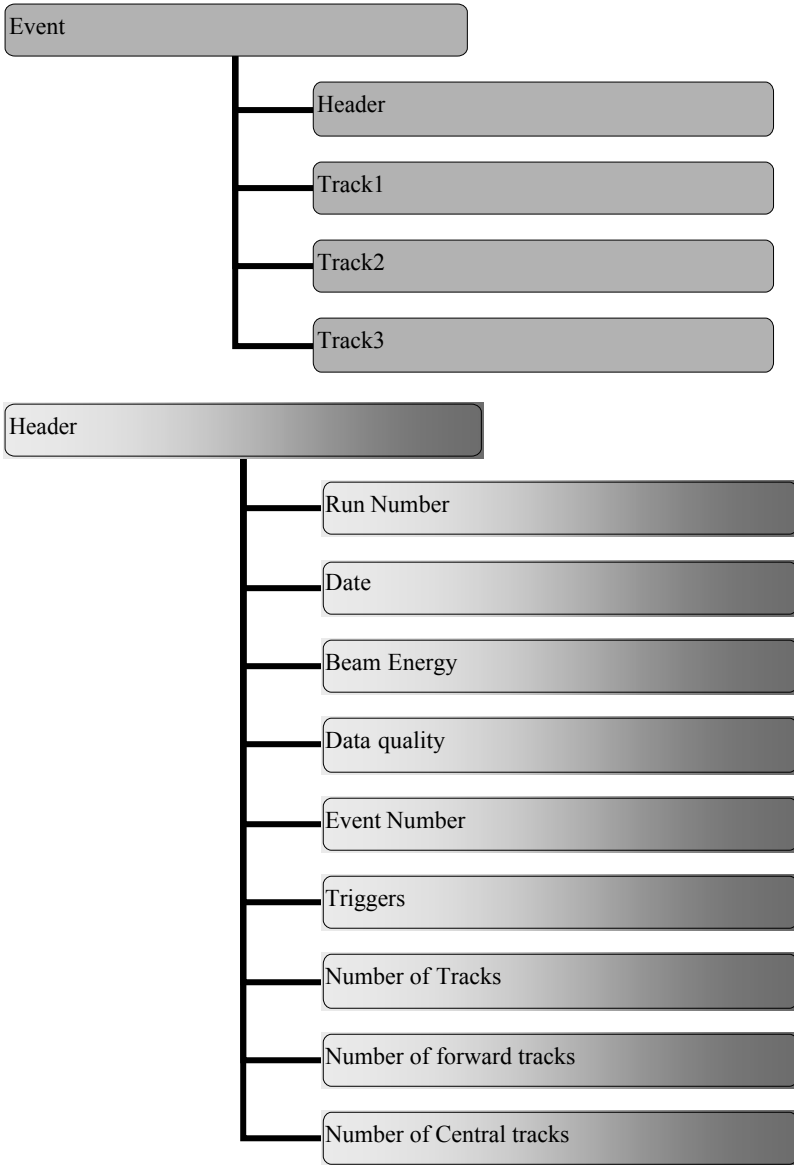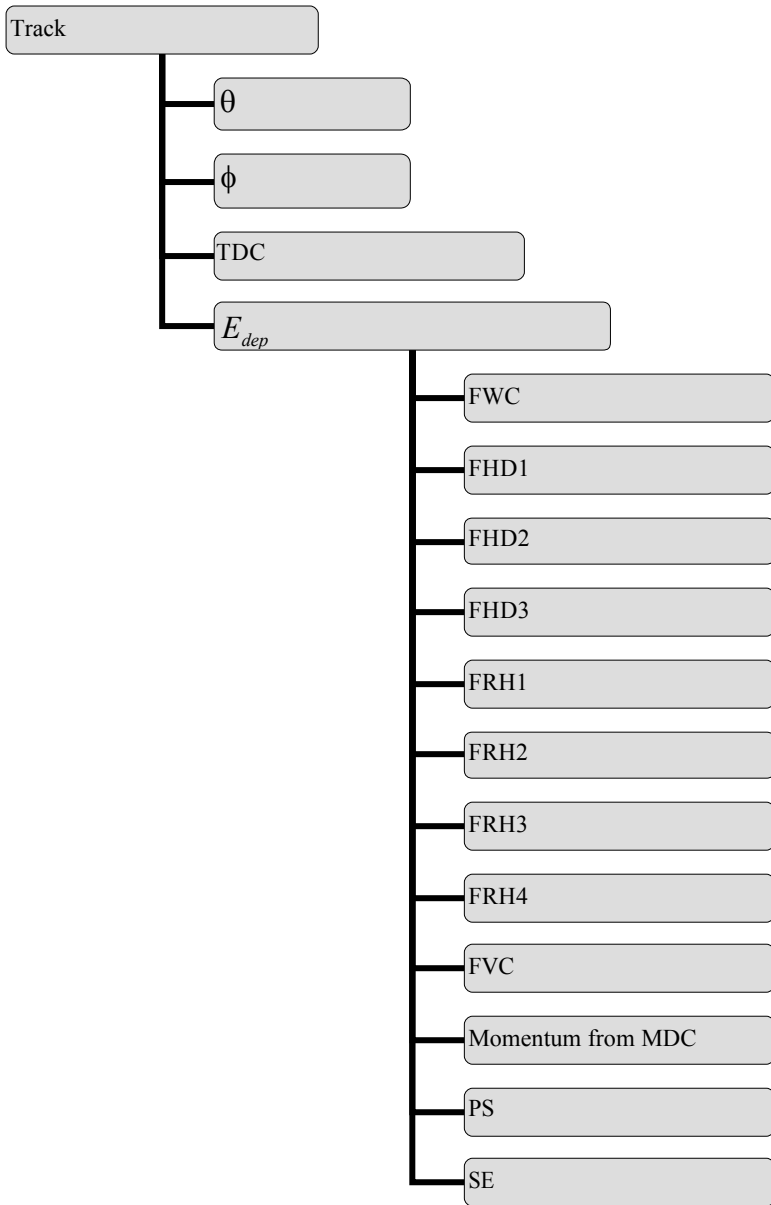
The number of tracks is variable. For forward tracks information from CD does not exist, for central ones the situation is opposite. Such reduced amount of information then allows all kind of high-level analysis. Due to its simplicity any analysis routines can be written by the programmer with knowledge of C/C++. It is also rather compact and

that is why the storage of data in such format is not very space consuming. The amount of required space varies from energy to energy: the higher the energy, the higher the multiplicity and the larger the event size. For the highest energies the average event size in the root file without zipping is 0.3kb/event. After further processing one adds additional branches to each track: mass M, kinetic energy E_{kin}, momentum P with

$$E = E_{kin} + M \quad \text{and} \quad E^2 = P^2 + M^2 c^4 \, .$$

3.2.2 Event processing after *W4P*

Unfortunately, not everything is included in the *W4P* program. That is why one needs to make some corrections and recalculations afterwards. Some of them have a very simple reason: the particle ID by definition is not included in *W4P,* so all corrections, which can be performed only with known particle ID, are not yet carried out.

3.2.3 Particle Identification

With WASA one can classify all possible tracks into four different track types:
Forward Charged track: Charged particles going into the FD should give signals in the thin plastic scintillators (FWC FHD1-3). Additionally it is required to have a signal at least in the first layer of the FRH.
Forward Neutral tracks: Neutral tracks (neutrons and photons) should not give a signal in thin plastics, but may create signals in the thick ones.
Central Charged tracks: As in the forward part, central charged tracks should give a signal in thin plastic scintillators (PS). As a matter of fact they also should give a signal in the MDC, but since the MDC efficiency is about 75% only, some tracks may not have a MDC signal.
Central Neutral tracks: Such tracks should not have a signal in MDC and PS, only in SE.

Let us consider the first type first. Actually all other particles are identified in a rather similar way.

3.2.3.1 Forward Charged Particles

As we see from the description of the WASA detector *Fig. 2—3* and particular its forward part description, *Chapter2.4.1,* there are only plastic scintillators available for the particle ID in the forward detector. Time of flight and momentum determinations via curvature in a magnetic field are not possible in the present design. So the only way to perform particle ID in the FD is via *dE-dE* plots, i.e. energy loss measurements in different layers of FD hodoscopes *Fig. 3—5*. But we have 11 layers of different plastic scintillators, which give $2^n - C_n^1 - C_n^n$ possible *dE-dE* plots (C_j^i is the number of permutations from *j* by *i*). Since in our case *n=11* we have 2024 plots.

The most common and simplest technique is to set boundaries ("bananas") around each of such particle branches. In proton-proton runs we usually have 4 types of charged reaction products: *e*, π, *p* and *d*. Each particle type needs upper and lower boundaries. Each boundary can be parameterized with 4 constants. So we have $4 \times 2 \times 4 = 32$ constants per plot. Since calibration constants are not perfect, one needs to vary boundaries from run period to run period. Even if one does not use all 2024 *dE-E*

combinations, it is a tremendous amount of boring hand work. Hence at first a routine which finds such conditions automatically was developed, but it did not simplify things much. For example on some plots deuterons may look like deuterons, but on others like protons, because they easily may break up in the detector. In addition all the particles can undergo hadronic interactions, and deposit energies different from that expected by the Bethe-Bloch formula.
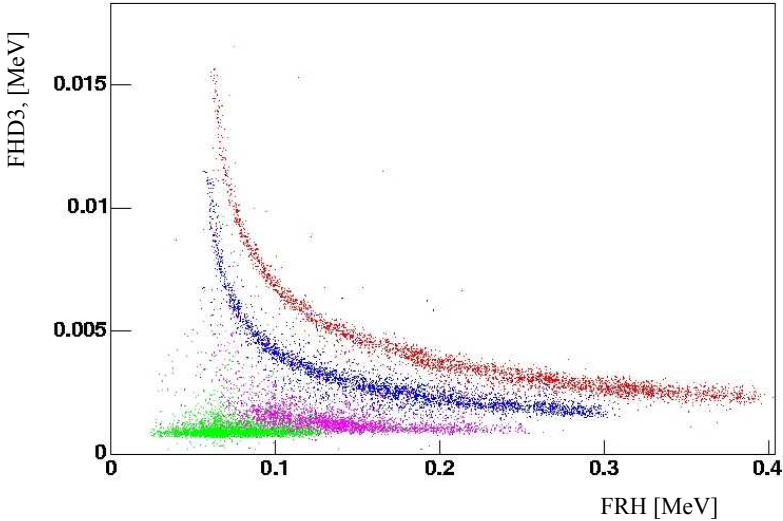

Fig. 3—5 Typical dE-dE plot, here for the case FHD3 vs. FRH. The different bands marked by different colors are (from top to bottom) deuterons, protons, pions, electrons.(MC simulation)

All these problems make the situation much more difficult, especially during the run period, when you need to judge immediately, whether the data collection is reasonably well within expectation. Hence it was decided to employ a neural net for that task, as a particularly reliable method

First we have to consider the topology. The number of inputs is not a problem: Energy deposition from all plastic forward layers (except of FRI and only yes/no signal from FVH) plus Θ angle. This means 10 inputs. The number of outputs is also not a problem: 4 — the probability to be *deuteron, proton, pion, electron*[a]. The number of hidden layers was chosen as one. Apparently it is enough. The final number of neurons in the hidden layer is chosen to be 525, *Fig. 3—6*.

---

[a] At the time when it was decided to make such routine, *pd* or *dd* runs were not even considered. That is why ^{3}He and ^{4}He are not in the outputs. Fortunately they can be nicely separated even without neural net because of their double charge
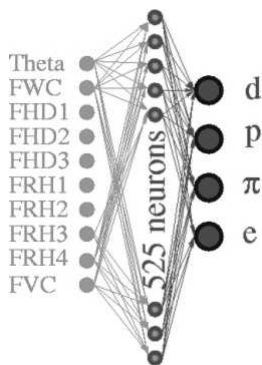
Fig. 3—6 Neural net for the particle identification of the forward going charged particles.

As one can see from the figure such a neural net does not obey a rule mentioned above. According to that rule the number of neurons in the intermediate layer should not exceed 21.

The reason for such deviation from the rule is following: the neural net was taught by the *backpropagation of errors* method. The number of teaching cycles (epochs) can be varied — the larger the number of epochs the lower the errors. But if the number of epochs gets too big, the network becomes overtaught and gives totally wrong results. However, the larger the NN, the more epochs one can train. So at some size an appropriate accuracy can be reached, before the NN becomes overtaught.

For this work the Neural Net package made by *J.P. Ernenwein*[28] was used. And the teaching was done using the MonteCarlo events. One should also mention despite the fact that the probability of each single particle to be a particle of certain type varies [0,1], the overall probability (sum of single probabilities) might exceed 1, or be smaller. It is clear that if one takes some "rubbish track", then the probability to be a particle of any kind is 0, so the sum of all probabilities is also 0, and not 1.

As one of the results of the NN separation one can look at the *Fig. 3—5.* Different colors denote different particles according to NN.
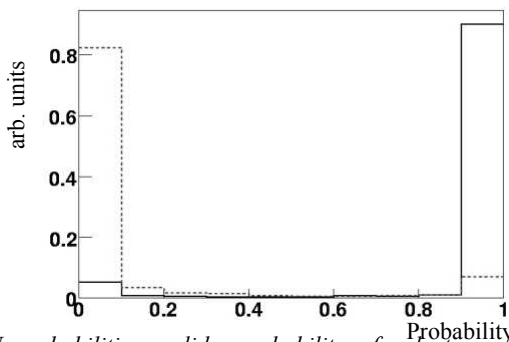

Fig. 3—7 NN probabilities: solid - probability of a deuteron to be identified as a deuteron; dashed — probability of a deuteron to be identified as a proton.

From *Fig. 3—7*, which gives the probability for deuteron identification as an example, one can see that the NN mostly identified deuterons as deuterons. So if we set the following condition: the probability to be a deuteron should be more than 80% and probability to be any other particle should be less than 20%, than we would get 95% purity with 91% selection accuracy. Under that condition 9% of our particles would be unidentified, but among the identified ones there would be all deuterons with a 95% confidence level. By varying that condition one can vary the purity of the particle identifications (changing the efficiency at the same time). This is quite important for an estimation of systematics, which is hardly possible with the usual "banana cut" algorithm.

3.2.3.2 Charged particles in Central Detector.

Following the procedure described in *Chapter3.2.3.1* one can also construct a neural net for the particle ID in the central detector. Fortunately here we have only 3 different layers — MDC, PS, SE. That is why it is not so important to have such a procedure for CD — separation can be easily done by hand. Nevertheless a NN was worked out for this case, too. As before there are 3 inputs, 325 neurons in the hidden layer and 4 outputs. The result can be seen on *Fig. 3—8* displaying data from the run mar05.
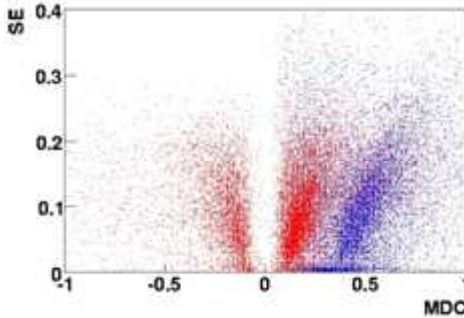

Fig. 3—8 Momentum from MDC vs dE in SE. Different colors are different particle types according to NN: blue are protons, red are pions.

Pions and protons are separated reasonably well. But one can also see that this should not be a problem for separation by hand.

3.2.3.3 Neutral particles in Forward Detector.

In the experiments at WASA we can have two kinds of neutral particles[a] — photons and neutrons. The probability to measure neutrons can roughly be estimated as 1% per centimeter of plastic material. The probability to measure photons in the *FD* was estimated by [29] as 30-50%, depending on energies and selection conditions. So both neutrons and photons have a probability of about 30% to interact with the FD and being

---

[a] Neutrals are particles without hits in thin scintillators Chapter3.2.3.

selected as neutrals. On the one hand this is a rather small number, on the other hand one can think on how to separate such neutrals between each other.

Since photons create electromagnetic showers in the FD, whereas neutrons produce proton recoils, it should be possible to separate them by analyzing the *dE* plots. It was also done by NN, but was not tested so far, in contrast to the two previous cases (Charged FD and Charged CD).

3.2.3.4 Neutral particles in Central Detector.

The dominant part of neutral particles in the CD is photons. Only a small part of neutrons can reach the CD at such large angles (>20°). And only a tiny fraction of them give a signal. It is not possible to distinguish them from photons by *dE* analysis. There was a successful attempt by M.Jacewicz to build a NN for such a type of separation based on cluster size/shape, but I am not aware of any applications, since reactions with neutrons in the CD are not of current interest of WASA collaboration.

3.2.4 Angle correction for forward tracks

The angle of forward going particles is measured far from the vertex. Since part of the track lies in the magnetic field of the solenoid, one must correct for this effect.

In a uniform magnetic field charged particles travel along helices. For forward going particles part of the track, which lies in the magnetic field, will be a helix and another part will be a straight line. Let us assume that inside the solenoid the magnetic field is constant and uniform and outside it is exactly 0, *Fig. 3—9*.
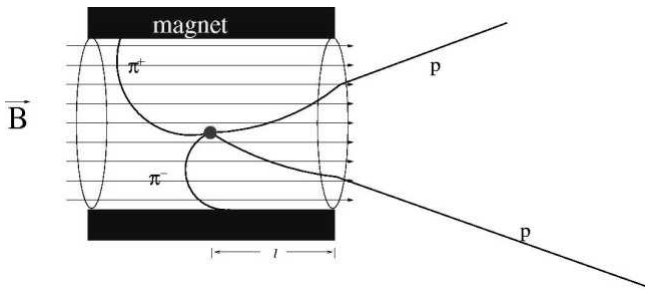
Fig. 3—9 Behavior of charged particles in the magnetic field. Two-pion production in pp collisions. Positively and negatively charged particles turn in different directions

Under such assumptions one can easily derive the formula[a]:

$$\phi' = \frac{l \cdot 0.3 \cdot z \cdot B}{P \cdot \cos\theta}$$

where ϕ' is the correction angle for the azimuthal angle in radians, z the charge of the particle in units of electron charge, B the magnetic field in Tesla, P the momentum of the

---

[a] For full derivation see *Appendix A*

particle in GeV, Θ the polar angle and l the distance in the field, *see Fig. 3—9*, measured in meters. One can make a cross-check of this formula — if the magnetic field is zero, then the correction angle is zero, too. Finally the validity of this formula has been verified by analyzing the reaction $pp \rightarrow d\pi^+$ at $T_p = 400$ MeV .

3.2.5 Angle correction for Central tracks

Usually the angular correction for charged tracks in CD is not needed, because MDC reconstructs angles at the vertex. However some times we can have a magnetic field together with the MDC being switched off. For such cases one may need a correction formula. Since for particles in CD the full track lies in the magnetic field, the formula will be slightly different.

$$\phi' = \pi - 2 \cdot \text{acos}\left(\frac{r \cdot 0.3 \cdot z \cdot B}{2 \cdot P \cdot \sin\theta}\right)$$

where r is the inner radius of the magnet in meters; all other quantities are the same as above.

3.2.6 $E_{dep} \rightarrow E_{kin}$ for forward going deuterons

There are corrections, which can not be done before the particle identification. Since we make the particle ID outside the *W4P* program, all related corrections have to be done outside, too. One of them is $E_{dep} \rightarrow E_{kin}$, i.e., the reconstruction of the kinetic energy of a particle from the energy deposited in the detector, E_{dep} : due to quenching effects and dead, i.e., passive detector material, such corrections are different for different particles. Initially all particles are assumed to be protons, the appropriate correction is done already in *W4P* and stored in *NTF*. But for deuterons it needs to be redone[a].

It turned out to be useful to parameterize particles stopped in different planes separately, in order to decrease the errors. One of the possible parameterizations is

$$E_{kin} = [1 + (e^{(A1+A2*E_{dep})} + e^{(A3+A4*E_{dep})}) + \Theta \cdot (e^{(A5+A6*E_{dep})} + e^{(A7+A8*E_{dep})})] \cdot E_{dep}$$
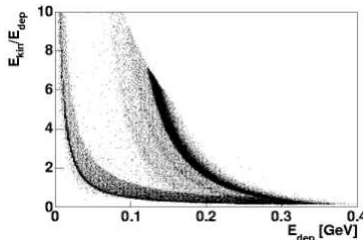

Fig. 3—10 E_{kin} / E_{dep} vs. E_{dep} for deuterons. The Lower "banana" displays stopping particles, the upper ones are punch-throughs. The plot shows MC events for one particular angular bin.

[a] For pions quenching corrections are tiny.

where E_{dep} denotes the deposited energy in GeV and Θ is the polar angle in radians; 1—4 are calibration coefficients, different for different stopping layers of FRH. The following table gives the appropriate parameters for deuterons:

Table 3.2.3.4-1 Calibration constants for deuterons in the FD.

Stopping plane:	1	2	3	4	Punch through
A1	2.0323	0.4685	0.7688	9.1301	11.8193
A2	-67.219	-15.990	-14.520	-45.440	-78.5049
A3	0.2199	-1.5828	-1.9609	-0.7163	3.5886
A4	-9.1901	-0.5497	0.2067	-2.9332	-15.445
A5	1.3763	27.149	30.597	7.1107	1.96028
A6	-120.31	-214.32	-156.12	-36.207	-12.2744
A7	-0.9260	-1.4222	-2.6355	-17.243	
A8	-18.534	-12.996	-7.0474	37.461	

The constants have been obtained by MC simulations and verified by data for the $pp \to d\pi^+$ reaction at $T_p = 640\,\text{MeV}$. Since this is a binary reaction, we can reconstruct the energy of a deuteron by its known angle and compare it with our energy calculation. It agrees reasonably well — $\frac{E_{reconst} - E_{calc}}{E_{calc}} \approx 0.0017$ — about 4%FWHM for stopping deuterons.

3.2.7 $E_{dep} \to E_{kin}$ for forward going ^{3}He particles

The effects of dead material and quenching are very strong for helium, since it is a heavy double-charged particle. It is also a question how well MC can describe such effects. Therefore it was decided to extract such parameters from real data. For our run period we have a very nice reference reaction, namely $pd \to {}^3\text{He}\pi^0$. It covers even a larger dynamical range than two-pion production, therefore it is well suited for our purposes. But before one should correct for ϕ nonuniformities: since the calibration constants achieved are based on protons, high order nonuniformity parameters can be slightly wrong. On Fig. 3—11 on the left side, we see that the maximum energy deposition is different for different elements, which should not be true in reality.
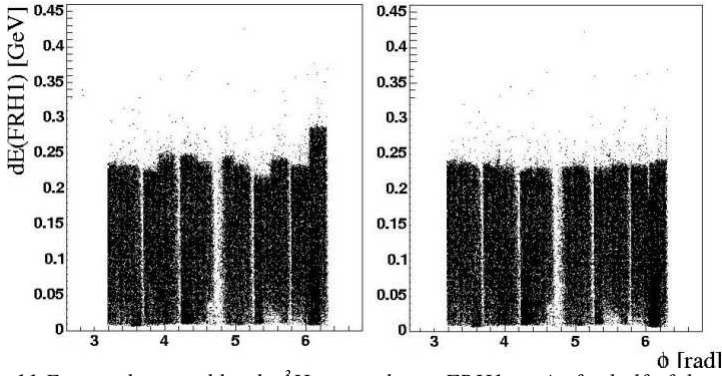
Fig. 3—11 Energy deposited by the ^{3}He particles in FRH1 v.s ϕ for half of the detector. Before (left) and after (right) corrections. (for more information see text)

Broad bands in Fig. 3—11 correspond to elements in the *FWC,* each of these elements in ϕ contains two elements of the FRH1, clearly seen on the left. We can correct for a mismatch by a linear function: $E'_{dep} = k \cdot E_{dep}$ (see *Fig. 3—11* (right)).

If we make all of our elements respond in a similar way, we can make the $E_{dep} \rightarrow E_{kin}$ corrections. As described before we can do it based on single pion production.
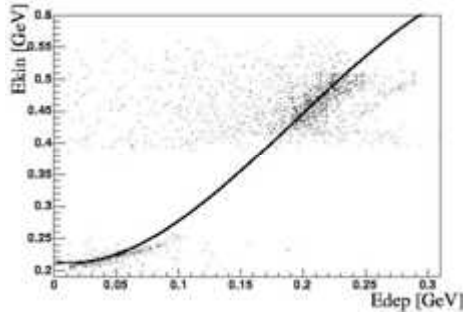

Fig. 3—12 E_{kin} vs E_{dep} plot for $pd \rightarrow {}^3He\pi^0$ events together with the fit curve.

For this purpose the function

$$E_{kin} = 0.214 - 0.270 \cdot E_{FRH1} + 11 \cdot E_{FRH1}^2 - 19.07 \cdot E_{FRH1}^3 \text{ , [GeV]}$$

is used for particles stopped in the first plane and

$$E_{kin} = 0.214 - 0.270 \cdot E_{FRH1} + 11 \cdot E_{FRH1}^2 - 19.07 \cdot E_{FRH1}^3 + E_{FRH2} \text{ , [GeV]}$$ for particles stopped in the second plane. At our energy ($T_p = 895 \text{ MeV}$) helium particles do not penetrate further.

To check the result of such a correction we look on the missing mass of ^{3}He in the $pd \rightarrow {}^3He\pi^0$, *Fig. 3—13*, where the spectra before and after correction are compared. Also the $\gamma\gamma$ invariant mass distribution is shown to compare the resolution.
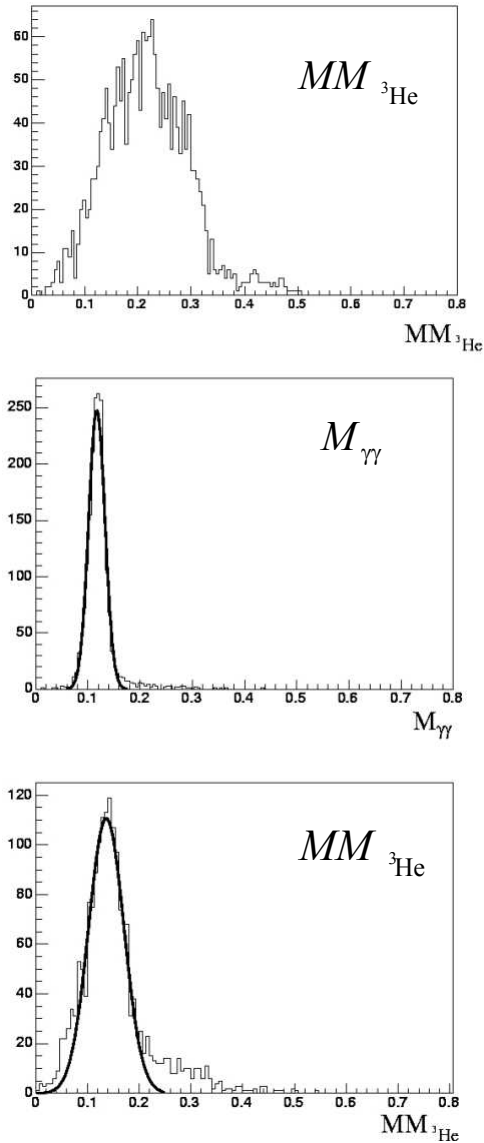
Fig. 3—13 $MM_{^3He}$ before corrections(top). $MM_{^3He}$ after correction (bottom). $M_{\gamma\gamma}$ (middle)

38

3.2.8 $E_{dep} \to E_{kin}$ for charged pions in the CD

   In principle one should determine the energy of charged particles in the central detector by using the momentum achieved from the MDC. But sometimes it may be necessary to know the energy of pions from the SE (if the MDC is not working, or there is no signal from the MDC). Then one has to apply corrections due to the substantial amount of dead material in front of the calorimeter (magnet, PS, MDC). Again one can get such corrections from MC simulations. In the case of positively charged pions one will get the following picture *Fig. 3—14*.

   One can see that for pions with energy more than 70 MeV such corrections are small. The decrease of the correction spectra on the left and right sides tells us that the angular size of the magnet is smaller than the angular size of the central detector. If pions do not have to pass through the magnet material, than such corrections are negligible at all energies.
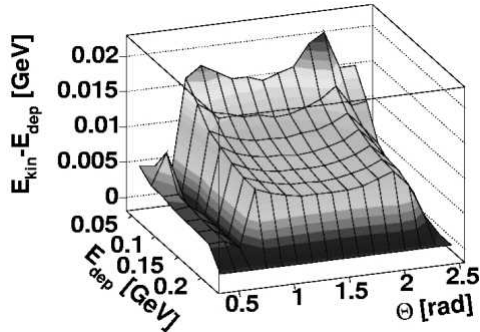

Fig. 3—14 Corrections for dead material for charged pions in the central detector.

   The quenching effects for pions are also tiny, so one can also neglect them.

3.3 Automatic calibration procedure with the neural net

Unfortunately this part was done much later than the whole analysis, otherwise it would have helped a lot. Nevertheless it makes sense to mention this work from both a methodological and an experimental point of view. It shows the achievable experimental resolution and the further way of simplifying the analysis.

The standard calibration procedure applied in this thesis is well described in [30]. It usually proceeds in the following way. Some *"guru"* sits in front of the computer and looks onto the *dE-E* plot for one special element. Then he/she selects some areas in that plot, the computer extracts the coordinates of these areas and makes a fit with *"guru predefined function"*. And this procedure is repeated for all 216 elements of the forward detector. There is an advantage of that procedure is that the "guru" can make the calibration extremely well, due to his or her high experience. But there are certain disadvantages: "gurus" are rare and during the experimental run they have a lot of much more important duties. The calibration is "guru" mood dependent — depending on the mood the "guru" can select areas more or less precisely. All elements will then be calibrated slightly differently, because a person can not do this 100% precise, and it is too many elements to be tied. Since all "gurus" are busy with other things, the calibration constants are updated once in half a year which is much too rare for extreme precision. Also the "guru" may not be interested in that run period paying less attention to calibration or it may be another "guru". But this actually was a minor problem. There is a basic problem, which prevents such a type of calibration procedure to reach ultimately high precision:

- Calibration is done on a statistical basis. Within some errors fit can draw a curve everywhere, but there is only one optimal place.
- All elements in φ use the same fitting function, but the properties of elements could be very different, requiring thus different curves.
- The properties of elements can change with time — hence the fitting function also should be changed and the calibration constants will be different; there will be several types of calibration constants, not compatible for different run periods.

Since this calibration quality is variable, all precise algorithms relying on it will fail or at least one would need to spend some time to verify them in a new calibration reality. As an example, one in principle needs to check "banana" boundaries in each run period, and not make it once and forever.

That is why there was a great desire to make a precise "guru"-independent calibration procedure providing stable repeatable results for each run period. The greatest wish was to make it on a event-by-event basis and take into account all disadvantages of the "guru's" method mentioned above.

As a matter of fact such a procedure was written. It gives extremely nice results — much better than the present calibration, which is extremely important for the FHD, where the process of aging goes so far that it is barely usable.

So in this chapter such an automatic calibration procedure based on a neural net will be described.

3.3.1 Selection of the data for the calibration.

The selection of appropriate data is the first step in all calibration procedures. The best thing would be to use some software package, where one has access both to event track information and to hit information. Unfortunately it is not possible right now. So the CWlib package was chosen, because of its transparency for an external user. One can easily access all hit information in it. Also, in this step simple tracking is done, just by overlap of the elements. And the polar angle is calculated by overlap of FHD1-FHD2 elements. That is why all "tracks" are required to have signals in all FHD planes and at least in FRH1. For simplicity only events with one charged particle in the FD were selected. The extracted hits information (ADC) and angle of "tracks" are written into root TTree (modern type of hbook ntuples). Starting from this step everybody can use this information, since it is standard.

The next step is to select desired events from the whole amount of one-track events. And this is the most difficult part in the calibration procedure. Since the elements are not yet calibrated, you do not see bananas[a] to select areas — to see "bananas" you need some calibration constants — but if you have calibration constants, you do not need to calibrate. In addition the gain factor can be very different, so one does not know ad hoc what the range of ADC values will be.

This problem is solved in several steps: The FRH has much smaller nonuniformities and much less nonlinearities than the FHD. So it is a good idea to calibrate the FRH first.

Step one: How to get nonuniformities for all elements of the FRH in a man independent way.

Solution: First one selects punch-through particles (particles which pass through the whole forward detector). They are supposed to deposit $2\,\text{MeV}$ per g/cm^2 — corresponding to minimum ionization. And if all of our elements would be uniform, then the energy deposition of such type of particles should be roughly constant[b] for all angles, but it is not, *Fig. 3—15*. Since it is just a single band, it can be easily fitted by computer and all elements in all 4 FRH planes can be corrected accordingly.
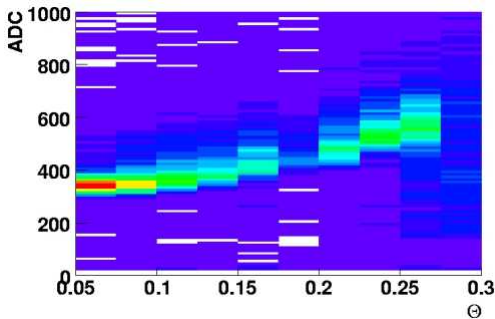

Fig. 3—15 Nonuniformity. ADC vs. Theta for one element of FRH1 for minimum ionizing particles.

---

[a] ΔE-E hyperbolas, called "bananas".
[b] The difference due to different thickness of material at different flight paths is below 3% compared to nonuniformities which can reach 2500%

One can see in *Fig. 3—16* that after such corrections one can see the particle bands much better than before. After such a correction has been carried out we can start to think about the selection of some point for calibration.
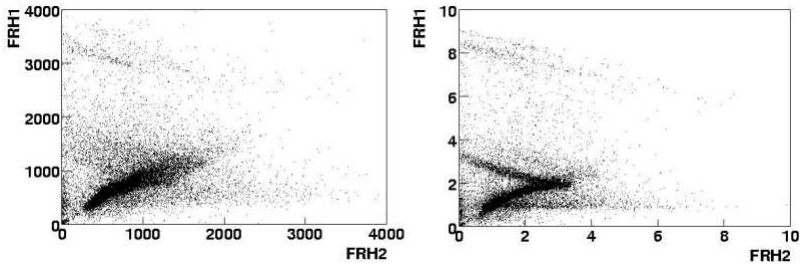

Fig. 3—16 d E -dE plot, FRH1 vs. FRH2 for one element. Before nonuniformity corrections (left), and after step one(right)

Step two: which events can we use for calibration? It is required that these points (regions occupied by events at *dE-E* plot) should be easy to find by computer and be gain independent.

Solution: On *Fig. 3—17* one can see several points, which can be used for calibration and can be found by the computer in a gain independent way.
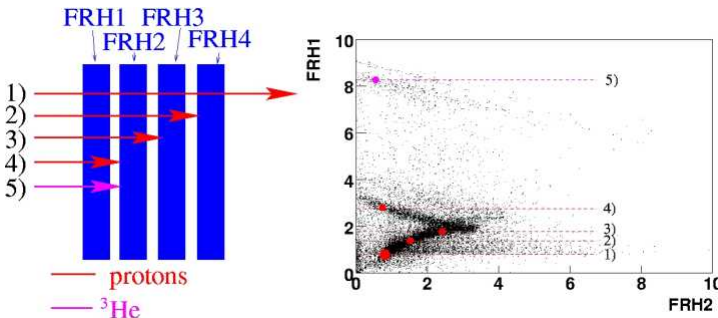

Fig. 3—17 Gain independent points for FRH1 calibration. 1) minimum ionizing; 2) stopped in FRH4 and depositing in FRH4 the same amount as minimum ionizing (MI); 3) stopped in FRH3 and deposited in FRH3 the same amount as MI; 4) stopped in FRH2 and deposited in FRH2 the same amount as MI 5) Helium stopped in FRH2 and deposited in FRH2 the same amount as MI., see sketch at the left.

So we have now 5 solid points, which we can use for *FRH1* calibration. Unfortunately all ^{3}He particles stop either in the first or in the second plane, that is why the large distance between the 4th and 5th calibration points can not be covered. As a matter of fact there are too many points at small E_{dep}, so we can skip point number 2.

Step three: How to prepare a training sample?

Solution: The quality of the training sample is extremely important for neural nets. The question if you solve your task with the neural net or not, depends on the quality of the training sample at least to 70%. In our case we can not just put calibration points *Fig. 3—*

17 into the neural net. We have to inform the program, how our data behave between these points. To do so, we prepare a fit. For each of the points we know the value for ADC, Θ, and expected deposited energy (from MC). So we produce a fit with the function:

$$E_{dep} = f_1(ADC) \cdot f_2(\Theta),$$

where f_1 and f_2 are third order polynomial functions.

If we were satisfied with a "guru-like" calibration, then we could stop at this stage. But we want to do better. That is why we take a E_{dep} fitted function and simulate events over the whole possible range of ADC and Θ. And add this simulated example to the real selected points in proportion 1:1 — one simulated event per one real. This helps to avoid misunderstandings between programmer and neural net.

Step four: What topology to choose for such a neural net?

Solution: We have several constraints on the topology of such a neural net. For sure we know how many inputs we want (2 — ADC, Θ) and how many outputs (1 — E_{dep}), but how many hidden layers should we take, or how many neurons should be in such layers? Since we want to have the same topology for all our detector elements of all our detectors, we need to decide, what topology would be enough to calibrate the most complicated (in calibration) detector (FHD). By trial and error it was found that a topology with 3 hidden layers, *Fig. 3—18*, and 8:16:4 neurons works remarkably well.

Step five: Training.

Solution. It was found that it is enough to make only 500 training epochs to reach good results, which is very small. The training sample is about 10000 events per element (half of them are simulated), so it takes 15-20 minutes per element on a usual computer — very little compared to hundred thousands of events in training examples for the particle ID and thousand training epochs there (few weeks of training). The calibration is fast and easy and can be easily done in one night.
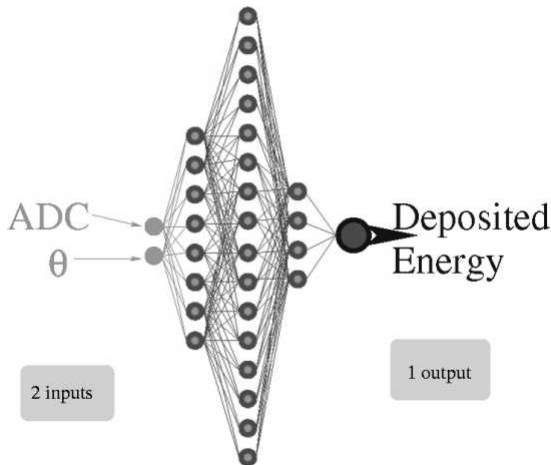

Fig. 3—18 Topology of the Neural Net used for calibration.

Step 6: Calibration of the FHD.

Solution. The calibration of the FHD essentially is the same as of the FRH1, but much more complicated even for straight elements: the nonuniformities can reach a factor of 20 (if one would plot *Fig. 3—15* for the FHD then for some elements the right side of the band can be 20 times higher than the left one.). The PMTs turn out to be highly nonlinear and the aging effect is enormous (after the transportation of the WASA detector to COSY, one of the elements was opened up — it was brown and full of cracks — far from the situation a usual plastic scintillator should look like.). All of these problems make the calibration of the FHD much more complicated, because every small error if magnified by nonuniformity can become huge. In fact nonuniformity parameters[a] vary from 1 to 30 for different elements, in addition the functions of such nonuniform responses are different. The microcracks together with nonlinearities of PMT's make nonuniformities energy dependent. So one can not use the trick like **Step one** for FRH1.

The main task for the nonuniformities of FHD is to separate deuteron and proton "bananas", that is why we take point number 5 from *Fig. 3—17* to extract nonuniformities, which is roughly in the same energy region.

Step seven — Get nonuniformity parameters for FHD like in **Step one**, but use ^{3}He .

Step eight: Select points of calibration.

Solution: Since the functional behavior of the FHD is much more complicated we need more points for the calibration —7, *Fig. 3—19*. Since the FRH1 is already calibrated at this stage, selecting the range of points becomes easier here, which compensates the difficulty of separating the different bananas along the FHD axis.

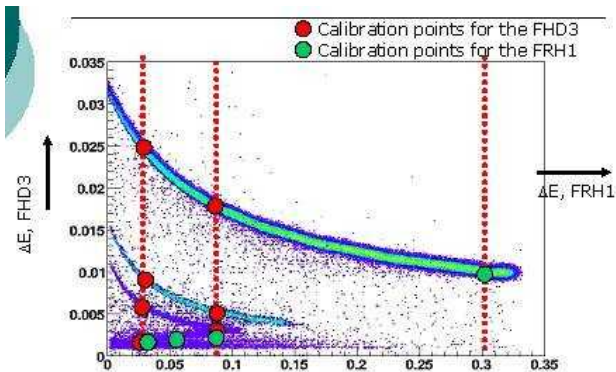All later steps for all layers of FHD are exactly the same as for FRH1.

Fig. 3—19 MC plot FHD3 vs. FRH1 with calibration points. From top to bottom: ^{3}He , deuteron and proton bands.

Step last: Results.

The result of such a complicated procedure is shown in Fig. 3—20 which is similar to Fig. 3—19, but for real data.

---

[a] Ratio between light output from a point close to photomultiplier to the farthest point of the element for the same source (in our case for minimum ionizing particles)
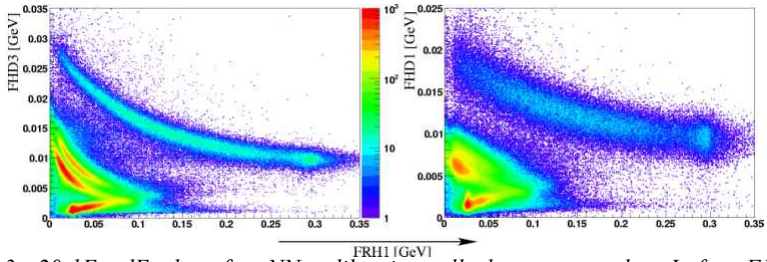
Fig. 3—20 *dE—dE plot after NN calibration, all elements together. Left — FHD3 (straight element); Right — FHD1 (curved element)*

One can see that the real data look very similar to MC. And even for curved elements (FRH1, FRH2) one can see (or at least imagine) different "bananas". To plot all elements together in one plot is to show the advantages of the NN calibration: since for conventional fitting the calibration of the position of "bananas" is not fixed within error, "bananas" from different elements have slightly different positions, at best distributed by Gaussians around the true value. Therefore if one plots all elements together, ambiguities smear the "good" calibration of each single element.

In contrast, the "bananas position" after the NN is really fixed. In reality, our present non NN calibration for FHD3 looks more like NN calibration of FHD1 (*Fig. 4—3* vs. *Fig. 3—20*), much worse compared to a NN calibration.

3.4 Outlook

From the previous chapters one can see that usage of Neural Nets can simplify the analysis substantially. Since the WASA detector is presently getting updated, after its move to COSY, we may consider what we can improve by use of neural nets. There is one thing worth mentioning: Neural nets can be not only software implemented, but also in hardware. Actually hardware neural nets are much faster, so fast that they can be used at trigger level. So let us imagine the future system *Fig. 3—21*.

If we look at *Fig. 3—21* then one can see several components. The first one (from the left) relates to the FHD — the system which can determine Θ and ϕ angles of the tracks, just by overlap of elements. For this one does not really need any complicated calculation, but only element numbers and some mapping.

Then at the next step, by knowing Θ angle and ADC we can calculate the deposited energy for each element as described in *Chapter 3.3*. To make this possible we should connect a small neural net to each element. After this stage we would know already quite a lot — angles of each track and deposited energies in each plane. But we can go further — as described in *Chapter 3.2.3* this is the complete information we need to make a particle ID.

So if we were to construct a hardware NN similar to *Fig. 3—6*, then already on trigger level we would know quite a lot. We can go even further — knowing the deposited energies and particle ID we can calculate the kinetic energy for each track. And if we came to this stage then we would know everything about our reaction, i.e., the four-momentum vector for each particle.
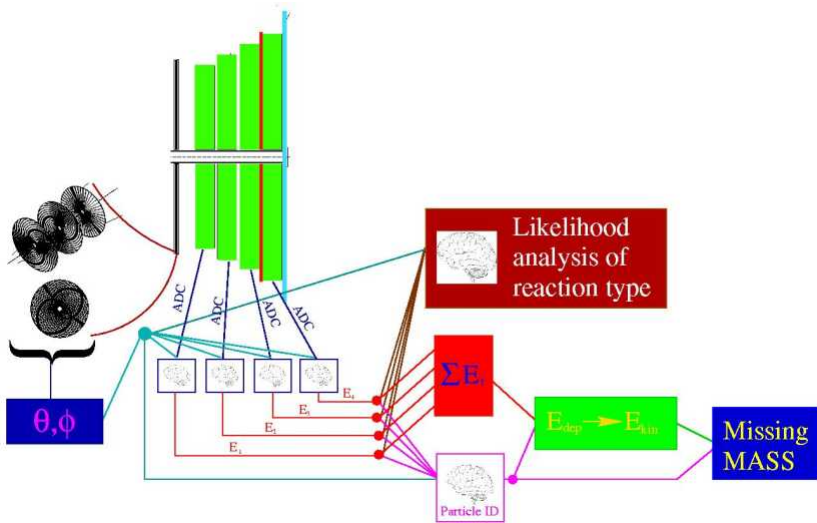
Fig. 3—21 Sketch view of an ideal system based on neural nets.

Then there are two possibilities:

1. We can make a missing mass trigger, e.g. for η tagging. In the $pp \rightarrow pp\eta$ reaction we usually have two protons in the FD, and usually all the rest (the decay products of η) in the CD. If we construct a trigger condition — two charged particles going forward — then we have a high background from multi-pion production, so we need either to make a constraint on decay channels — which is unfavorable because we would have a trigger dependent efficiency in the decay branchings — or we apply a missing mass condition on two protons suppressing then multi-pion production without suppressing η's.

2. Another possibility is to make a likelihood analysis based on neural nets as e.g. Fermilab does for the top quark reconstruction [31]. Or as it is done in MultiLayerPerceptron ROOT test example for Higgs selections [32]. For each given beam energy one can build a network which would provide the probability for a particular reaction for each single event. E.g. for each event one can get something like that: two-pion production with probability 1%, three-pion production with probability 10% and eta production with probability 89%.

One can in principle combine the first and the second case. Actually the second case is much more profound, but difficult. But since experiments are always performed at very few different energies, it should not be a problem to build a neural network for extracting reactions.

Actually even if it would not be realized at the trigger level, the NN can be realized in the offline analysis and can simplify a lot to make it much faster.

4   Analysis

In this chapter all steps will be described that were done to select, reconstruct, fit, and correct $pd \rightarrow {}^3\text{He}X$ reactions. For the analysis the March2005 data sample was chosen because of predictable trigger efficiency, large statistics and workable pellet and beam conditions. The analysis was done based on run numbers 42,43,44,45,46,52,53 — 24 million events in total, which leads to 116268 ${}^3\text{He}X$ events. The trigger condition was favorable for performing an unbiased analysis with respect to charged and uncharged pion channels. It requires one hit in the FWC, one hit in FHD3 (overlapping with FWC) and one hit in the FRH1. In addition there was a high threshold on the FWC, in order to suppress other (proton or deuteron) events. Previous pd runs had additional threshold conditions for the FHD3 and a veto for the FRH2. Both these conditions appeared to be bad. The veto condition cuts some part of data (it implies that ${}^3\text{He}$ should be below 0.55 GeV); the threshold FHD3 condition suffers from the high nonuniformities in FHD. Hence the selected run period had optimal trigger conditions for ${}^3\text{He}$ physics.

All systems were working reasonably well with a beam cycle of 180 s, a flat top intensity of 50-150 s, an average beam current 1.5-2.1 mA and a solenoid magnetic field of 1 T.

4.1 Kinematics of pd $\rightarrow$ ^{3}HeX reactions

Before starting the description of the analysis, even before starting measurements, one should understand how well one can measure these reactions. Since these reactions are based on a reliable ${}^3\text{He}$ information, we are first of all interested in the kinematics of ${}^3\text{He}$ in the reactions of interest here, i.e. $pd \rightarrow {}^3\text{He}\pi^0$, ${}^3\text{He}\pi\pi$, ${}^3\text{He}\pi\pi\pi$ and ${}^3\text{He}\eta$, as shown in *Fig. 4—1* for the relation between ${}^3\text{He}$ lab energy $E_{{}^3\text{He}}$ and lab angle $\Theta_{{}^3\text{He}}$.
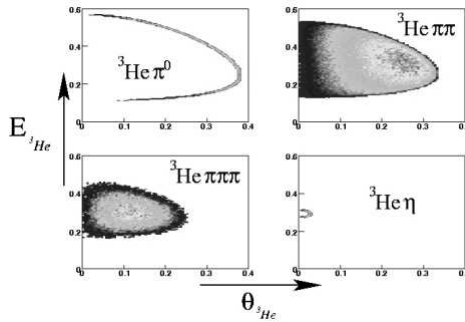

Fig. 4—1 Kinematics of ^{3}He lab energy $E_{{}^3\text{He}}$ versus lab angle $\Theta_{{}^3\text{He}}$ for the most probable ^{3}He reactions at $T_p = 0.895\,\text{GeV}$: ^{3}Heπ^0 (top left), ^{3}He$\pi\pi$ (top right), ^{3}He$\pi\pi\pi$ (bottom left), ^{3}Heη (bottom right)

Note that for 3-body reactions this relation gives an allowed region rather than a line as in the case of two-body reactions. The density of points in the continuum of the

allowed region depends on the dynamics of the reaction. For *Fig. 4—1* pure phase space has been assumed. The $E - \Theta$ information from ^{3}He is sufficient for obtaining mass and CMS angle of the system X in $pd \rightarrow {}^3$HeX reactions.

Looking at *Fig. 4—2*, which compares these kinematics with the FD acceptance, one can see that for ^{3}Heπ^0 we cover only a small part of the full phase space, for ^{3}He$\pi\pi$ we cover about 80% and for ^{3}He$\pi\pi\pi$ we cover nearly 100%. Actually the situation is even better. According to [6] the ABC effect should be forward-backward symmetric in the CMS. In this case it would be sufficient to measure only $\Theta_{^3\text{He}}^{CMS} < \pi / 2$, i.e., a region, which we cover nearly completely. This allows making model independent efficiency and acceptance corrections.
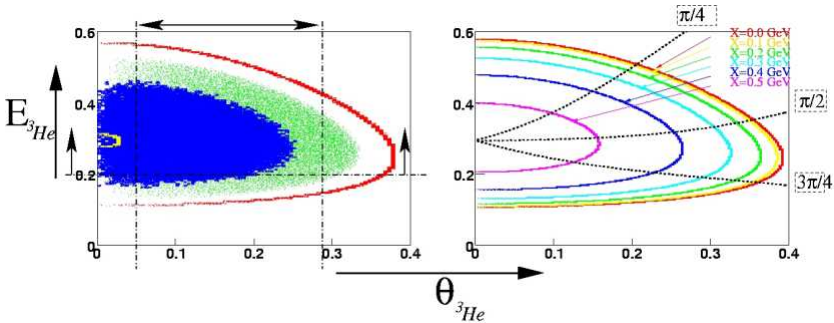

Fig. 4—2 The left plot is the overlap of the 4 plots from Fig. 4—1 (here red is single π production, green - $\pi\pi$, blue - $\pi\pi\pi$ and yellow is η production). Dashed-dotted lines show the acceptance of the FD. Right: kinematics decomposition for ^{3}He lab energy and lab angle (with CMS $\pi / 4$, $\pi / 2$ and $3\pi / 4$ angles of ^{3}He indicated by dotted lines) as well as M_X. Solid lines denote $M_X = const$ in rainbow order — 0.0 Gev, 0.1GeV, 0.2GeV, 0.3GeV, 0.4GeV, 0.5 GeV

4.2 Selection of the $pd \rightarrow {}^3$HeX reactions

As mentioned in *Chapter3.2.3* the analysis of these reactions was done prior to the recent development of the neural net. But due to their double charge ^{3}He particles deposit a much larger energy per unit of length than single-charged particles do. And most of ^{3}He particles stop in FRH1. So we have only one appropriate *dE-E* plot, namely *FHD3-FRH1*.

As one can see from *Fig. 4—3* the ^{3}He band is nicely separated from those for protons and deuterons. We also can see that the additional condition of accompanying pions cleans the spectrum substantially. Actually it is putting the cart before the horse, since we did not describe yet how to select pions, but it is good to see those plots next to each other for comparison. Pion selection will be described later.

Since the ^{3}He "banana" is well separated and there is practically no admixture from other bands, we can apply the conventional "banana" cut

$E_{FHD3} > \exp(-4.5 - 19.61 \cdot E_{FRH1}) + \exp(-5.0 - 0.76 \cdot E_{FRH1})$ [a]   without   worrying about additional background.
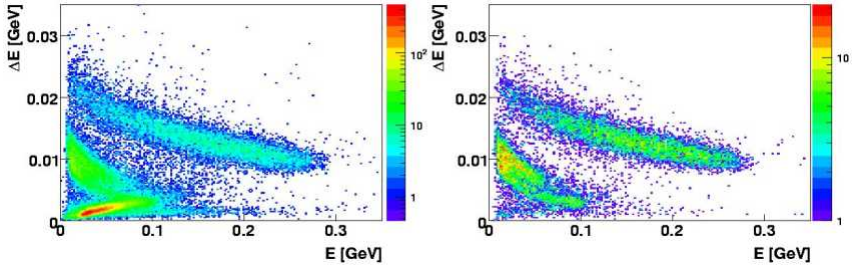

Fig. 4—3 Left: dE-E plot FHD3 vs. FRH1 (FRH1+FRH2) — both axis denote deposited energies. Right: the same plot but with requirements $\pi^0\pi^0$ or $\pi^+\pi^-$ in the CD. The z-axis is logarithmic for both plots. One should also take into account that we take only ^{3}He with deposited energy more than 0.1 GeV due to our $\Theta_{^3\text{He}}^{CMS} < \pi/2$ cut, Section4.1

After selection of ^{3}He we can make all energy corrections described in *Chapter3.2.7* and immediately make a cut $E_{^3\text{He}}^{kin} > 0.29 + 0.35 \cdot \Theta_{^3\text{He}}^2$ [b] which corresponds to the $\Theta_{^3\text{He}}^{CMS} < \pi/2$ cut. The situation at this stage is depicted in *Fig. 4—4*.
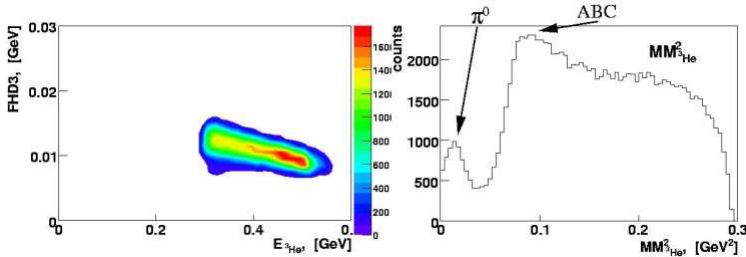

Fig. 4—4 Left: dE-E plot after ^{3}He selection and application of corrections and cuts. Right: $MM_{^3\text{He}}^2$ for the events shown in the left figure. Since the acceptance is close to 100% and the efficiency is roughly constant., the spectrum is close to a final one. One can see well separated regions of single and double pion production

Another important figure, which already can provide some insight into the dynamics of the $pd \rightarrow {}^3\text{He}X$ reactions, is the $E - \Theta$ plot in *Fig. 4—5*, which is similar to *Fig. 4—2*, but now for real data.

---

[a] Energies are in GeV
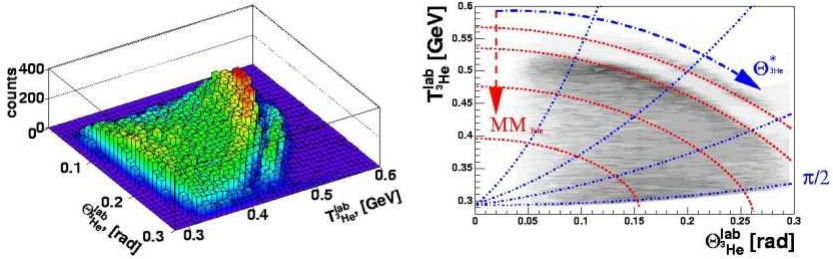[b] Energy is in GeV, angle is in radian

Fig. 4—5 3D and contour plots of lab angle Θ_{3He}^{lab} versus lab energy T_{3He}^{lab} for particles measured in FD. The dash-dotted lines are for $\Theta_{3He}^{lab} = 22.5°, 45°, 67.5°, 90°$. The dashed lines indicate the contours of missing masses $MM_{3He} = 0.135, 0.27, 0.4, 0.5$ GeV (from Ref. [43]).

By comparing with Fig. 4—1, Fig. 4—2 and Fig. 4—4 one can clearly see the single pion production to be well separated from the two-pion production, which shows an impressive enhancement close to $\pi\pi$ threshold — the ABC effect.

Already at this very early stage of analysis we can plot figures, see *Fig. 4—6*, similar to (*Fig. 1—1),* from the literature [2], [3],[6].

One can see that at this stage our data look compatible with previous measurements. Unfortunately nearly all previous experiments had to stop at this stage of analysis, lacking further experimental information. However, we can go on and select explicitly $\pi^0\pi^0$, $\pi^+\pi^-$ and π^0 channels and study all exclusive spectra.
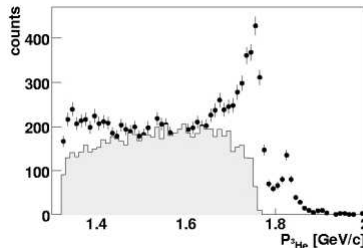

Fig. 4—6 ^{3}He momentum spectrum for the angular bin $7° < \Theta_{3He}^{lab} < 8°$ (not corrected for detector efficiency). The data points represent the inclusively measured spectrum for comparison with Saclay data [6]. The shaded area normalized to touch the data as in [6] shows phase space passed through the simulated detector (GEANT), and reconstructed afterwards

4.2.1 Single and double π^0 selection.

Single and double π^0 channels are selected in roughly the same way. Actually the requirement of the presence of ^{3}He in the FD removes a lot of background. Since

π^0 decays into two photons we need to ask for two neutral particles in the CD, (Chapter 3.2.3.4) in addition to the requirement of ^{3}He particles in the FD in order to select the $pd \rightarrow ^3\mathrm{He}\pi^0$ reaction. In reality we can have more than two photons, because we have a rather high photon background. Fortunately this background consists mostly of photons with little enegry. So usually we require not exactly two photons, but two or more photons.

In order to clean up our spectrum even more we can set the additional condition: $(M_{\gamma\gamma}/\mathrm{GeV} - 0.135)^2 + (MM_{^3\mathrm{He}}/\mathrm{GeV} - 0.135)^2 < 0.06^2$ meaning that $M_{\gamma\gamma}$ and $MM_{^3\mathrm{He}}$ should be roughly the same and should not deviate too much from the expected value. After this selection we arrive at *Fig. 4—7*.
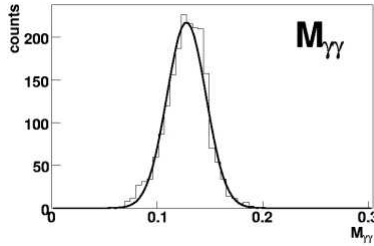

Fig. 4—7 Invariant mass of two photons to select reaction $pd \rightarrow ^3\mathrm{He}\pi^0$, fitted with a Gaussian (FWHM $\approx$ 20MeV).

The selection of $\pi^0\pi^0$ events proceeds in the same way. First we require "good ^{3}He" particles and thereafter four and more photons in the CD. In addition one needs to combine 4 gammas into two π^0 correctly. To do this we use the circular requirement: $(M_{\gamma_1\gamma_2}/GeV - 0.135)^2 + (M_{\gamma_3\gamma_4}/GeV - 0.135)^2 = \min$ for the proper combination. All in all there are three possible combinations. By calculating the expression above we choose the most appropriate one. In addition we require that for the best combination we should have $(M_{\gamma_1\gamma_2}/GeV - 0.135)^2 + (M_{\gamma_3\gamma_4}/GeV - 0.135)^2 < 0.05^2$ in order to select $\pi^0\pi^0$ events cleanly, *see Fig. 4—8*.
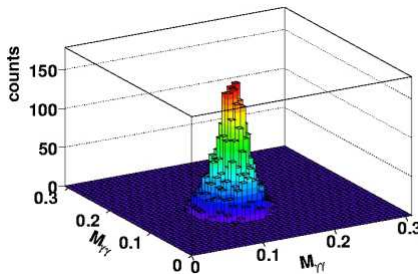

Fig. 4—8 $M_{\gamma_1\gamma_2}$ vs. $M_{\gamma_3\gamma_4}$ for the best combinations of photons, according to description above. Tails are cut away by a circular cut.

4.2.2 $\pi^+\pi^-$ selection.

The selection of charged particles in the CD is much more difficult than that for the neutrals. For neutrals the condition is simple — cluster in the SE. For charged particles there could be several different types of tracks: PS—SE; MDC—PS; MDC—PS—SE. We can not require for all tracks to have a signal in all three layers (MDC—PS—SE), because on the one hand, the efficiency of the MDC in the forward part of CD is small [22] due to its construction. And on the other hand, the particles, which fly to large angles, usually have a rather small energy — not enough to reach the SE. So if we would impose for all charge tracks a three-layer condition, then we would have a complicated angular-energy dependent efficiency. And it would not be easily possible to correct data in a model independent way. Even more importantly, the average single track efficiency of the MDC is about 75-80%. Asking for two charged tracks with a MDC signal reduces the event sample by a factor of two. That is why it was chosen to use any charged tracks among the three possibilities described above, but at least one track should have a signal in MDC to deduce the charge decomposition of pions. This gives an overall efficiency of about 94% ($1 - 0.25 \cdot 0.25 = 0.9375$ — only events without MDC information for both tracks are rejected). Fortunately we do not need a particle identification for such a case, because if we have ^{3}He in the forward detector and two charged particles in the central detector, than these could be only pions (actually they also could be electrons from π^0 Dalitz decay, but the cross section for single π^0 production is an order of magnitude smaller than for $\pi^+\pi^-$ production, and the branching $\pi^0 \to \gamma e^+ e^-$ is only 1.2%, which gives a contribution of such admixture at the sub per mill level). For verification, we can look at the *P-E* plot for charged particles after ^{3}He selection shown in (*Fig. 4—9*).

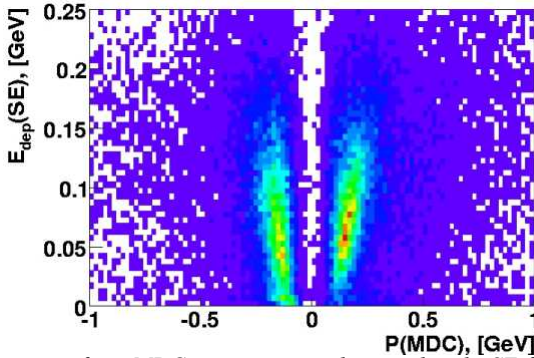*Fig. 4—9 Momentum from MDC versus energy deposited in the SE for charged particles (MDC-PS-SE) after ^{3}He selection in FD. Negative momenta P are for negatively charged particles*

One can compare *Fig. 3—8* with *Fig. 4—9*. It is clear that protons, present in the first picture absolutely disappeared in the latter. One may wonder about the small asymmetry between positively and negatively charged pions in *Fig. 4—9*, but this difference comes from the fact that π^- form pionic atoms when stopping.

4.3 *Kinematical fit* (Kfit)

The kinematical fit procedure is based on the Lagrange multipliers method introduced by Joseph-Louis-Lagrange in his "Théorie des Fonctions Analytiques" (1797). The application of the method for physics purposes can be found in [33]. Details of the algorithm which we use are described in [34]. So why do we need a kinematical fit at all? The reasons are uncertainties: all quantities which we measure (angles, energies) have uncertainties, but yet the derived kinematical quantities should obey energy and momentum conservation. Therefore we can vary a bit all our quantities within errors, to obey these laws, and thereby increase the accuracy of the data. Also background events can be further filtered out this way.

In order to use the kinematical fit, we need to settle the expected errors for each quantity. The absolute error is not that important, but the relations between different errors are. So if we would take real errors and increase them by factor of two — nothing will happen and the results of the kinematical fit would be roughly the same. But if we would increase only one error (for example only the error for the angles of pions), than we can get some weird results.

In our case we used the following errors: $\Delta E_{^3\text{He}} = 15$ MeV (in principle the error should be energy dependent, but in our case we have a small range of ^{3}He energies, that is why the error is roughly constant.); $\Delta E_\gamma / E_\gamma = 7\%$; $\Delta E_{\pi^0} / E_{\pi^0} = 7\%$, but the error can not be less than 10 MeV, if it is less, it is set to 10 MeV; $\Delta E_{\pi^\pm} / E_{\pi^\pm} = 7\%$, but not less than 15 MeV, the reason is described in *Chapter 3.2.8*. The angular errors are as follows: $0.2°$ for forward going particles and $5°$ for particles in CD.

The Kfit routine implemented in the WASA software proceeds in an iterative way and stops, if the conservation laws are fulfilled within 0.5 MeV or if the fit has diverged[a]. As a result of the fit one has corrected values of energies and angles and χ^2. So one needs to make a cut on χ^2. In our case we accept all events with $\chi^2 < 2$ [b], which does not cut away too much: for $pd \to {}^3\text{He}\pi^+\pi^-$ after all cuts but before Kfit we have 5796 events, after KFit and the χ^2 cut still 5532 events remain. For $pd \to {}^3\text{He}\pi^0\pi^0$ we have 8209 events before and 6331 events after Kfit. The stronger suppression in the case of neutral pions comes from larger number of constrain, as described below.

We also use some trick for the case of $pd \to {}^3\text{He}\pi^0\pi^0$: for $pd \to {}^3\text{He}\pi^+\pi^-$ one can make a kinematical fit with four overconstraints. For neutral pions we measure photons, so we have the two additional constraints that the photons must combine to neutral pions. However we did it in a slightly different way. First we fit the reaction

---

[a] If Kfit is diverged that event is dropped out

[b] Here χ^2 determined in a slightly different manner: $\chi^2 = \sum_i \left(\left(a_{out}^i - a_{in}^i \right) / \varepsilon_i \right)^2$, where i is sum over all kinematical variables of all particles, a_{in} is the value of a variable before Kfit a_{out} is the value after KFit, and ε is the error for this variable.

$pd \rightarrow {}^{3}\mathrm{He}\gamma\gamma\gamma\gamma$ with 4 overconstraints, and then combined the gammas into the neutral pions and fit the $pd \rightarrow {}^{3}\mathrm{He}\pi^{0}\pi^{0}$ reaction again.

4.4 Efficiency and acceptance corrections.

Finally data should be efficiency and acceptance corrected. Fortunately in our case these corrections are expected to be small, *see Chapter4.1*. They can be made in several different ways. The most usual one is sketched in *Fig. 4—10*.

In our case the data can be corrected in a model independent way due to the high phase space coverage in our experiment. For convenience we will use pure phase space as a model for corrections[a].

The other way is to use multidimensional corrections: a three-body unpolarized reaction has 4 independent variables. So instead of using one-dimensional histograms, *Fig. 4—10*, we can use a 4-dimensional histogram — each event in this case would be a point in four-dimensional space[b]. So our correction factors in this case would be 4-dimensional functions. Both methods have advantages and disadvantages:

One dimensional corrections:
- Easy to do
- Fully transparent
- Fast
- Can be model dependent in complicated cases
- May not accommodate for correlated inefficiencies.

Multidimensional corrections:
- Corrections can be applied as weights on an event-by-event basis.
- Results can be easily used outside the collaboration
- Less model dependent.
- Incorporates correlated inefficiencies.
- Requires large MC statistics, basically (one dimensional statistics)[4].
- Requires large data statistics — each 4-dimentional cell in histogram should be highly populated, overwise systematic uncertainties would be enormously high.
- Too many edges — each edge (of a detector element or of a corrected cell) can not be well corrected. With a complicated detector like WASA the systematic error appear to be very high.

So one can see that the multidimensional correction algorithm is not applicable in our case. But we can make an intermediate method — 2-dimensional corrections, at least for some distributions, to show, that one and two dimensional corrections methods give the same results within uncertainties.

To make 2D corrections we will take Dalitz plots (2D histograms) and correct them in the spirit of the 1D method. Afterwards we can reduce the Dalitz plots to 1D histograms and compare them to the same 1D histograms, obtained by the 1D correction algorithm. This is demonstrated in *Fig. 4—11*.

---

[a] If the data covers full acceptance range than any model is applicable, otherwise one should use model as close to data as possible.
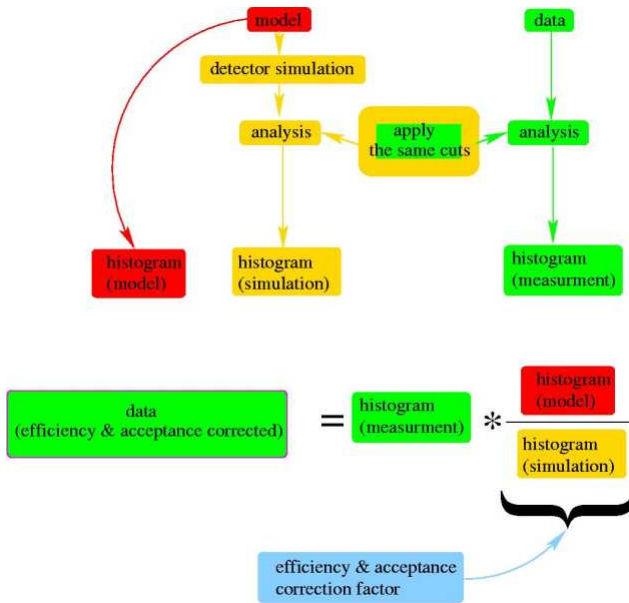[b] The example of the multidimensional corrections will be shown later, not 4D, but only 2D.

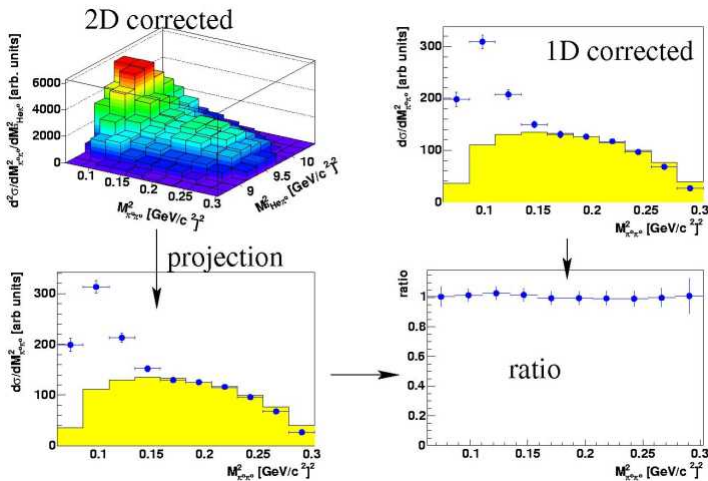*Fig. 4—10 Common method for efficiency and acceptance corrections.*

Fig. 4—11 Ambiguities with different correction algorithms. Upper left: Dalitz plot $M^2_{\pi^0\pi^0}$ vs. $M^2_{^3\text{He}\pi^0}$ 2D corrected. Lower left: projection of a Dalitz plot — $M^2_{\pi^0\pi^0}$. Upper right: the same as lower left, but achieved with 1D correction algorithm. Lower right: ratio between 1D corrected and 2D corrected histograms.

One can see that both methods agree very well within statistical errors. It means that systematical errors due to the chosen correction procedure are negligibly small.

55

5 Results

In this chapter the results of two-pion production will be discussed. Differential observables will be shown and compared to theoretical models. Possible explanations of different effects appearing in the data will be made at the end of this chapter.

5.1 Total cross section.

The total cross-section can be obtained from:

$$N_{\exp} = \sigma \cdot L_{\mathrm{int}} \cdot \varepsilon_{eff-acc}$$

where $N_{\exp}$ is number of events after reconstruction; $\varepsilon_{eff-acc}$ the efficiency and acceptance correction of data; σ is the total cross-section and L_{int} the integrated luminosity. $N_{\exp} / \varepsilon_{eff-acc}$ would give us the expected number of events, if our detector would not have any holes, cover the whole phase space and detection and reconstruction efficiency would be unity. This part we can estimate rather easily for any reaction *Chapter4.4*. But on the other side of the expression we have the integrated luminosity, which is much more difficult to estimate:

$$L_{\mathrm{int}} = \int L \cdot \varepsilon \cdot dt \ .$$

In this expression L is the luminosity ($L = I \cdot \rho$; I is the beam current, ρ is the target density). And ε is the parameter which should account for all imperfections of the measurements: the beam is bunched, so sometimes we do not have beam in the target region. Sometimes we have beam but no target. In addition we have some dead time in our data acquisition system and some trigger inefficiencies. So in our case

$$\varepsilon = \varepsilon_{beam} \cdot \varepsilon_{t\arg et} \cdot \varepsilon_{DAQ} \cdot \varepsilon_{trigger}$$

Each of these parameters varies in time, even the beam current in our case varies from 1.2 up to 2.1 mA. So the calculation of integrated luminosity by this method is next to impossible in the case of CELSIUS.

Fortunately there is another way to obtain the total cross-section. Let us call $N_{corr} = N_{\exp} / \varepsilon_{eff-acc}$ and look at the ratio of that number of expected reconstructed events for two different reactions, which are measured with same triggers simultaneously such as single and double π^0 production in *pd* collisions leading to $^3\mathrm{He}$:

$$\frac{N_{corr}(pd \to {}^3\mathrm{He}\pi^0)}{N_{corr}(pd \to {}^3\mathrm{He}\pi\pi)} = \frac{\sigma(pd \to {}^3\mathrm{He}\pi^0)}{\sigma(pd \to {}^3\mathrm{He}\pi\pi)}$$

For these two reactions the beam is the same, the target is the same the DAQ is the same and even the trigger is exactly the same. So all inefficiencies cancel out. In case of $pd \to {}^3\mathrm{He}\pi^0\pi^0$ we could even have a wrong GEANT description of our detector and it

also would cancel. And since we have a reaction to normalize to, we better do it this way, thus reducing our systematic error substantially.

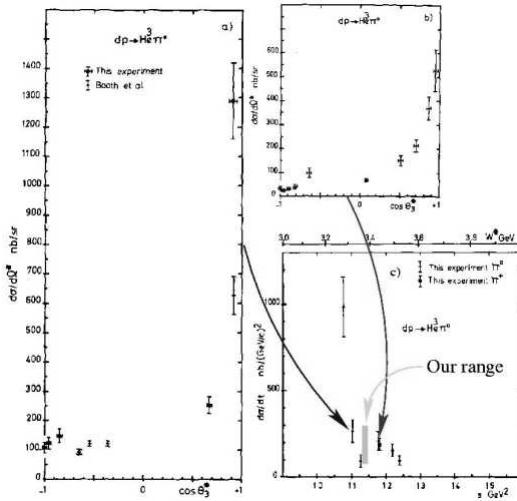The cross section of $pd \rightarrow {}^3He\pi^0$ is known from Saclay measurements [35], see *Fig. 5—1*.

Fig. 5—1 Saclay data for $pd \rightarrow {}^3He\pi^0$ [35]. a) ${}^3He$ angular distribution in the CMS at 2.83 GeV/c beam momentum; b) same distribution at 3.5 GeV/c beam momentum; c) cross-section at 180°. as a function of s, the center of mass energy squared. The shaded bar area shows our energy with corresponding errors.

One can see that the angular distribution for $\Theta^*_{{}^3He} > 90°$ is flat. Unfortunately the errors in cross-sections are large. In addition the data point at $s \approx 11$ GeV^2 is outside the trend and it is not clear, whether it is due to an error in the experiment or due to dynamics at the η threshold, which is right at this point. By comparison with the angular distribution obtained in our analysis of the ${}^3He\pi^0$ channel, see *Fig. 5—2*, we can derive the absolute cross-section.
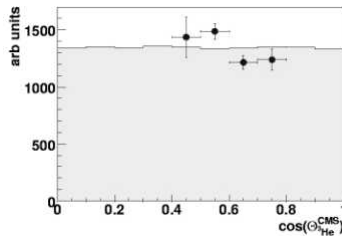

Fig. 5—2 ${}^3He$ angular distribution in CMS system for the $pd \rightarrow {}^3He\pi^0$ reaction. The shaded area represents phase space.

Note that in our case we had a proton beam, whereas Saclay had a deuteron beam, that is why in the CMS we have different directions of the *z*-axis. So *Fig. 5—1* and *Fig. 5—2* are just mirrored. Adopting $d\sigma / d\Omega = 100\,\mu\text{b/sr}$ for $\cos\Theta > 0$ from the Saclay data for the $^3\text{He}\pi^0$ channel our data yield the following total cross-sections for the $\pi\pi$ channels: $\sigma(pd \rightarrow {}^3\text{He}\pi^0\pi^0) = 2.8(3)\,\mu\text{b}$ and for $\sigma(pd \rightarrow {}^3\text{He}\pi^+\pi^-) = 5.1(5)\,\mu\text{b}$.

The main part of the uncertainty in our results does not originate from statistics, but from systematics — we know the single pion cross-section only by interpolation and can not compare the angular distributions at exactly our energy. Hopefully new results from COSY on this reaction should come soon, and this would improve the uncertainty in our analysis.

There is yet another way to estimate the cross-section of our reaction: the cross-section for $pd \rightarrow {}^3\text{He}\eta$ is known for this energy with very high precision due to searches of eta-mesic nuclei. And in parallel to our reaction also the measurements of $pd \rightarrow {}^3\text{He}\eta$ were performed. Unfortunately it is very difficult to normalize our cross-section reliably to this reaction. Since η tagging includes the Zero-Degree spectrometer, *Chapter 2.4.3*, one should also include the optics of magnets into the estimations of inefficiencies, which is difficult. In addition since we are here very close to threshold the cross section varies strongly with energy and the energy of the beam changes slightly even during the cycle. But at least we may check the consistency of our results. To perform such a type of analysis, we have to select η's. The easiest way is by selecting the $\eta \rightarrow \gamma\gamma$ branch. The η is produced just at threshold, so it is nearly at rest in the CMS. Therefore the photons are coplanar both in the CMS and lab frames. In addition the energy of photons is very high, so it is not a problem to select those events.
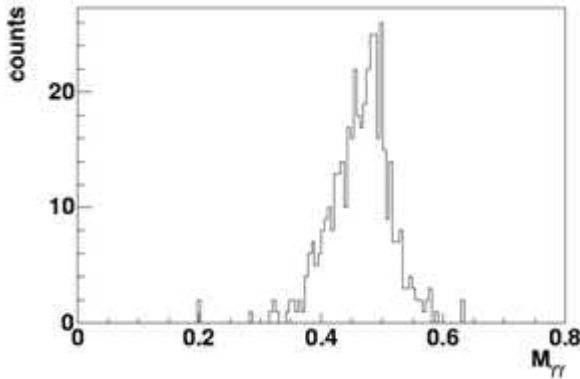

Fig. 5—3 Selection of $\eta \rightarrow \gamma\gamma$ events. Invariant mass of two photons after selection.

In order to obtain a clean spectrum of $\eta \rightarrow \gamma\gamma$ events we applied the following cuts: $\phi(\gamma_1 \wedge \gamma_2) > 3.1$ [rad] (planarity cut); $E_{\gamma_1} + E_{\gamma_2} > 0.4\,\text{GeV}$; $2.1 < \delta_{\gamma\gamma} < 2.5$ [rad] (opening angle cut). Such cuts do not reduce the η statistics but remove background. The acceptance for $\eta \rightarrow \gamma\gamma$ is 85%. Together with the known $pd \rightarrow {}^3\text{He}\eta$ cross-section of $0.409\,\mu\text{b}$, and the branching $\eta \rightarrow \gamma\gamma$ of 39.43% [36], this brings us to roughly the same

order of magnitude for the $\pi\pi$ cross-sections: $10\,\mu b$ for $\pi^0\pi^0$ instead of $2.8\,\mu b$ from previous method.

5.2 Invariant mass distributions.

In this section the experimental results for the distributions of invariant masses are presented for both the $pd \rightarrow {}^3\text{He}\pi^0\pi^0$ and the $pd \rightarrow {}^3\text{He}\pi^+\pi^-$ reactions. They are discussed first with respect to pure phase space distributions. The discussion about the pertinent deviations from phase space and their implications about the nature of the ABC effect will be presented in Chapter 6.

For an (unpolarized) three-body reaction there are only 4 independent observables with 3 invariant mass distributions. For the particular case of neutral pions there are only two, because we can not distinguish between first and second π^0. First let us ask, what a difference could we expect between neutral and charged pions? In the initial system we have a proton and a deuteron. The isospin of the deuteron is 0, that of a proton is ½ So the isospin of the initial system is ½ In the final system we always have ${}^3\text{He}$ and the double pion system. The isospin of each single pion is 1. So the system of two pions can be in isospin 0, 1, 2 states. Since pions are identical bosons in their isospin space, their wave function must be symmetric, i.e. $(-1)^{L+S+I} = +1$, with orbital momentum L between two pions, spin S of the pion pair (S=0, since pions have no spin) and isospin I of the pion pair ($I = 0,1,2$). This implies that for pions only odd-odd or even-even I-L combinations are allowed. In addition, due to the identity of the pions in the $\pi^0\pi^0$ channel $L = 1$ and in consequence also $I = 1$ is not allowed in this case, therefore $I = 0$ or 2. For the $\pi^+\pi^-$ channel $L = 1$ is allowed, hence also $I = 1$.

Summarizing, we see that in case of $pd \rightarrow {}^3\text{He}\pi^0\pi^0$ with the initial isospin ½ the $\pi^0\pi^0$ system can be only in an $I = 0$ state. And in case of $pd \rightarrow {}^3\text{He}\pi^+\pi^-$ the $\pi^+\pi^-$ system can be in $I = 0,1$ states. However in the latter case this is combined with $L = 1$. Hence the isovector part of the $M_{\pi^+\pi^-}$ distribution must be proportional to k^2 (where k is the momentum in the $\pi - \pi$ system)[a], so it has to be 0 at threshold and to rise towards higher invariant masses. Since the isovector $\pi\pi$ channel thus carries the quantum numbers of the ρ meson, this channel may be dominated by ρ excitation in the appropriate mass region.

Since the charged pions are heavier than the neutral ones, the threshold values $M_{\pi^+\pi^-}^{\min} = 0.2791$ GeV and $M_{\pi^0\pi^0}^{\min} = 0.26995$ GeV differ by nearly 10 MeV. So we expect a different behavior of the $M_{\pi^0\pi^0}$ and $M_{\pi^+\pi^-}$ distributions near thresholds due to the pion mass difference, and at high invariant masses due to the I=1 contribution in the

---

[a] One can decompose amplitude into partial waves: $A_l \propto k^l$. Since cross-section is equal to amplitude squared, then in case of *L=1* $\sigma \propto k^2$

$\pi^+\pi^-$ channel. For the isoscalar part the isospin relations give $\sigma(\pi^+\pi^-)_{I=0} = 2\sigma(\pi^0\pi^0)_{I=0}$ [a].

In the $M_{^3\mathrm{He}\pi}$ spectra we expect to see a strong Δ excitation, if the early explanations of the ABC effect [11],[38],[39] are correct. For a pure Δ excitation and isospin conservation the $M_{^3\mathrm{He}\pi^+}$ and $M_{^3\mathrm{He}\pi^-}$ spectra should look exactly the same. If the $\pi^+\pi^-$ production proceeds partly via a N^* resonance decaying through Δ, then $M_{^3\mathrm{He}\pi^+}$ should be more excited compared to $M_{^3\mathrm{He}\pi^-}$ due to different isospin coefficients for Δ^{++} and Δ^0 excitations [b]. One should remember that ρ^0 can not be produced in $\Delta\Delta$, due to spin-isospin selection rules, but only through N^*, most probable through $N^*(1520)$.

Fig. 5—4 shows the Dalitz plots of $M^2_{\pi^0\pi^0}$ versus $M^2_{^3\mathrm{He}\pi^0}$ and $M^2_{\pi^+\pi^-}$ versus $M^2_{^3\mathrm{He}\pi^\pm}$ respectively (both $M^2_{^3\mathrm{He}\pi^+}$ and $M^2_{^3\mathrm{He}\pi^-}$ are filled into one histogram for better comparison with the $\pi^0\pi^0$ case).
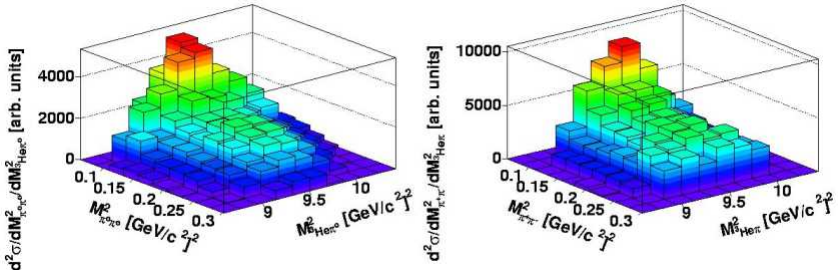

Fig. 5—4 Dalitz plots for the systems $^3\mathrm{He}\pi^0\pi^0$ (left) and $^3\mathrm{He}\pi^+\pi^-$ (right).

In both cases we see a strong enhancement at small $\pi\pi$ masses, which is particularly pronounced in the $\pi^0\pi^0$ case. Fig. 5—5 displays the measured $M_{\pi^0\pi^0}$ and $M_{^3\mathrm{He}\pi^0}$ differential distributions in comparison with pure phase space predictions.

In $M_{^3\mathrm{He}\pi^0}$ we see a strong Δ excitation at $2m_N + m_\Delta$ (right part of *Fig. 5—5*). On the left part of *Fig. 5—5* one can clearly see the ABC effect as a large (relative) enhancement close to the $\pi\pi$ threshold. One can also see that at high invariant masses the $M_{\pi^0\pi^0}$ distribution behaves like phase space.

---

[a] $|I = 0|I_3 = 0\rangle = 1/\sqrt{3}|\pi^+\pi^-\rangle - 1/\sqrt{3}|\pi^0\pi^0\rangle + 1/\sqrt{3}|\pi^-\pi^+\rangle$; squaring this expression results in $\sigma_{I=0} = \tfrac{2}{3}\langle\pi^+\pi^-|\pi^+\pi^-\rangle + \tfrac{1}{3}\langle\pi^0\pi^0|\pi^0\pi^0\rangle$, so $\sigma_{\pi^+\pi^-} = \tfrac{2}{3}\sigma_{I=0}$, $\sigma_{\pi^0\pi^0} = \tfrac{1}{3}\sigma_{I=0}$

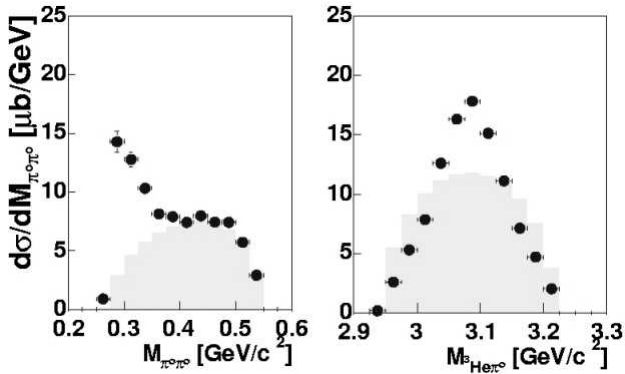[b] For example $\dfrac{\sigma(N^*(1440) \to \Delta^{++}\pi^-)}{\sigma(N^*(1440) \to \Delta^0\pi^+)} = 9$

Fig. 5—5 Differential cross-section in dependence of $M_{\pi^0\pi^0}$ (left) and $M_{^3\mathrm{He}\pi^0}$ (right) for the reaction $pd \to {^3}\mathrm{He}\pi^0\pi^0$. Shaded areas represent phase space distributions, in the left histogram phase space is normalized to touch the data, in the right one to equal the integral cross-section

As in the $\pi^0\pi^0$ case also the $\pi^+\pi^-$ channel exhibits a strong Δ excitation in the $M_{^3\mathrm{He}\pi}$ spectrum, see *Fig. 5—6*. In detail the Δ excitations in $M_{^3\mathrm{He}\pi^+}$ and $M_{^3\mathrm{He}\pi^-}$ appear to be slightly different, which could indicate some small $N^*(1520)$ contribution as discussed above. The $M_{\pi^+\pi^-}$ spectrum looks also slightly different from the $M_{\pi^0\pi^0}$ spectrum — the ABC bump appears to be considerably smaller and there is an additional (relative) enhancement at high invariant masses. If we plot both invariant mass distributions on top of each other (reducing the $\pi^+\pi^-$ cross-section by factor of two, the isospin factor for the isoscalar part), (Fig. 5—7), then the
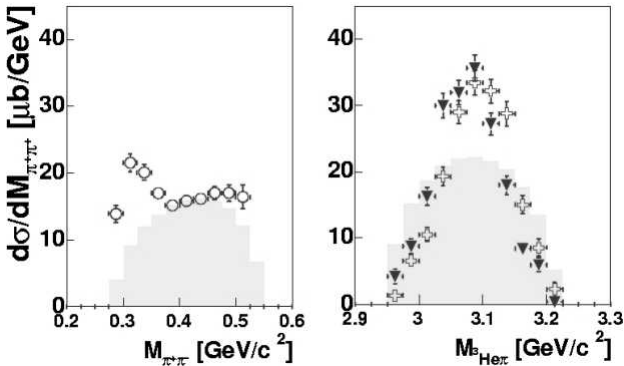

Fig. 5—6 Differential cross-section in dependence of $M_{\pi^+\pi^-}$ (left) and $M_{^3\mathrm{He}\pi}$ (right). $M_{^3\mathrm{He}\pi^+}$ is marked by pluses, and $M_{^3\mathrm{He}\pi^-}$ by inversed triangles. Shaded areas represent phase space distributions.

61

bulk part of both distributions agrees quite well, exhibiting the main contribution to be isoscalar. The differences at high $M_{\pi^+\pi^-}$ can be associated to an $I=1$ contribution yielding $\sigma_{\pi^+\pi^-}(I=1) = \sigma_{\pi^+\pi^-} - 2\sigma_{\pi^0\pi^0} \approx 0.6\,\mu b$.

This value depends strongly on the relative normalization of $\pi^+\pi^-$ and $\pi^0\pi^0$ channels. According for their uncertainties (see *Chapter 5.1*) we could have an isovector contribution as large as $1\,\mu b$ in support of the findings in the inclusive measurements [6]. An alternative estimate of the isovector contribution will be given in *Chapter 6.1.8*.
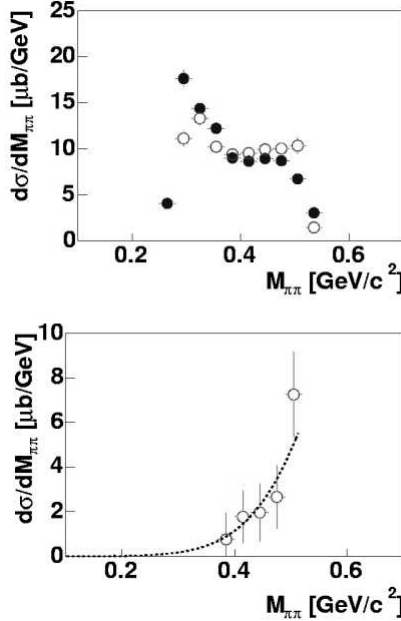
Fig. 5—7 Distributions of $M_{\pi^+\pi^-}$ (open symbols) and $M_{\pi^0\pi^0}$ (filled symbols) shown at the top of the figure. The $\pi^+\pi^-$ cross-section has been reduced by a factor of two. Bottom: extraction of the I=1 contribution, assuming that the difference at high invariant masses is due to I=1 contamination. The dashed line represents a possible ρ contribution, parameterized by an appropriate Breit-Wigner function[a]

5.3 Angular distributions.

Here we restrict the discussion to the most interesting angular distributions shown in the *Fig. 5—8*. Further angular distributions are given in the appendix chapter 11.

---

[a] $A \propto \dfrac{1}{(M_{\pi\pi} - M_{\rho})^2 + \Gamma_{\rho}^2/4}$, where $M_{\rho} = 0.77\,\text{GeV}$ and $\Gamma_{\rho} = 0.15\,\text{GeV}$
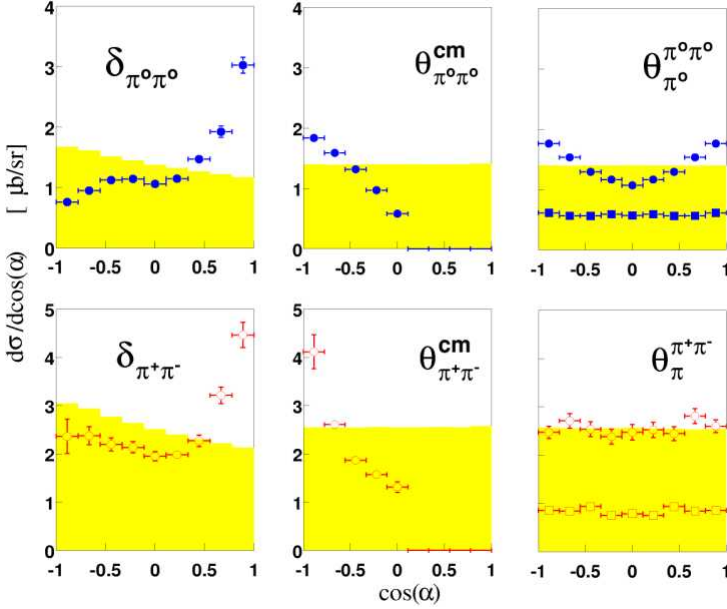
Fig. 5—8 displays the angular distributions for $\delta_{\pi\pi}$, the opening angle between the momentum vectors of the two pions, for the angle of the total momentum of $\pi\pi$ system $\Theta_{\pi\pi}^{cms} = -\Theta_{^3\text{He}}^{cms}$ — all in the overall center of mass system — and for $\Theta_{\pi}^{\pi\pi}$, the pion angular distribution in the $\pi\pi$ subsystem (Jackson frame), which is shown both for the full mass region (circles) and for $M_{\pi\pi} < 0.34\,\text{GeV}$ (squares).

Fig. 5—8 Angular distributions for $\delta_{\pi\pi}$, the opening angle between the momentum vectors of the two pions, for the angle of the total momentum of $\pi\pi$ system $\Theta_{\pi\pi}^{cms} = -\Theta_{^3\text{He}}^{cms}$ — all in the overall center of mass system — and for $\Theta_{\pi}^{\pi\pi}$, the pion angular distribution in the $\pi\pi$ subsystem (Jackson frame). For the latter the data are plotted also with the constraint $M_{\pi\pi} < 0.34\,\text{GeV}$. Top: $pd \to {}^3\text{He}\pi^0\pi^0$, bottom: $pd \to {}^3\text{He}\pi^+\pi^-$. Shaded area is phase space.

For the discussion of the angular distributions we go through Fig. 5—8 step by step. In the first column, where $\delta_{\pi\pi}$ distributions are plotted, we see a strong spike at small relative angles. This relates to the spike (see Fig. 5—7) at small $\pi\pi$ invariant masses, since low invariant masses belong to $\pi\pi$ pairs with small relative momentum. Such pairs must move essentially in parallel both in the lab system and in the overall CMS thus having a small opening angle $\delta_{\pi\pi} \to 0$, as indeed is borne out in our data for $\delta_{\pi\pi}$. This is fully supported by the distributions of the azimuthal angle difference $\Delta\phi_{\pi\pi}$ of the two pions, which also peaks at $\Delta\phi_{\pi\pi} \to 0$ (see Appendix 11.2). The next column exhibits the $\Theta_{\pi\pi}^{cms}$ distributions, which are the mirrored ${}^3\text{He}^{CMS}$ angular distributions. They show a behavior consistent with previous inclusive ABC measurements [6]. Most

interesting is the third column, the $\Theta_\pi^{\pi\pi}$ distribution, i.e. the pion angular distributions in the $\pi\pi$ subsystem. Here the coordinate system is chosen such that the z axis coincides with the beam axis. So $\Theta_\pi^{\pi\pi}$ is the angle between pion momenta in the $\pi\pi$ rest frame and the beam axis. This is the socalled Jackson reference system. It is appropriate for a study of the contributions of the partial waves in the particular subsystem [37]. Let us first look on the circle symbols in the figure, representing the full unconstrained angular distributions. They look very much like containing some p-wave admixture. But since p-wave is not allowed in the $\pi^0\pi^0$ system, it implies that we have a s-d wave interference, which behaves exactly the same way[a]. However if we consider the $\Theta_\pi^{\pi\pi}$ angular distribution belonging to just the ABC region (squares in *Fig. 5—8*), then it is flat, which means that the ABC effect is of scalar nature. As we derived before it also can be only isoscalar. So we have the important result that the ABC is a scalar-isoscalar effect. This feature is even better visible, if $\Theta_\pi^{\pi\pi}$ is plotted as a function of the invariant mass, *Fig. 5—9*.
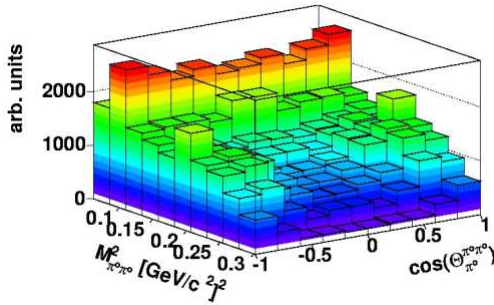

Fig. 5—9 Lego plot of $M_{\pi^0\pi^0}^2$ versus $\cos\Theta_\pi^{\pi\pi}$ with respect to the beam axis. The vertical scale is in arbitrary units.

Clearly at high invariant masses the angular distribution is not flat, it is flattening out, however, towards lower invariant masses.

---

[a] $A \propto A_S + A_D$ — amplitude of the reaction. Since $A_S \propto const$ and $A_D \propto \cos^2 \Theta_\pi^{\pi\pi}$, $A^2 \propto const^2 + 2 \cdot const \cdot \cos^2 \Theta_\pi^{\pi\pi} + \cos^4 \Theta_\pi^{\pi\pi}$. The second is the interference term. Compare to $A_P^2 \propto \cos^2 \Theta_\pi^{\pi\pi}$ one can find that the functional behavior is exactly the same.

6 Discussion: "Towards the nature of the ABC effect".

In this section different models will be discussed and presented. It will be attempted to get an explanation of the ABC effect and relate it to other systems. First the usual $\Delta\Delta$ model — as introduced originally by [11] and used by many other authors [38],[39] in more sophisticated treatments — will be discussed (*see Chapter6.1.1*). The invalidity of such models as well as possible ways of improvement will be shown. As a first step into a more detailed description, one can consider the inclusion of Fermi-motion inside the nucleus (*Chapter6.1.2*), which however does not improve the description with the conventional $\Delta\Delta$ model. For a better description several different ideas are suggested from the naive bound $\Delta\Delta$ model (*Chapter6.1.3*) up to a more complicated $\Delta\Delta$-FSI model, considered to be the correct description of the ABC effect (*Chapter6.1.4*). It will be shown, that the $\Delta\Delta$-FSI model can explain not only differential observables of $pd\rightarrow{}^3\mathrm{He}\pi\pi$ data at our energy, but also gives the correct dependence of the total cross-section (*Chapter6.1.5*) as well as differential observables of $pn\rightarrow d\pi\pi$ reaction at $T_p=1.037\,\mathrm{GeV}$. Moreover it reproduces inclusive spectra for $dd\rightarrow{}^4\mathrm{HeX}$ reactions (*Chapter6.1.9*). Finally some other less probable explanations will be mentioned (*Chapter6.1.7*).

6.1.1 The traditional $\Delta\Delta$ model

The basic ingredients for a $\Delta\Delta$ excitation as treated in many theoretical papers [11],[12],[38],[39] are given by

$$\sigma \propto \Delta_1 \cdot \Delta_2 \cdot (1+3\cos(\Theta_{\pi_1}^{N_1\pi_1})) \cdot (1+3\cos(\Theta_{\pi_2}^{N_2\pi_2})) \cdot phase\ space \tag{1}$$

where $\Theta_\pi^{N\pi}$ is the angle of the pion in the nucleon-pion subsystem, with respect to the beam-axis as the z-axis. Here and later we use *c=1* (speed of light), so it will be skipped for convenience in formulas, so all variables like *M*, *P*, Γ are in GeV. The symbol Δ in the above equation represents the Breit-Wigner term with an energy-dependent width for the Δ excitation:

$$\Delta = \frac{\Gamma^2 / P_\pi^{N\pi}}{\left(M_{N\pi}^2 - M_\Delta^2\right)^2 + M_\Delta^2 \cdot \Gamma^2} \tag{2}$$

with $M_\Delta=1.23\,\mathrm{GeV}$, $P_\pi^{N\pi}$ denoting the momentum of the pion in the nucleon-pion subsystem, and

$$\Gamma = \frac{\gamma \cdot R^2 \cdot \left(P_\pi^{N\pi}\right)^2}{1+R^2 \cdot \left(P_\pi^{N\pi}\right)^2} \cdot P_\pi^{N\pi} \tag{3}$$

with $\gamma=0.74$ and $R=6.3$ c/GeV, see [11], i.e. $\Gamma(M_\Delta)=0.110\,\mathrm{GeV}$.

This ansatz leads to the $M_{\pi\pi}$ distribution shown in *Fig. 6—1* by the solid line. Compared to a phase space distribution a (relative) enhancement is seen both at small and large $\pi\pi$ masses. As demonstrated in Ref.[11] — and reiterated in many publications of the $\Delta\Delta$ calculations [see e.g. [12]] — the two enhancements arise from the term $\Delta_1\Delta_2$

in eq.1, which is at maximum for the two cases, where the two pions emerging from the decay of the two Δ's move either parallel or antiparallel to each other i.e. $\delta \to 0$ or π. This is valid, however, only under the condition that the two nucleons emerging from the Δ decay have no (significant) relative motion — as is the case, when they are captured in a final nuclear bound state.
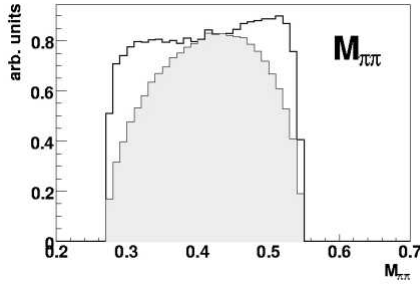

Fig. 6—1 $M_{\pi\pi}$ distribution: solid line is the result of $\Delta\Delta$ calculations according to eq.1 the shaded area denotes phase space normalized to touch the solid line.

This scenario immediately translates into one with regard to the relative motion of the two Δ. As we see from *Fig. 6—2* there is a clear correlation between $\pi\pi$ invariant mass and $\Delta\Delta$ relative momentum, $q_{\Delta\Delta}$. And the low-mass enhancement corresponds to a $\Delta\Delta$ pair with minimum relative momentum, whereas the high-mass enhancement corresponds to a $\Delta\Delta$ with maximum relative motion.

By comparing *Fig. 6—1* and *Fig. 5—5*, one sees that this $\Delta\Delta$ model is far from a realistic description of the data — the first bump should be much higher and the second one should be absent.

In order to make a calculation close to observations w e have to enhance $\Delta\Delta$ configurations with small relative momentum and simultaneously suppress $\Delta\Delta$ configurations with large relative momentum.
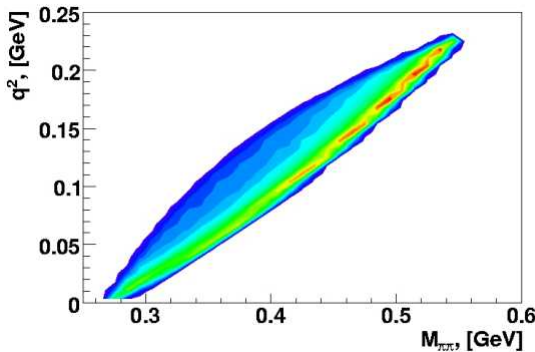

Fig. 6—2 Distribution of the invariant mass $M_{\pi\pi}$ with respect of the relative momentum $q_{\Delta\Delta}$ of the two Δ in the CMS, as obtained by simulating the eq.1, at $T_p = 0.895$ GeV .

This may be achieved by requiring a bound or quasi-bound state in the $\Delta\Delta$ system (*Chapters 6.1.3, 6.1.4*). Indeed, the $\Delta\Delta$ interaction is thought to be attractive [40], and even bound $\Delta\Delta$ states have been predicted [41]. Before continuing with the discussion of bound $\Delta\Delta$ states, we first want to improve the model further by including the Fermi motion of the nucleons in ^{3}He. So far it was tacitly assumed that $P_N = P_{{}^3\text{He}}/3$.

6.1.2 Fermi momentum of a nucleon inside nuclei.

To incorporate the Fermi motion into the simulation we apply a trick. After simulation of an event by a MC program based on TGenPhaseSpace package from ROOT [32] we have only the momentum of ^{3}He as an observable, but for the improved calculation we need the momentum of each of the nucleons. To this end we need to assign a Fermi momentum. Since the sum of all 3 Fermi momenta must be 0, we need to simulate the momentum of only two nucleons, the momentum of third nucleon can then be calculated using the condition above. For each nucleon we have to simulate Θ , ϕ and p. The variable ϕ should be evenly distributed in the interval $[0, 2\pi]$, Θ should be distributed like the *cos* function[a], i.e. the $\cos\Theta$ distribution should be flat in the interval $[-1,1]$, and the absolute value of the momentum p should follow the momentum distribution in nuclei. For simplicity we can use the probability function,

$$\wp(p) \propto \left[\frac{p \cdot (k^2 - \beta^2)}{(p^2 + \beta^2)(p^2 + k^2)} \right]^2 \qquad (4)$$

based on the Hulthen wave function [42], with $k = 0.26\,\text{GeV/c}$, $\beta = 0.0456\,\text{GeV/c}$. These coefficients are best suited for the deuteron. If we calculate the Fermi-motion for reaction $pn \to d\pi\pi$ we use exactly this probability distribution. For ^{3}He one should use different function:

$$\wp(p) \propto \left[p \cdot e^{-\left(\frac{p}{p_0}\right)^2} \right]^2 \qquad (5)$$

where $p_0 = 0.17\,\text{GeV/c}$; this assumes the wave function of ^{3}He to be a Gaussian with width $\sigma = p_0/2$ in momentum space, corresponding to a size of ^{3}He in coordinate space of $\sqrt{\langle r^2 \rangle} = \sqrt{3}\,\dfrac{\hbar}{p_0} = 2.0\,fm$. However eq.5 assumes the distribution to be the same for all nucleons which might not always be the case. If we want to simulate the reaction $pd \to N\Delta\Delta \to {}^3\text{He}\pi\pi$, then two nucleons participating in the Δ formation would be distributed deuteron-like in their rest frame, and the third nucleon would be distributed as given by the ^{3}He in ^{3}He rest frame. So the most probable configuration for this case will be a deuteron + nucleon partition. This is in spirit of the formfactor used in the

---

[a] This is true for s-wave nucleons i.e. for A≤4, which we consider.

description of the transfer reactions, giving the overlap of the deuteron + nucleon configuration with the ^{3}He wavefunction [3].

It is difficult to get the momentum distribution for such configuration analytically. However, we can easily simulate it, and the result is very close to eq.5 with $p_0 = 0.12 \, \text{GeV/c}$

In the figure below one can see all distributions: eq. 4, eq.5 with $p_0 = 0.17 \, \text{GeV/c}$ and $p_0 = 0.12 \, \text{GeV/c}$ as well as the simulated d+N configuration of ^{3}He.
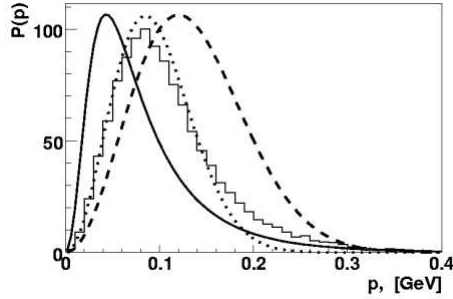
Fig. 6—3 *Probability distributions for the momentum of nucleons inside nuclei. The dashed curve corresponds to a Gaussian wave function with $p_0 = 0.17 \, \text{GeV}$. The solid line represents the Hulthen wave function. The solid histogram gives the simulated momentum distribution for the d+N configuration inside ^{3}He. The dotted line shows the eq.5 ansatz with $p_0 = 0.12 \, \text{GeV}$.*

Since the momentum distribution for the d+N configuration inside the ^{3}He can be well fitted with eq.5 using a slightly different parameter ($p_0 = 0.12 \, \text{GeV/c}$ instead of $p_0 = 0.17 \, \text{GeV/c}$), we will rather use this analytical expression then simulate such configuration for each event, which is time consuming.

In order to get a random x according to some probability function $f(x)$ in the range $[x_1, x_2]$, one should make the following operations. In the range $[x_1, x_2]$ the function $f(x)$ reaches a minimum value y_1 and a maximum value y_2. First we create a pair of randoms $x \in [x_1, x_2]$ and $y \in [y_1, y_2]$ and then make the following comparison: if $f(x) > y$, then this value of x is accepted, otherwise the procedure is repeated.

The results of introducing the Fermi motion will be shown in the next Chapter, together with model calculations.

6.1.3 Bound $\Delta\Delta$ system.

To build a $\Delta\Delta$ model, which is able to adequately describe the data, we should take the usual $\Delta\Delta$ model, from eq.1 include Fermi motion, eq.5 with $p_0 = 0.12 \, \text{GeV/c}$, for a more realistic description, and multiply it with a formfactor, for the binding of the two Δs. As formfactor we choose a monopole type formfactor:

$$F(q_{\Delta\Delta}) \propto \left(\cfrac{1}{1+\left(\cfrac{q_{\Delta\Delta}}{q_0}\right)^2} + a \right) \qquad (6)$$

where $q_{\Delta\Delta}$ is the relative momentum between two Δ in the CMS[a]. The coefficients q_0 and a are fitted for the best reproduction of the data, *Fig. 6—4*. The coefficient q_0 represents the size of the $\Delta\Delta$ bound object. The second coefficient just says that not all Δs are bound. So finally the formula for the bound $\Delta\Delta$ model would be:

$$\sigma \propto \Delta_1 \cdot \Delta_2 \cdot (1+3\cos\Theta_{\pi_1}^{N_1\pi_1}) \cdot (1+3\cos\Theta_{\pi_2}^{N_2\pi_2}) \left(\cfrac{1}{1+\left(\cfrac{q_{\Delta\Delta}}{q_0}\right)^2} + a \right)^2 \cdot PS \qquad (7)$$

where PS denotes phase space here and with the optimized parameters $a = 0.2\,\text{GeV}$ and $q_0 = 0.09\,\text{GeV/c}$. The latter is correlated with the size of the bound $\Delta\Delta$ by

$$\sqrt{\langle r^2 \rangle} = \frac{\sqrt{6}\hbar c}{2q_0} \approx 3.2\,\text{fm}\,,$$ i.e. a size similar to that of the loosely bound deuteron.

The result of such a calculation is shown in *Fig. 6—4.* It should be mentioned that one can vary the optimization parameters in quite a broad range $q_0 \in [0.7, 1.2]\,\text{GeV/c}$ with roughly the same result.
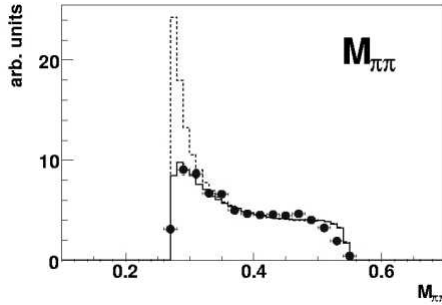
Fig. 6—4 Invariant mass of $\pi^0\pi^0$. Data and bound $\Delta\Delta$ calculations. The solid line gives a calculation including Fermi motion, dashed line – without Fermi motion, but with the same fit parameters ($a = 0.2\,\text{GeV}$ and $q_0 = 0.09\,\text{GeV/c}$).

---

[a] By including the Fermi-motion we know the momentum of each nucleon on a event by event basis. So knowing the momentum of nucleons and pions we can calculate the 4-momentum of Δ's, providing us access to such variables like $q_{\Delta\Delta}$ and M_Δ

One can see that the ansatz eq.7 describes the data reasonably well. The effect of Fermi motion makes the peak at small invariant mass broader, as is obvious from the discussion at the end of *Chapter 6.1.1*. We note in passing that one can also fit the data points without the requirement of Fermi motion. To do so one would need to assume a higher q_0 parameter, equivalent to a smaller radius of the $\Delta\Delta$ molecule. Saying that we have no Fermi motion, we entirely assume that the probability function for the momentum distribution inside the ^{3}He is a δ-function. Taking the Gaussian parameterization of the Fermi motion, one has to assume a smaller q_0 to fit the data with the same accuracy. The higher the allowed Fermi motion, the better should the binding of $\Delta\Delta$ be to satisfy our data, which looks reasonable. It means that in the free case the $\Delta\Delta$ binding would need to be much stronger to give the same invariant mass distribution as in the ^{3}He case.

Here and later on we will always tacitly assume a d+N type Fermi motion. It should be mentioned that the bound $\Delta\Delta$ ansatz describes also the other distributions reasonably well. On the figure below (*Fig. 6—5*) one can see the calculations of this model together with the data from *Fig. 5—8*. These calibrations are published in Ref. [43] together with the data.
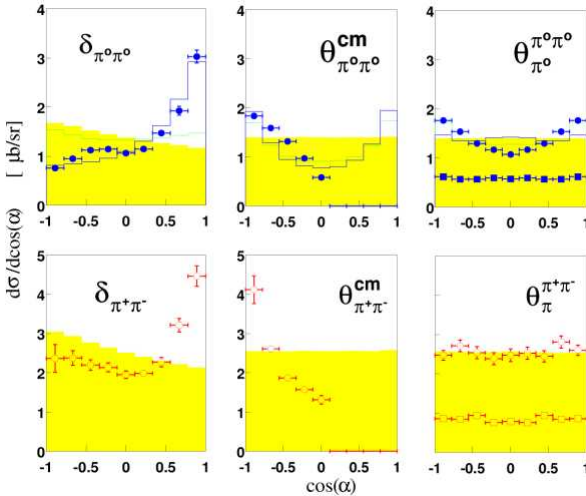
Fig. 6—5 Angular distributions for $\delta_{\pi\pi}$, *the opening angle between the momentum vectors of the two pions, for the angle of the total momentum of $\pi\pi$ system* $\Theta_{\pi\pi}^{cms} = -\Theta_{^3He}^{cms}$ *— all in the overall center of mass system — and for* $\Theta_\pi^{\pi\pi}$, *the pion angular distribution in the $\pi\pi$ subsystem (Jackson frame) For the latter the data are plotted also with the constraint* $M_{\pi\pi} < 0.34\,GeV$ *(squares). Top:* $pd \to\ ^3He\pi^0\pi^0$, *bottom:* $pd \to\ ^3He\pi^+\pi^-$ *The shaded area is phase space. The dashed green line is the calculation of the $\Delta\Delta$ model. The solid blue line is the results of the bound $\Delta\Delta$ anzatz (from Ref. [43]).*

More differential distributions and their comparison to the bound $\Delta\Delta$ ansatz are shown in the Appendix.

6.1.4 ΔΔ FSI

By looking at formula eq.7 one can observe that it strongly resembles a final state interaction [44]. So one can make a more general statement, namely that we just have a final state interaction (FSI) between the two Δ's. In case of nucleon-nucleon scattering we can deduce from the known scattering length that there is an attraction both in the isospin 0 and 1 channels and that there exists a bound nucleon-nucleon state in the isospin 0 channel (deuteron).

Following the original FSI papers of Migdal and Watson [44] for the NN case we parameterize the ΔΔ FSI in the form

$$F_{FSI}^2(q_{\Delta\Delta}^2) = 1 + \frac{R^{-2}}{\left(-\dfrac{1}{a_s} + \dfrac{1}{2}r_0 p_{\Delta\Delta}^2\right)^2 + p_{\Delta\Delta}^2} \tag{8}$$

here a_s is the scattering length, R characterizes the size of the vertex region and r_0 is the effective range. $p_{\Delta\Delta}$ here denotes to the Δ momentum in the ΔΔ subsystem, i.e. $p_{\Delta\Delta} = \frac{1}{2}q_{\Delta\Delta}$.

The formula depends very weakly on r_0, so we fix it at 2 fm, a reasonable value close to the one used in the NN case. In this way we reduce the 3 parameter fit to a 2 parametric function and fit our data, *Fig. 6—6*.

The scattering length a_s affects the width of the peak in the $M_{\pi\pi}$ spectrum whereas R influences the ratio between the peak and the shoulder. The plotted curve was obtained with the following fit values. $a_s = -16\,\text{fm}/+10\,\text{fm}$ and $R = 1.1\,\text{fm}$. The value $a_s = 10\,\text{fm}$ says that ΔΔ is bound. If $a_s = -16\,\text{fm}$ then ΔΔ is in the continuum. With our experiment we can not distinguish the sign of the scattering length. To do so we would need a polarized Δ beam and a polarized Δ target, which is impossible. A more careful consideration shows that we are actually sensitive only to the absolute value of a scattering length: $|a_s|$.
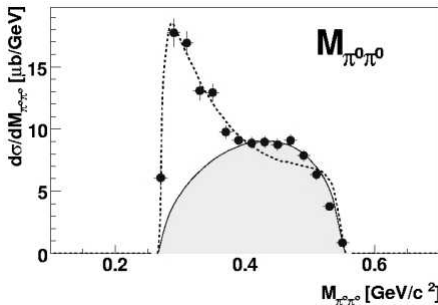
Fig. 6—6 Experimental invariant mass distribution of the $\pi^0\pi^0$ channel in comparison with ΔΔ FSI calculations (dashed line) and phase space (shaded area).

Since in the case of absorption the scattering length is a complex quantity, where the real part corresponds to attraction/repulsion in the scattering channel and the imaginary part to the absorption, it might well be that in our case the main contribution to $|a_s|$ comes from absorption into $NN\pi\pi$ and NN systems.

This can lead to misinterpretation in the case of non-observing the nucleon system: Let's assume that we have a scalar-isoscalar $\pi\pi$ system with relatively small invariant mass and rather large common momentum traveling through the nuclear medium. An experimentalist who would measure only $\pi\pi$ at the end of the medium will observe a huge $\pi\pi$ attraction — which is absent in vacuum. Hence one could come to the conclusion of strong medium modifications of the σ meson. By observing the full system it might become obvious that such an induced attraction actually results from $\Delta\Delta$ rescattering and attraction in the $\Delta\Delta$ system.

6.1.5 Energy dependence of the total cross section.

In addition to the differential distributions one can study the energy dependence of the total cross-section. Monte-Carlo technique provides us with such a possibility by usage of the "Fermi phase space" option. Whereas phase space gives a cross section steadily increasing with s, we expect from the $\Delta\Delta$ ansatz to obtain some resonance-like structure with the maximum around the $\Delta\Delta$ mass (plus the mass of "spectator" nucleons in the final nucleus) and a width in the order of the Δ width. Indeed, this is borne out by the Δ calculations as demonstrated in *Fig. 6—7.*
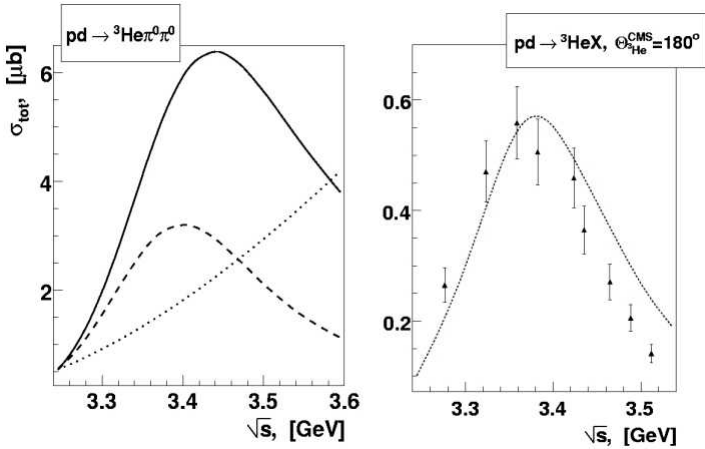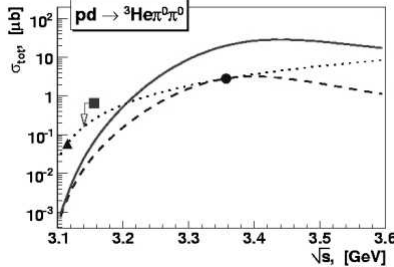

Fig. 6—7 Left: Total cross-section as a function of the total CMS energy $\sqrt{s}$ (Mandelstam "s") for the $pd \rightarrow {}^3He\pi^0\pi^0$ process, solid - $\Delta\Delta$ model; dashed - bound $\Delta\Delta/\Delta\Delta$ FSI model, dotted - phase space. All curves are normalized to have the same cross-section at $\sqrt{s} = 3.156$ GeV. Right: data from Ref. [6] at $\Theta_{^3He}^{CMS} = 180°$ for the low-mass $\pi\pi$ enhancement relative to phase space ("ABC peak") and calculation for the bound $\Delta\Delta$ ansatz.

The energy dependence of the cross-section for the "ABC peak" (low mass $\pi\pi$ enhancement relative to phase space) was measured inclusively at $\Theta^{CMS}_{^3\text{He}} = 180°$ at Saclay [6]. The data indeed show the expected resonance-like behavior, *Fig. 6—7*.

One can see from *Fig. 6—7* that the total cross-sections obtained from the $\Delta\Delta$ and the bound $\Delta\Delta$ ansatz behave similar, but the cross-section in the bound $\Delta\Delta$ case starts to decrease somewhat earlier. Though the bound $\Delta\Delta$ calculations describe the Saclay data for the "ABC peak" cross section at $\Theta^{CMS}_{^3\text{He}} = 180°$ quite well, they obviously overestimate the cross section at high $\sqrt{s}$. This is not unexpected, since at high energies the total cross-section should also be suppressed by the formfactor of the ^{3}He, which is not yet included in our ansatz.

Close to threshold the cross-section of the $\Delta\Delta$ excitation gets very small, see *Fig. 6—8*.

Fig. 6—8 Total cross section as a function of the total CMS energy $\sqrt{s}$ (Mandelstam "s") for the $pd \to {}^3\text{He}\pi^0\pi^0$ process. The solid dot is the data from our measurement, the triangle denotes the PROMICE/WASA [9] data point, the square is the upper limit deduced from the COSY-MOMO [10] data. Solid - $\Delta\Delta$ model; dashed - bound $\Delta\Delta$ model, dotted - phase space. See text for details.

In the figure above one can see 3 data points, from left to right — PROMICE/WASA, COSY-MOMO and CELSIUS-WASA (our measurement). The first and third points were direct measurements of the $pd \to {}^3\text{He}\pi^0\pi^0$ process, but not the MOMO result. From Ref. [10] one can deduce the total cross-section for the $pd \to {}^3\text{He}\pi^+\pi^-$ process at $T_p = 546\,\text{MeV}$ to be $\sigma(pd \to {}^3\text{He}\pi^+\pi^-) = 1.3\,\mu\text{b}$. Assuming that the isovector ($I = 1$) contribution is 0^a, we would deduce the

$\sigma(pd \to {}^3\text{He}\pi^0\pi^0) = \sigma(pd \to {}^3\text{He}\pi^+\pi^-)/2 = 0.65\,\mu\text{b}$. This is an upper limit for the $pd \to {}^3\text{He}\pi^0\pi^0$ cross section at that energy ($\sqrt{s} = 3.156\,\text{GeV}$). Since the $\pi^0\pi^0$ system is 10 MeV lighter than the $\pi^+\pi^-$ system, the relevant energy is, however, $\sqrt{s} = 3.149\,\text{GeV}$ as indicated in *Fig. 6—8* by the arrow.

---

[a] $\sigma_{tot}(\pi^+\pi^-) = \sigma_{I=0}(\pi^+\pi^-) + \sigma_{I=1}(\pi^+\pi^-)$, if $\sigma_{I=1} = 0$ than $\sigma_{tot}(\pi^+\pi^-) = \sigma_{I=0}(\pi^+\pi^-)$ and since $\sigma_{I=0}(\pi^+\pi^-) = 2 \cdot \sigma_{I=0}(\pi^0\pi^0)$ and $\sigma_{tot}(\pi^0\pi^0) = \sigma_{I=0}(\pi^0\pi^0)$ then one can derive $\sigma_{tot}(\pi^0\pi^0) = (\sigma_{tot}(\pi^+\pi^-) - \sigma_{I=1}(\pi^+\pi^-))/2$

The phase space curve at *Fig. 6—8* is normalized to the PROMICE/WASA [9] point, since we know that close to threshold everything should be according to phase space, because only s-waves are involved. The $\Delta\Delta$-FSI calculations is normalized to our data point, because at our energy this process is dominant and the $\Delta\Delta$ model is normalized to give the same results at threshold as the bound $\Delta\Delta$ calculation (both $\Delta\Delta$ models should be tiny at threshold).

From our $\Delta\Delta$-FSI ansatz for the ABC effect (dashed curve) we see that in both the PROMICE/WASA and the MOMO cases the contribution from the ABC effect to the total cross-section is negligibly small (per mille to percent level). So two-pion production close to threshold is dominated by other processes, and that is why the ABC peak should not be visible in their case — exactly as it was observed, see [9],[10].

6.1.6 Comparison with the basic $\pi\pi$ production process

One can find a lot of similarities between the basic $pp \to pp\pi\pi$ production and $pd \to {}^3\text{He}\pi\pi$. Indeed in the $pp \to pp\pi\pi$ case close to threshold the data exhibit a phase space like behavior in the $\pi\pi$ invariant mass with some shift towards high invariant masses compared to phase space — the higher the excitation energy the stronger the shift [57],[58]. Such behavior occurs up to $T_{beam} = 1.0\,\text{GeV}$ ($Q = 0.177\,\text{GeV}$, Q is the excitation energy) and can be well described by the $N^*(1440)$ Roper resonance excitation and its subsequent decay into $N\sigma$ or $\Delta\pi$, [45][46][47], or alternatively by chiral dynamics [48]. At energies higher than 1 GeV ($Q > 0.177\,\text{GeV}$) the behavior of the data changes drastically, demonstrating now a dominant $\Delta\Delta$ excitation, but again without the expected [39][47]double hump structure in the $M_{\pi\pi}$ spectrum, however, again with a low-mass enhancement in $M_{\pi^0\pi^0}$ [58].

A similar picture we can derive from existing $pd \to {}^3\text{He}\pi\pi$ data: close to threshold — $T_{beam} = 0.477$ GeV ($Q = 0.032$ GeV), Ref [9], PROMICE/WASA — the data show reasonable agreement with phase space. If we go further— $T_{beam} = 0.546$ GeV ($Q = 0.070$ GeV), Ref [10], MOMO — the data show a substantial shift towards high invariant masses as compared to phase space. And if we go even higher — $T_{beam} > 0.624$ GeV ($Q > 0.120$ GeV) [3], Berkeley — then the ABC effect ($\Delta\Delta$) starts to appear, becoming clearly visible at $T_{beam} \geq 0.745$ GeV ($Q \geq 0.190$ GeV) [6], Saclay. I.e., we notice a close correspondence between $pp \to pp\pi\pi$ and $pd \to {}^3\text{He}\pi\pi$: in both cases the $\Delta\Delta$ excitation (without the expected double hump structure) appears at roughly $Q = 0.170$ GeV i.e. $T_{beam} = 1.0$ GeV for the $pp \to pp\pi\pi$ and $T_{beam} = 0.720$ GeV for the $pd \to {}^3\text{He}\pi\pi$ reaction, respectively. Extrapolating to the $dd \to \alpha\pi\pi$ case one should expect the appearance of the $\Delta\Delta$ excitation (ABC effect) at $T_{beam} = 0.92$ GeV and becoming clearly pronounced at $T_{beam} = 0.97$ GeV with the maximum strength around $T_{beam} = 1.15$ GeV — as actually has been observed in the corresponding inclusive measurements at Saclay [49].

6.1.7 Medium modifications

Though the $\Delta\Delta$ concept provides a very good description of our measurements, we give here a short discussion of alternative concepts to explain the ABC effect. Since we have seen that the produced $\pi\pi$ pairs are scalar-isoscalar, it appears possible to associate the ABC effect with medium modifications of the σ meson. In fact the σ meson is expected to be modified in medium strongly [50][51] due to partial restoration of the chiral symmetry.

In this concept the mass of the σ meson is modified according to $m_\sigma(\rho) = m_\sigma\left(1 - \alpha\dfrac{\rho}{\rho_0}\right)$,

where m_σ is the free mass of the σ meson; ρ is the density of the nuclear medium and

ρ_0 is the saturation density $\rho_0 = 0.17$ nucleons/fm^3. $\alpha = \dfrac{\sigma_{\pi N}}{m_\pi^2 f_\pi^2}$ with $\sigma_{\pi N}$ being the

pion-nucleon σ-tem ($\sigma_{\pi N} \approx 50$ MeV) and f_π the pion decay constant. Results from Ref. [51] for such considerations are shown in *Fig. 6—9*
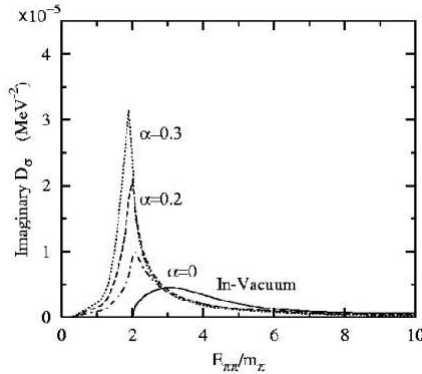
Fig. 6—9 Results for the imaginary part of the sigma-meson propagator in the medium. Solid line - vacuum case. Rest – calculation for normal nuclear density with different α parameters[50].

As one can see, medium modifications also can lead to an enhancement at threshold (since one can directly relate the $\text{Im}(D_\sigma)$ to the $M_{\pi\pi}$). However, they are not directly associated with Δ excitations as we observe in our measurements. Alternatively Roca et al. [52] obtain qualitatively similar results by Δ-hole excitations of the medium. So the question is whether such medium modifications of the σ-meson, which lead to an enhancement just at threshold, describe a physics phenomenon different from the $\Delta\Delta$ model, or whether it is just a different description of the same phenomenon.

6.1.8 Contribution of the three-pion production in the inclusive spectra.

With a quantitative description of two-pion production at hand we can try to understand also quantitatively the inclusive ^{3}He momentum spectrum in *Fig. 4—6* and extract the contribution from 3π production at our energy $T_p = 0.895\,\text{GeV}$. In *Chapter 6.1.3* we have presented the description of the isoscalar part of two-pion cross-section. To simulate its isovector part, which we need for $\pi^+\pi^-$ production, we assume ρ production in this channel, which carries the quantum numbers of the ρ-meson, i.e. we

assume $\sigma(I=1) \propto \dfrac{1}{(M_{\pi^+\pi^-} - M_\rho)^2 + \dfrac{\Gamma_\rho^2}{4}}$, where $M_\rho = 0.77$ GeV; $\Gamma_\rho = 0.15$ GeV[a] (*see*

also Fig. 5—7). Then we can fit the relative contributions from the isoscalar and the isovector parts for the best reproduction of the $\pi^+\pi^-$ spectrum, *Fig. 6—10*.

The best solution of the fit gives $\sigma(\pi^+\pi^-)_{I=0} = 4.6\,\mu\text{b}$ and $\sigma(\pi^+\pi^-)_{I=1} = 1.2\,\mu\text{b}$; with $\sigma(\pi^0\pi^0)_{I=0} = 2.8\,\mu\text{b}$. As described before, according to isospin symmetry $\sigma(\pi^+\pi^-)_{I=0} = 2\cdot\sigma(\pi^0\pi^0)_{I=0}$. Since the $\pi^0\pi^0$ cross-section is much more reliable in its absolute normalization, we assume that $\sigma(\pi^+\pi^-)_{I=0} = 2\cdot 2.8 = 5.6\,\mu\text{b}$. From this it follows that $\sigma(\pi^+\pi^-)_{I=1} = 1.5\,\mu\text{b}$, and $\sigma(\pi^+\pi^-)_{tot} = 7.1\,\mu\text{b}$.
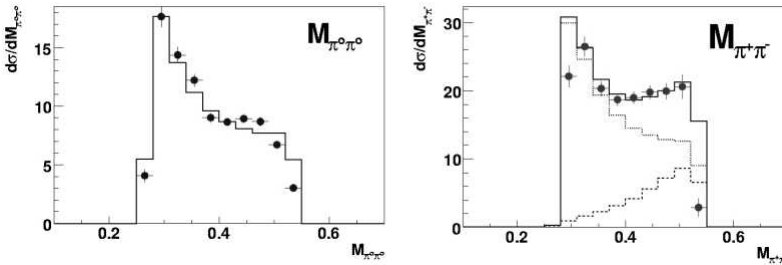
Fig. 6—10 Left: $\pi^0\pi^0$ invariant mass distribution; solid line is the calculation of the bound $\Delta\Delta$ model. Right: $\pi^+\pi^-$ invariant mass distribution; dashed line - ρ meson contribution; dotted line - bound $\Delta\Delta$ model calculation; solid line - sum of both contributions. The relative height of the curves is chosen for the best fit of the spectra.

Having fixed the isoscalar and isovector parts of $\pi\pi$ production we simulate the inclusive ^{3}He spectrum. By a fit to the data, see *Fig. 6—11,* a 3π cross-section of $\sigma(3\pi) = 0.5\,\mu\text{b}$ is obtained.

---

[a] A more general approach with p-wave, which leads to a linear rise in the $M_{\pi^+\pi^-}$ spectrum, gives a very similar description.
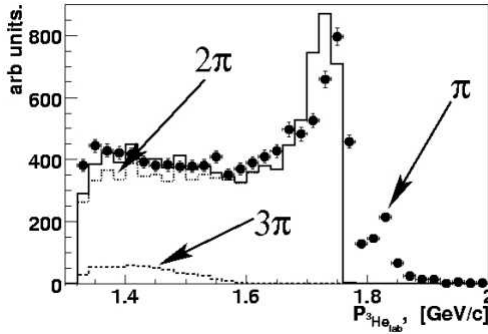
Fig. 6—11 ^{3}He momentum spectrum for the angular bin $7° < \Theta^{lab}_{^3He} < 8°$ *(as it was measured/simulated, not corrected for detector efficiency). The data points represent the inclusively measured spectrum. Most right peak is single pion production. The dotted line gives the description for the two-pion production. The dashed histogram shows the phase space description for the* 3π *production. The solid line represents the sum.*

One can see that the sum line at *Fig. 6—11* still deviates somewhat from the data. This disagreement comes from the fact that at *Fig. 6—10* the model calculation gives a slightly smaller width of the ABC peak. Taking into account the uncertainties in the different model assumptions one can estimate the 3π cross-section to be in the range $0.3 \div 1.3\,\mu b$.

6.1.9 $\Delta\Delta$ FSI-model for other nuclear systems.

Since the $\Delta\Delta$-FSI model describes our data amazingly well, we can try to extend it to other nuclear systems, different reactions and energies.

The simplest case is the $dd \to \alpha X$ reaction below the η threshold and particularly $dd \to \alpha\pi\pi$. Here the isospin $I=0$ is the only possible configuration for the $\pi\pi$ system, meaning that contributions from the ρ meson should be exactly zero[a]. The available data are inclusive measurements by Saclay[8] at 0°. The measurement at the maximum of the ABC effect is that at $T_d = 1.084$ GeV. In *Fig. 6—12* the data from Saclay [8] are compared to our calculations in the $\Delta\Delta$-FSI model. One can see that the model describes the data very well, underestimating them only at high invariant masses, exactly at the place where the 3π production should contribute. It means that for the $dd \to \alpha\pi\pi$ reaction the model also works. Here the difference to the calculations for $pd \to ^3He\pi\pi$ (*Chapter6.1.4*) is tiny — only the mass of projectile is changed from proton to deuteron and mass of ^{3}He is changed into mass of ^{4}He. The Fermi-motion is assumed to be the same for ^{3}He and ^{4}He, which is in agreement with the fact that the radii of both nuclei are very similar.

---

[a] It is still possible to have ρ meson contribution due to isospin symmetry violating terms and due to ρ-ω mixing, but such contributions should exhibit themselves at the per mille level.
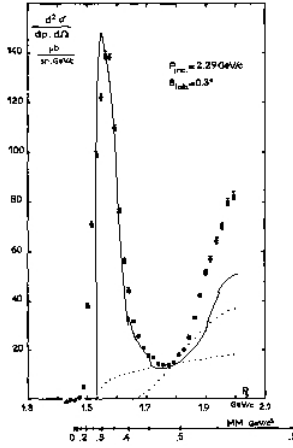
Fig. 6—12 Momentum distribution of α particles at 0° for the dd → αX reaction at T_d=1.084 GeV. The solid line shows the ΔΔ-FSI model calculations, normalized to the peak cross-section. The dotted line represents phase space, normalized to touch the data in the minimum, the dashed line shows the 3π contribution normalized arbitrarily. The nonlinear scale in the bottom of the figure shows the translation of the α momentum into the invariant mass of system X.

We may test our model further and even more crucially by exclusive measurements of the most basic reaction leading to bound nuclear states, which is the reaction $pn \to d\pi^0\pi^0$. First preliminary data for it at $T_p = 0.895$ GeV are available now from the ongoing PhD work [56] in our group. The excitation energy is slightly lower compared to our $pd \to {}^3He\pi^0\pi^0$ measurement but still in the ABC region.
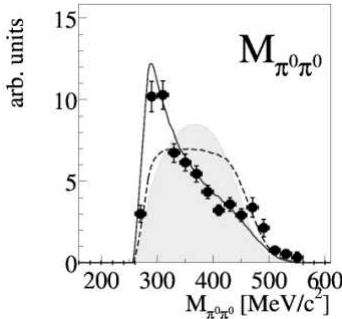
Fig. 6—13 Preliminary data for the invariant mass of 2π from $pn \to d\pi^0\pi^0$ reaction[56] compared to the prediction of the ΔΔ-FSI model (solid), ΔΔ model (dashed) and phase space (shaded).

The model describes the data again very well without adjustment of any parameters demonstrating thus its validity for a large variety of energies and systems.

78

7 Summary

The first exclusive measurements of $pd \rightarrow {}^3\mathrm{He}\pi^0\pi^0$ and $pd \rightarrow {}^3\mathrm{He}\pi^+\pi^-$ reaction channels in the ABC energy range were performed and analyzed. The exclusive data reveals the ABC effect to be

- a low-mass $\pi\pi$ phenomenon not necessarily associated with a high-mass one,
- particularly pronounced in the $\pi^0\pi^0$ channel,
- associated with $\Delta\Delta$ production and
- of pure scalar-isoscalar nature.

Despite the fact that current measurements are consistent with the previous inclusive ones, the additional exclusive information turns out to be crucial for the understanding of double-pionic fusion processes. It has been shown that the conventional $\Delta\Delta$ explanation can no longer survive the data test. The new experimental information points to a very strong $\Delta\Delta$ interaction — parameterized here as quasi-bound state condition or more general as $\Delta\Delta$ FSI — for which no information is available from other sources and which so far has not been considered in theoretical investigations of the NN system and its excitations. The angular distribution, together with isospin decomposition shows that the effect is scalar-isoscalar in nature. There is a small of $I=1$ contribution in the $pd \rightarrow {}^3\mathrm{He}\pi^+\pi^-$ reaction consistent with ρ-meson excitation.

Another possibility of an explanation of the ABC effect are nuclear medium effects[50], observed before also in $\pi A \rightarrow \pi\pi X$,[53][54] and $\gamma A \rightarrow \pi\pi X$,[55]. However this explanation lacks the simultaneous $\Delta\Delta$ excitation.

The model of $\Delta\Delta$ FSI can describe also $pn \rightarrow d\pi^0\pi^0$ quantitatively [56] without changes of parameters or any additional assumptions. The same holds for the descriptions of the inclusive Saclay data [8] on $dd \rightarrow \alpha X$.

Predictions for the energy dependence of the total cross sections also agree quite well with the measurements. Based on this model one can understand the full set of existing two-pion data on bound nuclear systems.

8 Other reactions

Several other reactions have been analyzed during the course of this PhD work, but since they are outside the ABC topic they were not mentioned in the main part of the thesis:

$pp \rightarrow pp\pi^+\pi^-$ at $T_p = 895, 1000, 1100, 1300, 1360$ MeV [57],[58].

$pp \rightarrow pp\gamma\gamma$ at $T_p = 1200$ and 1360 MeV. Here an observed spike at the two-pion threshold is of particular interest [59],[60].

$pp \rightarrow d\pi^+\pi^0$ at $T_p = 1100$ MeV [58].

Results from these reactions were presented at several conferences, and published in conference proceedings [57—60]. Further publications are foreseen.

9 Outlook

Despite the obvious success in the explanation of the existing data about the ABC effect there remains a number of issues to be done for a complete understanding of the strong enhancement observed at low $\pi\pi$ masses. This includes the energy dependence of the ABC cross-section as well as its nuclear dependence, i.e. exclusive measurements not only with proton beam and deuteron target, but also with heavier projectiles and targets. In addition the use of polarized beams will be very helpful in order to disentangle different partial wave contributions. Many of these projects can be performed at COSY with the upgraded WASA detector. However, some better understanding we can get already now, by analyzing $pn \rightarrow d\pi\pi$ and $dd \rightarrow \alpha\pi\pi$, reactions from the collected CELSIUS-WASA data sample. Hopefully in a few years from now we will understand the ABC effect in all its details and learn possibly about the behavior of the σ meson in the nuclear medium. The study of double-pionic fusion appears by an ideal doorway situation for the understanding of a possible chiral restoration in the medium.

10 Acknowledgments

11 Appendix

In this chapter the following notation is used: c.m. — center of mass system; lab. – laboratory system; the upper indexes always correspond to a subsystem, if indexes are absent then it is silently assumed to be the center of mass system; $\Theta_{\pi\pi}$ — angle of $\pi\pi$ system in center of mass system relative to z (beam axis); $\Theta_{\pi}^{\pi\pi}$ — angle of pion in $\pi\pi$ subsystem relative to z (Jackson frame); $\widehat{\Theta}_{\pi}^{\pi\pi}$ — angle of pion in $\pi\pi$ subsystem relative to $\pi\pi$ momentum direction (Helicity frame). M is invariant mass. $\delta_{\pi\pi}$ is the opening angle between pions, $\Delta\phi$ is the planarity angle.

Shaded area is phase space, dashed line is $\Delta\Delta$ model calculation. Dots are experimental efficiency and acceptance corrected data.
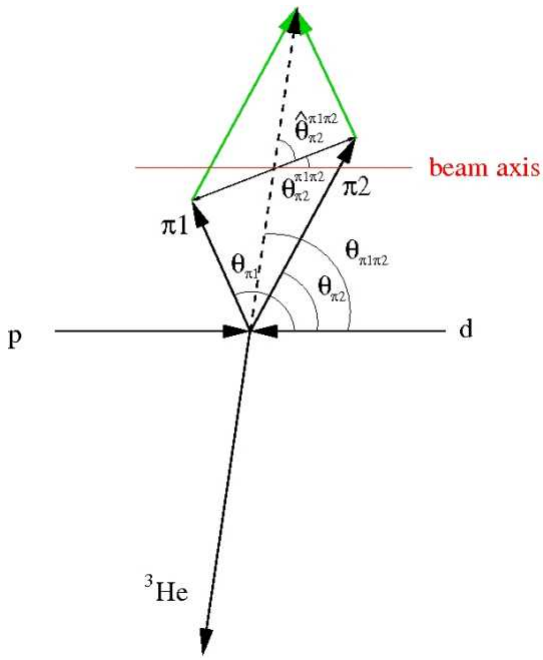
Fig. 11—1 The definition of the different scattering angles in the subsystem of particles, here for two particles in overall center of mass system. For simplification, the figure shows a non-relativistic construction.

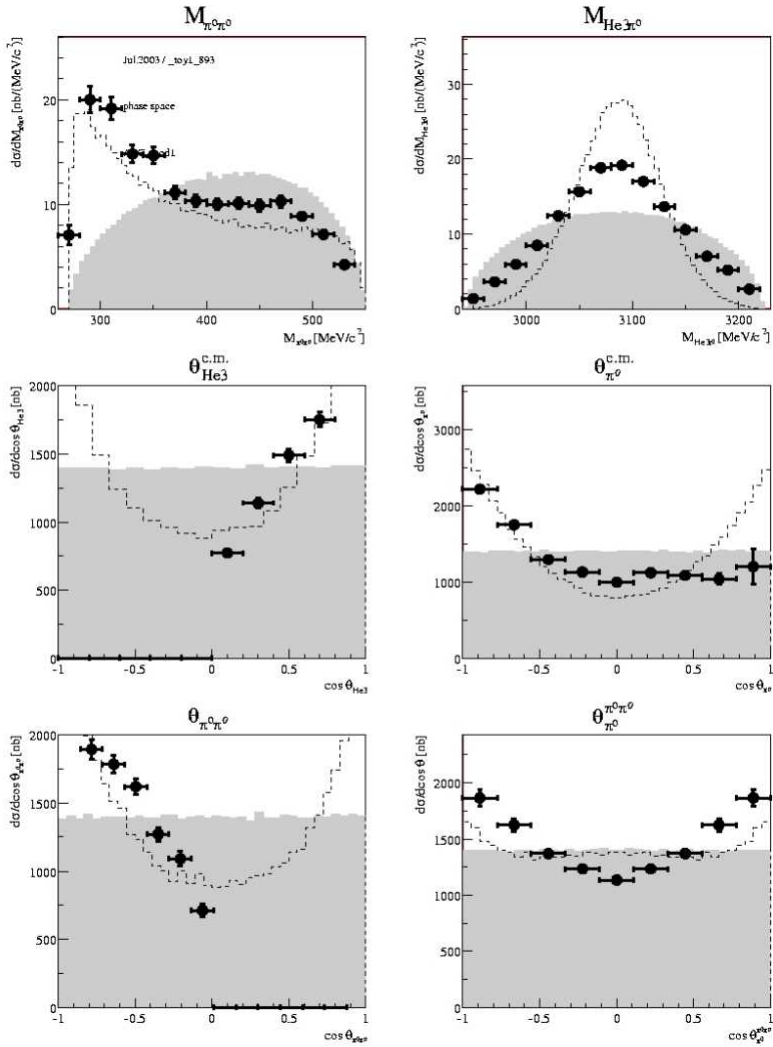# 11.1 $^3He\pi^0\pi^0$ differential cross-sections

Fig. 11—1 Differential distributions. Shaded area is phase space. Dashed line is the bound $\Delta\Delta$ model calculations.
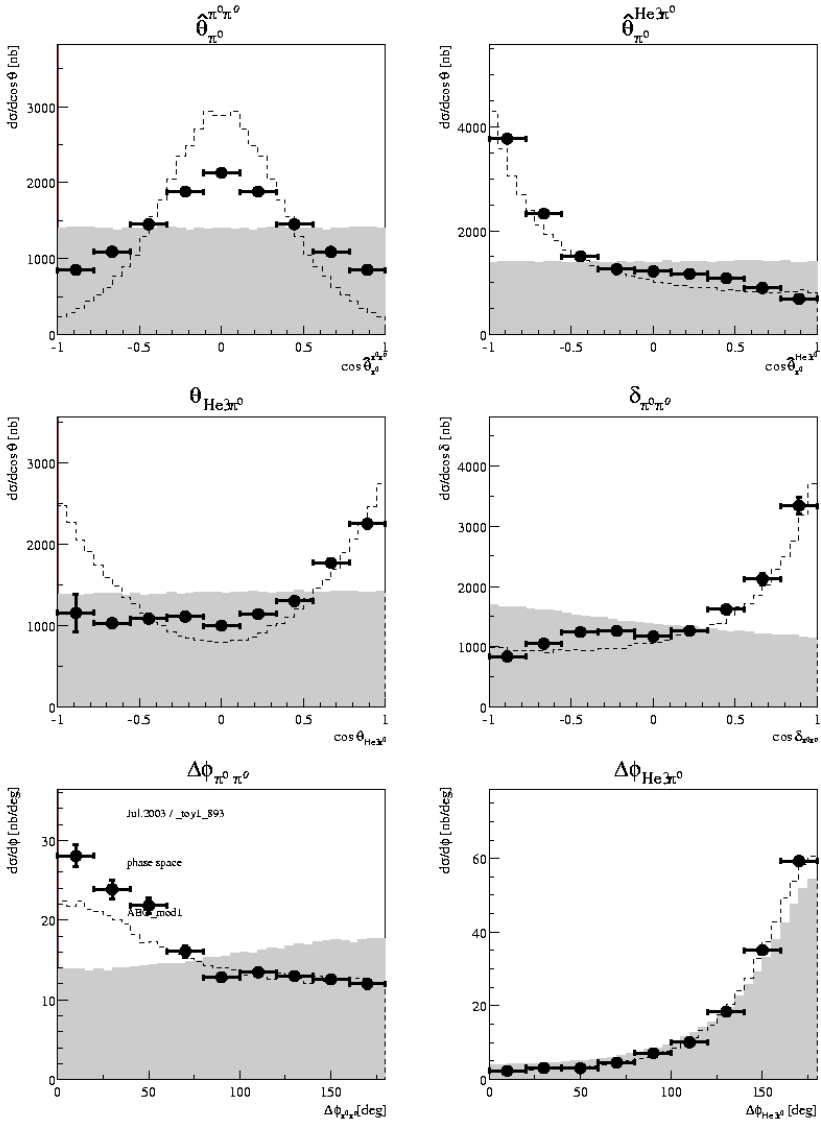
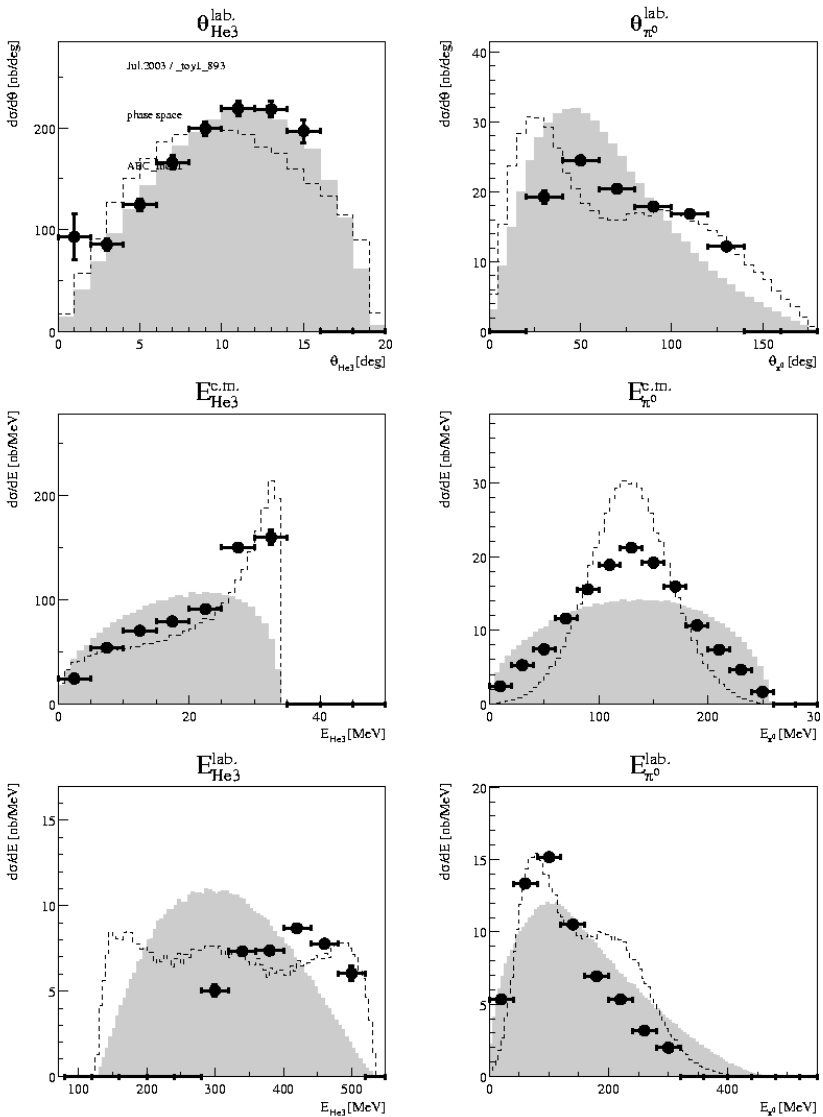*Fig. 11—2 Differential distributions. Notation is described above.*

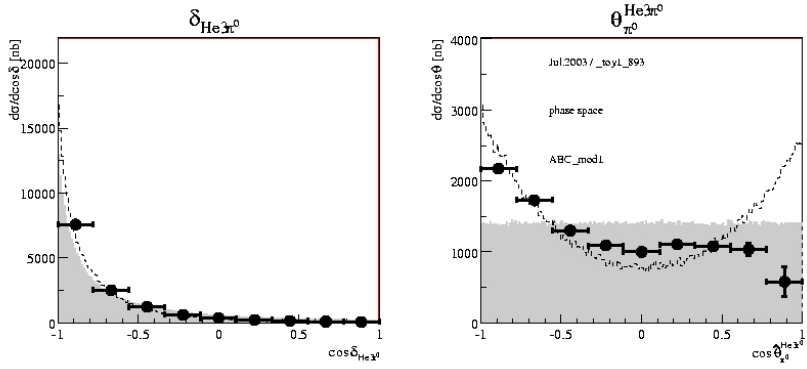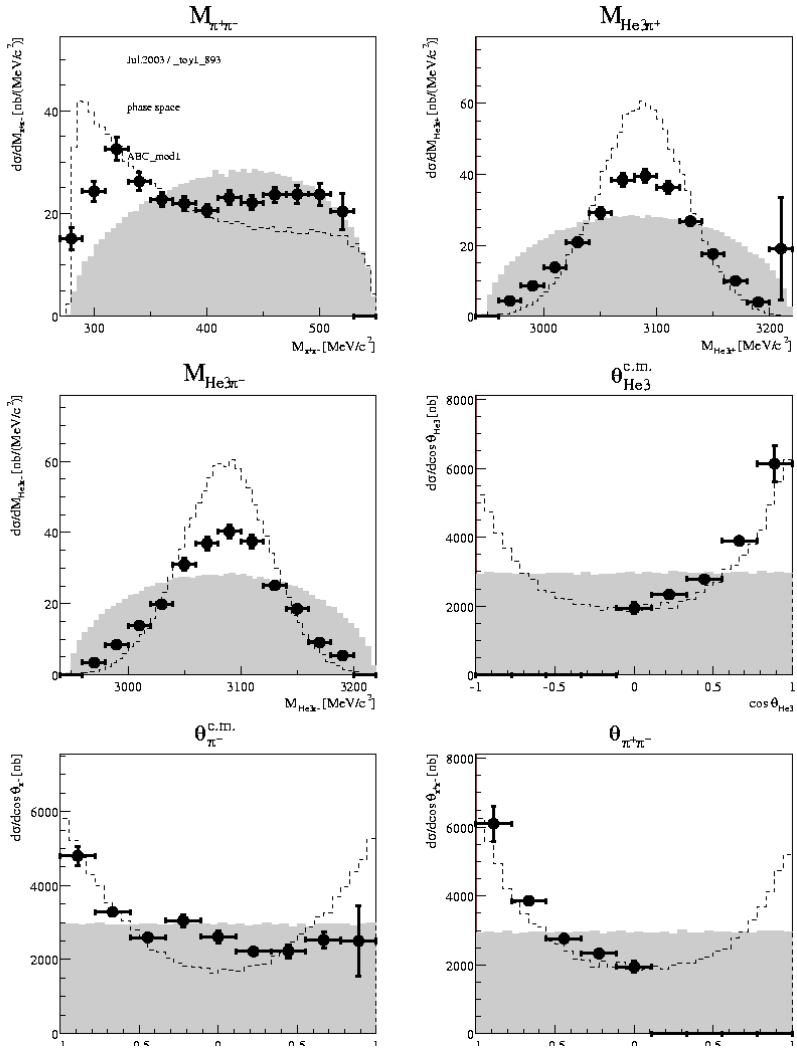*Fig. 11—3 Differential distributions. Notation is described above.*

Fig. 11—4Differential distributions. Notation is described above.

11.2 $^3He\pi^+\pi^-$ differential cross-sections

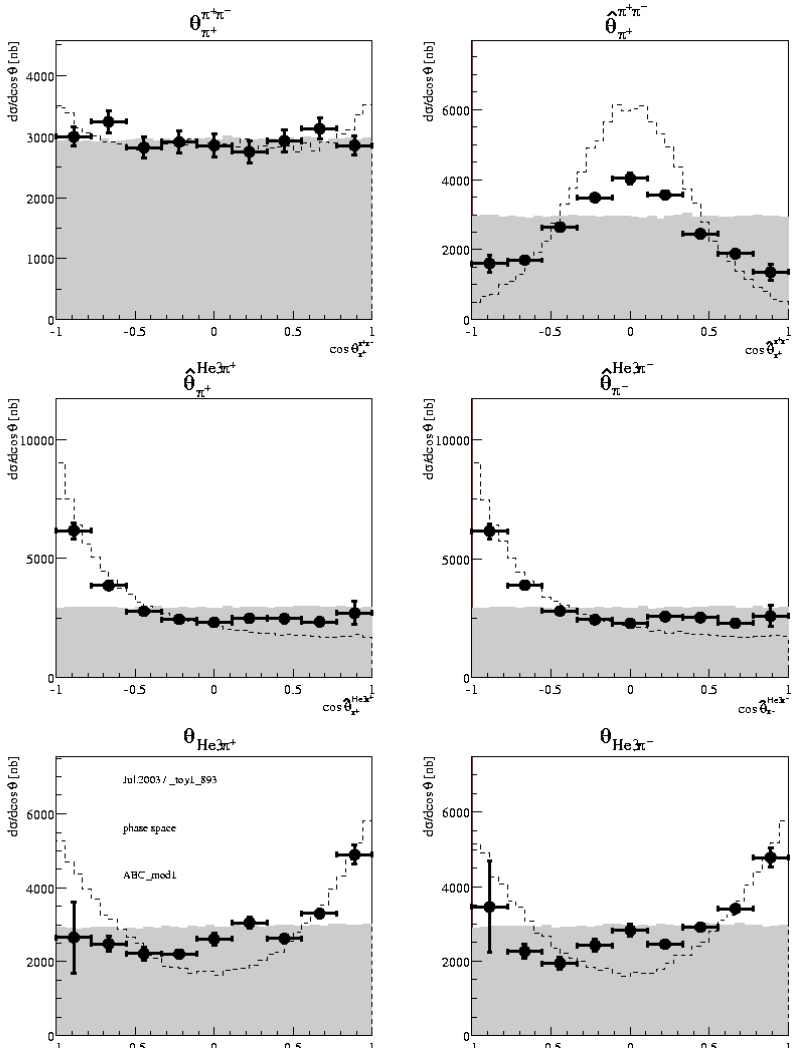*Fig. 11—5 Differential distributions. Notation is described above.*

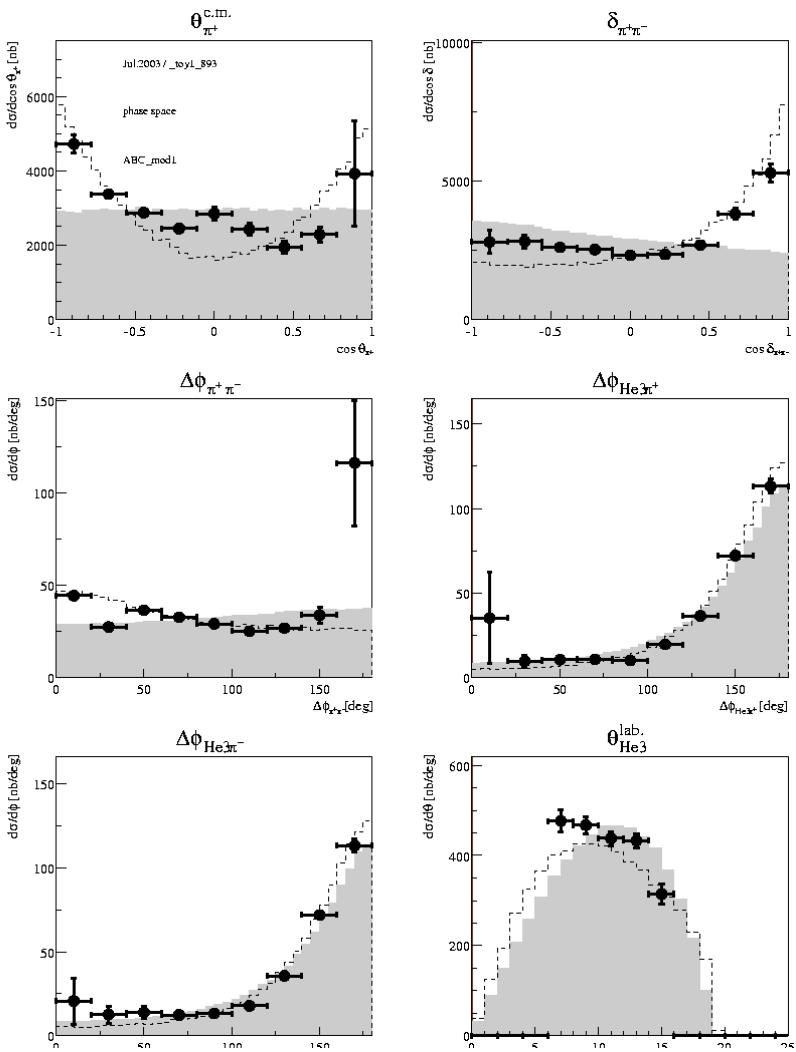Fig. 11—6 Differential distributions. Notation is described above.

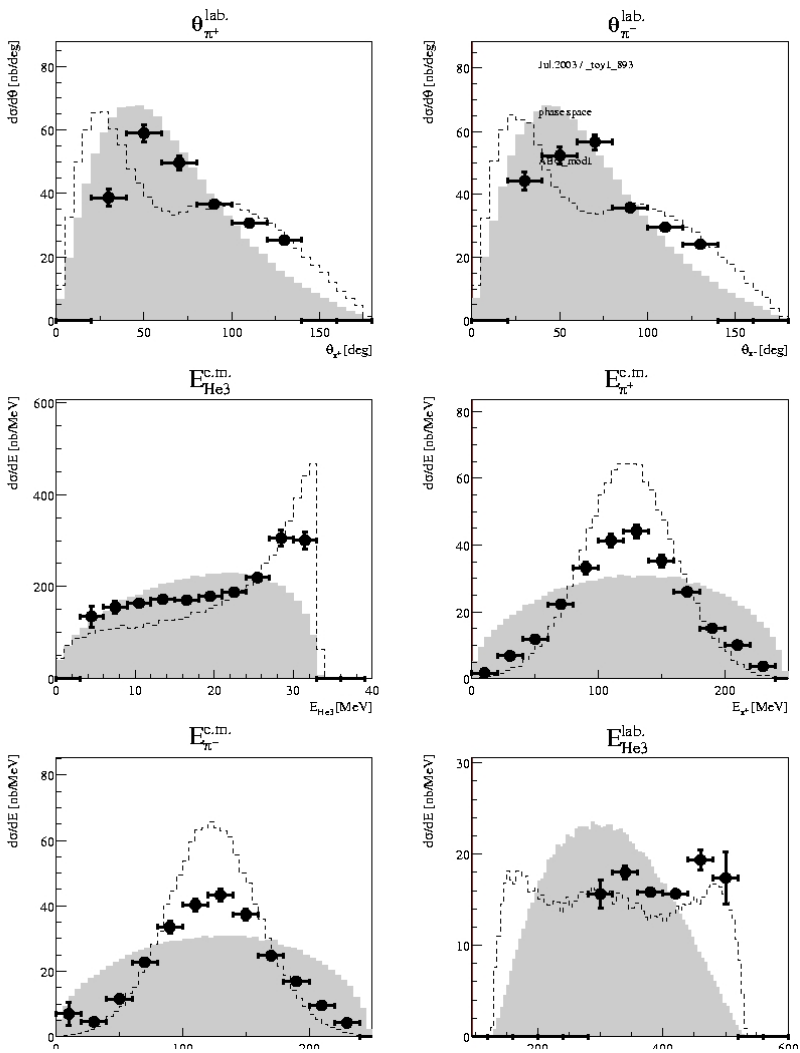*Fig. 11—7 Differential distributions. Notation is described above.*

Fig. 11—8 Differential distributions. Notation is described above.
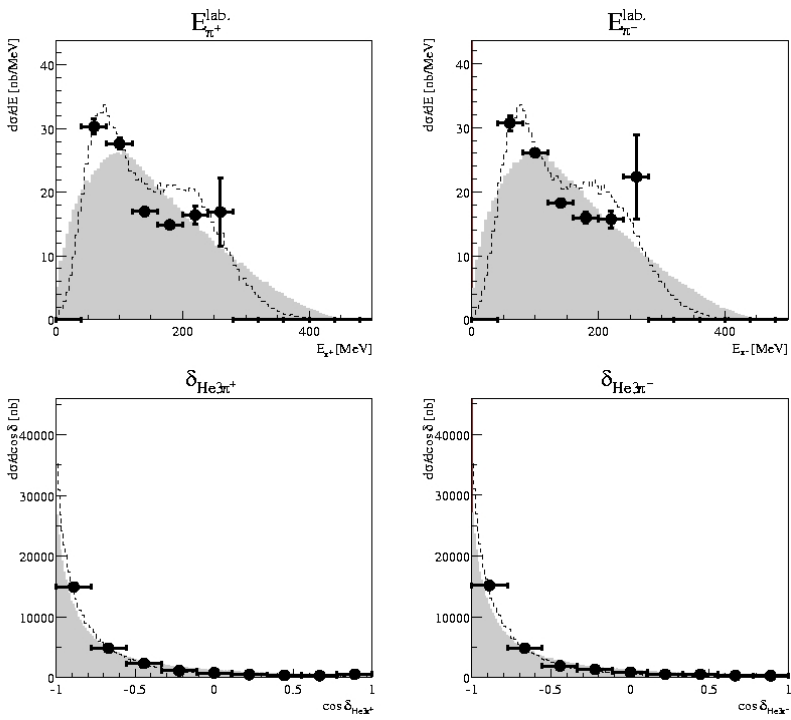
Fig. 11—9 Differential distributions. Notation is described above.

12 Appendix A

Here the derivation of the angular corrections for the Forward and Central detector will be done (begin in *Chapters 3.2.4, 3.2.5*).

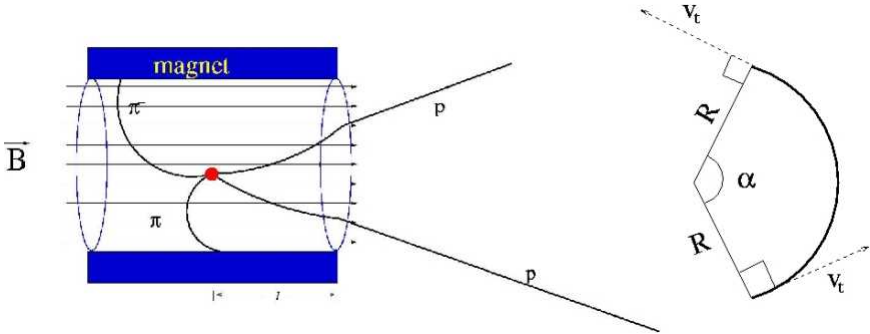The flight paths of charged particles in the solenoidal magnetic field of the WASA detector look as follows.

Fig. 12—1 The flight path of charged particles in magnetic field. Left: longitudinally cut figure. Right: transverse projection for a single track.

Let us first consider the case, when a charged particle moves in forward direction. Here only a part of the track lies in the magnetic field. In simplest approximation we can assume that inside the solenoid we have a homogeneous magnetic field B and outside the solenoid the magnetic field is 0. First we decompose the momentum of the charged particle p into two components: longitudinal (p_l) and transversal (p_t). The longitudinal component says how long particle will stay in the magnetic field $t = l/v_l$. Here l is the length of a field from the interaction point, t is the time and v_l is the longitudinal component of the velocity. The transversal component directly corresponds to changes in the azimuthal angle. According to [36] equation (28.40) $p_t = 0.3 \cdot z \cdot B \cdot R$, there z is the charge of the particle in the units of the electron charge, B is magnetic field in tesla and R is the curvature of the track in transversal plane.

Let us call the length of the arc at *Fig. 12—1, right* as a. Then this length can be calculated as $a = v_t \cdot t = v_t \cdot \dfrac{l}{v_l} = l \cdot \dfrac{v_t}{v_l} = l \cdot tg\Theta$, where Θ is the polar angle. As one can see from the picture the changes in the φ angle is exactly equal to the angle α. Knowing the length of arc a and the curvature R we can calculate this angle:

$$\alpha = \frac{a}{R} = \frac{l \cdot tg\Theta}{1} \cdot \frac{0.3 \cdot z \cdot B}{p_t} = \frac{l \cdot \sin\Theta \cdot 0.3 \cdot z \cdot B}{p \cdot \sin\Theta \cdot \cos\Theta} = \frac{0.3 \cdot z \cdot B \cdot l}{p \cdot \cos\Theta} .$$

For the case of central going particles, the situation is slightly different, since the full track lies in the magnetic field, and the time inside the field is determined not by the variable l, but related to the radius r of the magnet. Geometrically one can build a

triangle, based on *Fig. 12—1* with two sides of length R, the angle α in between and with the third side being of length r. So $\alpha = \pi - 2 \cdot a\cos(r/2R) = \pi - 2 \cdot a\cos\left(\dfrac{r \cdot 0.3 \cdot z \cdot B}{2 \cdot p \cdot \sin\Theta}\right)$.

The variables are exactly the same as before.

In these formulas we know all the variables. In principle it is possible to take l and r from documentation, but it is much easier to take it from data or MC: for example from reaction $pp \rightarrow d\pi^+$ at small energies, where the angular corrections for deuteron are large. We took it from MC $l = 0.0953$ [m] and verify with data below.
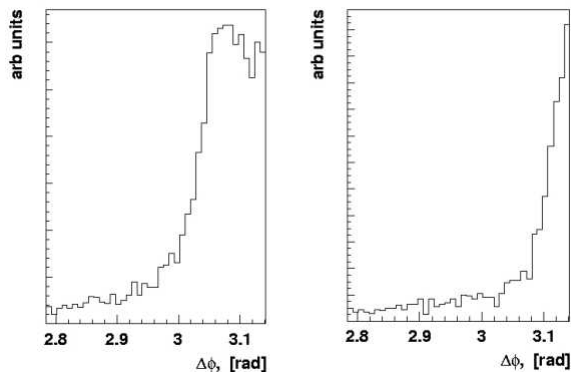

Fig. 12—2 Planarity of particles in FD from $pp \rightarrow d\pi^+$ reaction. Left: before angular corrections. Right: after.

In the ideal case the planarity in a binary reaction should be π. Due to resolution it is not a δ-function but a Gaussian. One clearly sees that the angular correction improves the data a lot.

13 References

1) Leutwyler, Meson06 conference Proceedings, to be published
2) A. Abashian, N.E. Booth, K. Crowe, Phys. Rev. Lett. **5,** 258 (1960)
3) N.E. Booth, A. Abashian, Phys. Rev. **122**, 2314, (1963).
4) J.H.Hall el al., Nucl. Phys. **B12**, 573, (1969)
5) J. Banaigs et al., Nucl. Phys. **B28**, 509 (1971)
6) J. Banaigs et al, Nucl. Phys **B67**, 1 (1973.)
7) F. Plouin et al., Nucl. Phys **A302**, 413, (1978).
8) J. Banaigs et al., Nucl. Phys. **B105**, 52, (1976)
9) Andersson et al., Phys Lett **B485**, 327 (2000)
10) Bellemann et al., Phys Rev. **C60**, 061002(R) (1999)
11) Risser, Shuster, Phys. Lett. **43B**, 68, (1973)
12) F. Plouin, P. Feury, C. Wilkin, Phys. Rev. Lett. **65**, 6, (1990)
13**)** R. Bilger et al., CELSIUS as an eta factory, Nucl. Phys. A **626**, 93c-96c, (1997)
14) H. Calen et al., Nucl. Instrum. Meth. Phys. Res. A **379**, 57-75 (1996)
15) B. Trostell, Nucl. Instrum. Meth. Phys. Res. A **362**,41-52
16) J.M. Dyring, PhD thesis, Uppsala University, 1997.
17**)** M. Dahmen et al., Nucl. Instrum. Meth. Phys. Res. A **348**, 97-104 (1994)
18) M. Waters, Doktorarbeit, Forchungszentrum Juelich, 1994.
19) C. Pauly, CWnotes 031015CP, (2003)
20) C. Pauly et al., Nucl. Instrum. Meth. Phys. Res. A **547**, 294-301, (2005)
21) W. Brodowski, Diplomarbeit, University Tuebingen, (1995)
22) M. Jacewicz, PhD theses Uppsala University, (2004)
23) I. Koch, PhD theses Uppsala University, (2004)
24) C. Bargholtz et al., Nucl. Instr. Meth. Nucl. Phys. **A390**, 160, (1997)
25) P. Marciniewski, PhD thesis, Uppsala University, (2001)
26) H. Calen, Manual, 1992, (2000)
27) Alice internal note ALICE/GEN 95-32
28) J.P. Ernenwein http://e.home.cern.ch/ernen/WWW/NN/index.html
29) A.Schwick, WaC meeting 10.2005
30) L. Demiroes, PhD thesis University Hamburg, (2005)
31) V.M. Abazov et al., Phys. Lett. **B517**, 282, (2001)
32) Root Tutorial, http://root.cern.ch/root/Tutorials.html
33) P.R.Bevington, D.K. Robinson, Data reduction and error analysis for the Physical Science, 2nd edition, Mc-Graw-Hill (1992)
34) A.Kupcs, private communications (1995)
35) J.Banaigs et al., Phys. Lett. **B45**, 394, (1973)
36) PDG booklet 2004, S Eidelman et al., Physics Letters **B592**, 1 (2004)
37) E. Byckling, K. Kajantie, Particle Kinematics, J. Wiley and sons, London-New York-Sydney-Toronto, (1973)
38) A. Gardestig, G. Faldt, C. Wilkin Phys. Rev. **C59**, 2608 (1999) and Phys Lett. **B421**, 41 (1998)
39) L. Alvarez-Ruso, E. Oset, E. Hernandez, Nucl. Phys. **A663**, 519 (1998); Phys Lett **B452**, 207, (1999)
40) H. Müther, privat comm.
41) J. Ping, H. Pang, F. Wang, T.Goldman, Phys. Rev. **C64,** 044003 (2002)

42) A.Fridman, Fortschritte der Physik **23,** 243, (1975)

43) M.Bashkanov et. al., Phys. Lett. **B637**, 223-228, (2006)

44) M. Watson, Phys. Rev **88**, 1163, (1952), A. B. Migdal, JETP 1, 2, (1955)

45) W. Brodowski et al., Phys. Rev. Lett. **88**, 192301 (2002)

46) J. Paetzold et al., Phys Rev. **C67**, 052202(R) (2003)

47) L.Alvarez-Ruso, Phys. Lett. **B452** 207, (1999); L.Alvarez-Ruso, Ph.D Thesis, University of Valencia, (1999)

48) M. Kaskulov, H. Clement Phys. Rev. **C70,** 057001 (2004)

49) J. Banaigs et al., Nucl Phys **B105**, 52 (1976)

50) T. Hatsuda, T. Kunihiro, H. Shimizu, Phys. Rev. Lett, **82,** 2840, (1999)

51) Z. Aouissat et al., Phys. Rev. **C61**, 012202(R)**,** (1999)

52) L. Roca, E. Oset, M.J. Vicente-Vacas, Phys. Rev. Lett. **B541**, 77, (2002)

53) F. Bonutti et al., Nucl Phys **A677**, 213, (2000)

54) A. Starostin, et al. Phys. Rev. Lett., 85, 5539, (2000)

55) J.G. Messchendorp, et al., Phys. Rev. Lett. 89, 222302, (2002)

56) O. Khakimova, privat comunications.

57) M. Bashkanov et al., AIP Conf. Proc. 717:241-44, (2004)

58) T. Skorodko et al., Int. J. Mod. Phys. **A20,** 671, (2005)

59) M.Bashkanov et al., hep-ex/0406081

60) M.Bashkanov et al., Int. J. Mod. Phys. **A20**, 554, (2005)